Novel Mold Modifications for Injection Molding of Specialty Products

By

Demitri Shotwell

A dissertation in partial fulfillment of

the requirements for the degree of

Doctor of Philosophy

Mechanical Engineering

at the

UNIVERSITY OF WISCONSIN-MADISON

2022

Date of PhD final oral examination: 08/31/2022

The dissertation committee:

Lih-Sheng Turng, Professor, Mechanical Engineering
Tim Osswald, Professor, Mechanical Engineering
Roderic Lakes, Professor, Engineering Physics
Corinne Henak, Assistant Professor, Mechanical Engineering
Pavana Prabhakar, Assistant Professor, Civil and Environmental Engineering

Abstract

Two methods of mold modification for injection molding specialty plastic parts were explored in three projects:

First, The effect of an in-mold static mixer on orientation of fiber-reinforced polypropylene (PP) was explored within the injection molding process. Several mold geometries and helical mixer designs were assessed via simulation to identify the mixing ability and the potential effect on fiber orientation. It was found that the static mixers within the runner segment could successfully mix the polymer and randomize the fibers but that the fiber alignment reduction was quickly recovered. Injection molding experiments were carried out to verify these simulations using one geometry case. Fiber orientation at different mold locations were measured using micro-CT (μCT) scans and the degree of fiber orientation was quantified by "goodness of fit" to a normal Gaussian function approach. The experimental fiber orientation results showed good agreement with the simulations. These experiments indicated that the use of a static mixer within the runner system of a mold could be used for mixing the polymer melt after the plasticizing unit of the injection molding machine. However, its effect on changing the overall alignment of the fibers within injection molded parts could be offset by the melt flow downstream of the static mixer, suggesting the importance of mixer location with respect to the part cavity.

In a related project, the effect of an in-mold static mixer on optical properties of polystyrene (PS) parts was explored within the injection molding process. Several helical mixer designs were assessed via simulation and molding trials to identify the mixing ability and the potential effect on optical properties including retardation and birefringence. It was found that the static mixers within the runner segment could successfully mix the polymer and disrupt property distributions such as temperature but that there was only slight improvement in retardation with some of the mixer cases. The experiments and simulations showed relatively good correlation in results although there were slight differences in the trends that could be due to the experimental retardation measurement resolution or unaccounted-for variables between the experiments and simulations. The retardation was experimentally measured using a custom-made polariscope using photography and image processing. These experiments indicated that the use of a static mixer within the runner system of a mold could be used for homogenizing the polymer melt after the plasticizing unit of the injection molding machine. However, its effect on improving the optical performance of injection molded parts could be offset by the melt flow downstream of

the static mixer and potential increase of residual stresses due to flow restriction, suggesting the importance of mixer location and geometry.

Last, the use of a sacrificial reservoir as part of an injection mold with optical polycarbonate (PC) materials was explored with simulations. Three different methods of reservoir designs were considered. The first method was using engineering intuition to determine the geometry, the second method used a combination of mass and momentum balance equations to determine the geometry, the third method used the mass balance equation to determine the geometry. Using these three methods eight reservoirs were designed and simulated and compared to two no-reservoir cases. 27 runs varying three levels of injection flow rate, V/P switch, and packing pressure were simulated for each of the 10 geometry cases. Considering the quality parameters of flow and thermally induced retardation and the average and standard deviation of volumetric shrinkage the benefit of using a reservoir for manufacturing lens parts was considered. For each of the quality parameters the minimum, best, case occurred with one of the reservoirs. Thus, this study offers a proof of concept that reservoirs could offer a method to improve both the retardation and warpage defects in injection molded optical parts.

Acknowledgements

First, I would like to thank my research advisor Lih-Sheng (Tom) Turng for his support and guidance throughout my academic endeavors. I particularly appreciate the support from my graduate school committee members: Tim Osswald, Roderic Lakes, Corinne Henak, Pavana Prabhakar, and Sangkee Min. I would like to acknowledge the support and friendship I have received from colleagues: Galip Yilmaz for training and mentorship, Huaguang (Allen) Yang and Jinsu Gim for discussion, collaboration, and assistance in running experiments, and Stefanie Glas, Edward Chen, Zhutong Li, Allen Jonathan Román, Chase Yankowski, and Chung-Yin Lin for discussion and collaboration. I also would like to acknowledge the support of my family. I am grateful for the generous contributions of CoreTech System for providing Moldex3D and technical support and training for my research, Stamixco for providing static mixers for experiments, and Foxconn for their collaboration and support of my work. This work was partially supported by the Wisconsin Distinguished Graduate Fellowship (WDGF) the Wisconsin Institute for Discovery at the University of Wisconsin−Madison and the Consolidated Papers Foundation Chair Professorship, and the Kuo K. and Cindy F. Wang Professorship.

Table of Contents

Table of Figures

Chapter 1: Effect of Static Mixer on Fiber Orientation of Injection Molded Fiber-Reinforced Composites

Chapter 2: Effect of Static Mixer on Optical Properties of Plastic Injection Molded Parts

Chapter 3: Effect of Sacrificial Reservoir Runner Geometry on Optical Properties of Plastic Injection Molded Parts

Table of Tables

Chapter 3: Effect of Sacrificial Reservoir Runner Geometry on Optical Properties of Plastic Injection Molded Parts

Introduction

Two methods of mold modification for injection molding specialty plastic parts will be explored in three projects:

The goal of the first research project is to analyze the influence of a helical static mixer, which could be a disposable plastic mixer or a reusable steel mixer, on the fiber orientation of fiber-filled thermoplastics when integrated directly into the runner system of an injection mold. This approach ideally allows for disruption of the fiber orientation directly before the melt fills the part gate and does not require any changes to the injection molding machine or significant changes to the mold design. The helical static mixer will be assessed both numerically using injection molding simulation software, Moldex3D, and experimentally with injection molding trials.

In the second research project the influence of static mixers on the melt homogeneity and optical part quality when integrated directly into the runner system is considered. This approach allows for homogenization of the melt properties directly before the melt fills the part gate and does not require any changes to the injection molding machine or significant changes to the mold design. In this study, the effects of static mixers on the quality of plastic parts will be evaluated through both injection molding simulations and experiments.

The goal of the final project is to develop a method for designing an effective mold reservoir which can provide, for the part cavity, flow control, F/P switch over point damping, and complete material packing. This method will be based on engineering intuition and the use of the fundamental balance laws and the power law constitutive equation and will be verified using commercial injection molding simulation software Moldex3D.

Chapter 1: Effect of Static Mixer on Fiber Orientation of Injection Molded Fiber-Reinforced Composites

1. Introduction

Fiber fillers are common additives to many injection molding materials since they can add benefits such as high durability, increased strength and stiffness, and resistance to corrosion, wear, impact, and fire [1]. However, it is a challenge to accurately quantify and control the mechanical properties of a fiber-reinforced injection molded part owing to the complexity of characterizing the fiber orientation and distribution [1, 2, 3, 4]. This attribute is due to the complex part geometry plus effects of runner and gate, intricate injection molding process physics, and the complicated rheological behavior of thermoplastics compounded by the presence and influence of fibers [5]. During injection molding, a complex, multi-layer flow profile forms and develops into a final part, which will typically have several layers of different fiber orientation properties [4, 5]. The symmetric layers shown in Figure 1 consist of a skin or shell layer closest to the mold that is strongly influenced by fountain-flow behavior, a transition skin or shell layer, and a core layer that typically exhibits fiber orientation perpendicular to the flow. On the other side of the core layer is again the transition skin or shell layer, which is adjacent to the skin or shell layer touching the other half of the mold [4, 5].

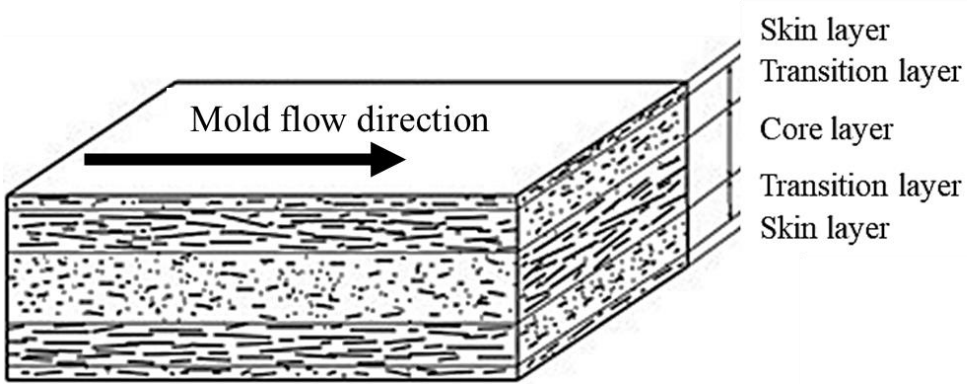

Figure 1: The typical five fiber orientation layers in the injection molding process [5].

The portion of the part thickness each of the layers occupies will change due to geometry, material, fiber concentration, and processing parameters [1]. The variability in the fiber orientation through the thickness causes variation in the mechanical properties of the reinforced

material at different locations, leading to anisotropic properties and non-uniform shrinkage and warpage responses within the part [2]. Generally, homogeneous polymer melts and uniform filler distributions are more desirable for high quality injection molded parts as they offer consistent and reproducible mechanical properties. To this end, some special injection molding processes employ mixing heads or kneading blocks in their screw design to help achieve homogeneity of melt and fibers [6, 7, 8]. However, these screw elements contribute to an increase in shear rate, shear stress, and melt temperature, which can cause degradation to the polymer material and damage to fillers, such as fibers, glass spheres, and biomolecules [9, 10, 11, 12, 13]. Further, in multi-cavity molds complex runner systems can allow for fiber orientation and non-homogeneous material properties to develop prior to the filling of the part cavities. A method of alleviating these issues is to introduce a static mixer that is closer to the molded part into the process. This work discusses and evaluates the use of an "in-runner" static mixer to provide post-plasticizing screw mixing and in-mold control of the fiber orientation.

A helical mixer is a static mixer with several consecutive helical elements [14]. When the helical mixer is used in conjunction with polymer processing, the continuous, laminar melt flow is divided, rotated, and recombined to achieve a homogeneous material distribution while maintaining low shear stress [15, 16, 17]. Various numerical studies and simulations have been developed to analyze the complex flow within this type of mixer, which coincided with experimental data regarding residence time and pressure drop and showed the effectiveness of the helical static mixer [18, 19, 20, 21, 22, 23, 24].

Several concepts of integrating static mixing technology in the injection molding process have been patented and discussed in literature [25, 26, 27] e and some nozzle-based static mixers are already commercially available [28, 29]. The inclusion of a static mixer in the process has shown promising results regarding temperature and mass homogeneity. These solutions all have in common that the mixing device is installed between barrel and mold, which requires investment and significant modification to the standard injection molding machine. By contrast, this work focuses on applications of a static mixer within the runner system.

Runner system melt homogenization techniques have been studied since the 1990s when Beaumont et al. presented the so called "melt flipper" solution to mold filling imbalances in geometrically balanced runner systems [30]. This solution provides homogenization of the melt temperature by shifting a segment of the runner with respect to the parting line, thus providing a

means to correct for thermal (shear heating) effects that occur as the melt is pushed through the runner system [30]. The melt flipper solution, however, does not mix the melt to a great extent so a temperature distribution still exists within the melt [30]. In 2011, Tsai proposed a runner modification specifically designed to increase the melt homogenization for the molding of optical lenses [31]. In particular, a melt restrictor design was introduced within the runner system, which caused the melt profile to change significantly as the melt moved through the narrow segment [31]. Since the geometrically balanced multi-cavity mold used would likely exhibit mold filling imbalance due to thermal effects, the runner restrictor effectively corrected the temperature distribution, so the flow became nearly symmetrical again [31]. To the best of our knowledge, we have not seen applications of complex static mixers, such as the helical static mixer, in the injection mold runner system.

Fiber orientation in the injection molding process has been a topic of extensive research [1, 2, 3, 4, 5]. From developing models to accurately simulate orientation [4], to exploring how the injection molding processing parameters such as injection speed, mold temperature, and packing pressure affect the final orientation [1], there is extensive literature. There are, however, few papers on methods that leverage novel mold geometry to control fiber orientation. Zainudin et al. explained in their review paper the research on the effects of mold thickness and convergent and divergent flows at the melt entrance on fiber orientation, which yield general, simple mold design guidelines for fiber-reinforced parts [1]. The paper by Silva, et al. described a novel rotation, compression, and expansion mold, which allowed for mold movement during the injection molding process [2]. This unusual technology offered a unique control of fiber orientation but at the cost of a specialized mold [2]. Again, we have been unable to find literature on implementing static mixers within the injection mold for fiber reinforced polymer applications.

The goal of this research project is to analyze the influence of a helical static mixer, which could be a disposable plastic mixer or a reusable steel mixer, on the fiber orientation of fiber-filled thermoplastics when integrated directly into the runner system of an injection mold. This approach ideally allows for disruption of the fiber orientation directly before the melt fills the part gate and does not require any changes to the injection molding machine or significant changes to the mold design. The helical static mixer will be assessed both numerically using

injection molding simulation software, Moldex3D, and experimentally with injection molding trials.

2. Simulation and Experimental

2.1 Geometry

Two mold geometries were considered in the computer simulation study, namely, the disk mold (cf. Figure 2) and the two-cavity impact + tensile bar mold (cf. Figure 3). The disk mold was first created to evaluate the potential impacts and benefits of the helical static mixer for injection molding using computer simulation. After promising effects of the helical static mixer were revealed by the simulation software for six different types of neat thermoplastics in terms of density and temperature variations [32], a two-cavity impact + tensile mold was designed and built to experimentally test the process feasibility and benefits of adding a static mixer in injection molding trials. The mold geometries and mixers used in the numerical and experimental studies are summarized in Table 1. The part, runner system, and mixers of these two mold geometries can be seen in Figure 2 and Figure 3, respectively. For these two geometries several mixers were considered, as listed in Table 1.

Table 1: The two mold geometries and various mixer designs evaluated both in simulation and experimental studies.

Mold geometry	**Mixer designs tested in simulation**	**Mixer designs tested in experiments**
Disk mold	• No-mixer • 0.5 mm-thick mixer • 1 mm-thick mixer	NA
Two-cavity Impact + Tensile Bar	• No-mixer • 1 mm-thick straight mixer • 1 mm-thick corner mixer	• No-mixer • 1 mm-thick straight mixer

For the disk geometry mold (cf. Figure 2A) three cases were simulated: no-mixer, 0.5 mm-thick mixer, and 1 mm-thick mixer. The mixer was designed based on a helical static mixer; it was 6 mm in diameter and consisted of six consecutive elements, each measured 10 mm long and had a 20 mm right-handed helical pitch. An example of this geometry is shown in Figure 2B. The runner in Figure 2A was 6 mm in diameter and 100 mm long, which included sufficient length ahead of the mixer to allow for a fully developed stable melt flow. A 1.5 mm by 5 mm

rectangular gate led to a convex-concave disc which had a diameter of 25.6 mm and a thickness of 5 mm.

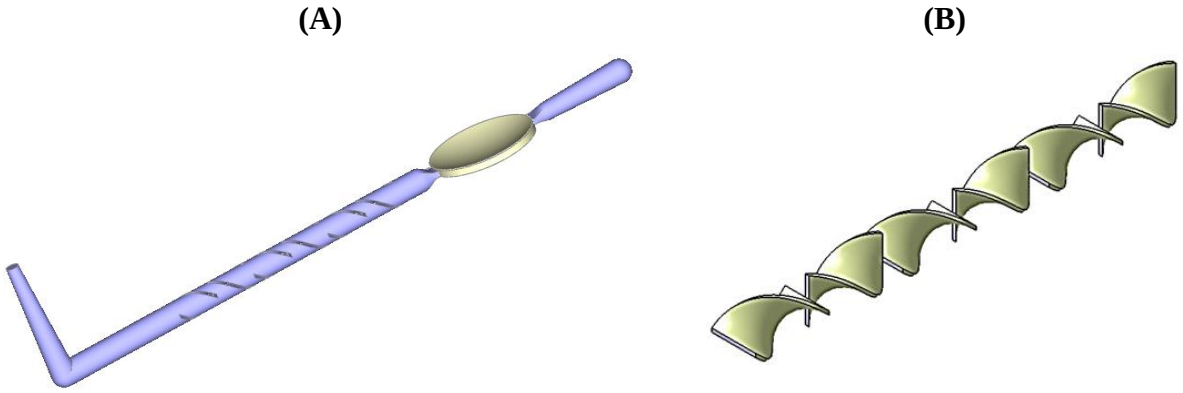

Figure 2: Disk mold with mixer. (A) The tan circular geometry is the disk part, and the blue feature is the runner system. (B) A six-element helical static mixer.

The two-cavity impact + tensile bar mold shown in Figure 3A was used to simulate two different types of mixer geometry and for the physical injection molding experiments. In the simulations and molding experiments, one of the 1 mm-thick mixers was situated at the base of the sprue and ran straight along the runner (cf. Figure 3B and Figure 3D). In further simulation runs, the other 1 mm-thick mixer was located at the corner at the end of the central runner, so the mixing occurred at the corner and closer to the part gate (cf. Figure 3C and Figure 3D). These static mixers were 4.75 mm in diameter with alternating right- and left-handed helical pitch elements which each had a length equal to the 4.75 mm diameter. The straight mixer had 14 elements and the corner mixer had 6 elements total. A no-mixer case was included as a control for both mixer designs and layouts. The first of the two parts was a tensile bar test specimen, which had overall dimensions of 63.5×9.53×3.00 mm, where the 9.53 mm width dimension is located at the widest region of the specimen. The other part was the impact bar test specimen, which was a basic rectangle of 63.5×12.7×3.00 mm. The runners were trapezoidal with the dimensions of 5.7 mm at the top of the runner and 4 mm at the bottom and a height of 4.8 mm. Both gates had a rectangular cross-section with dimensions 3.00×2.00 mm and were slightly off center with respect to the thickness of the part, so the mold parting plane was at the top of the parts. While all the mixer and mold cases were simulated, only the two-cavity impact + tensile mold with straight mixer and no-mixer cases were tested in injection molding trials.

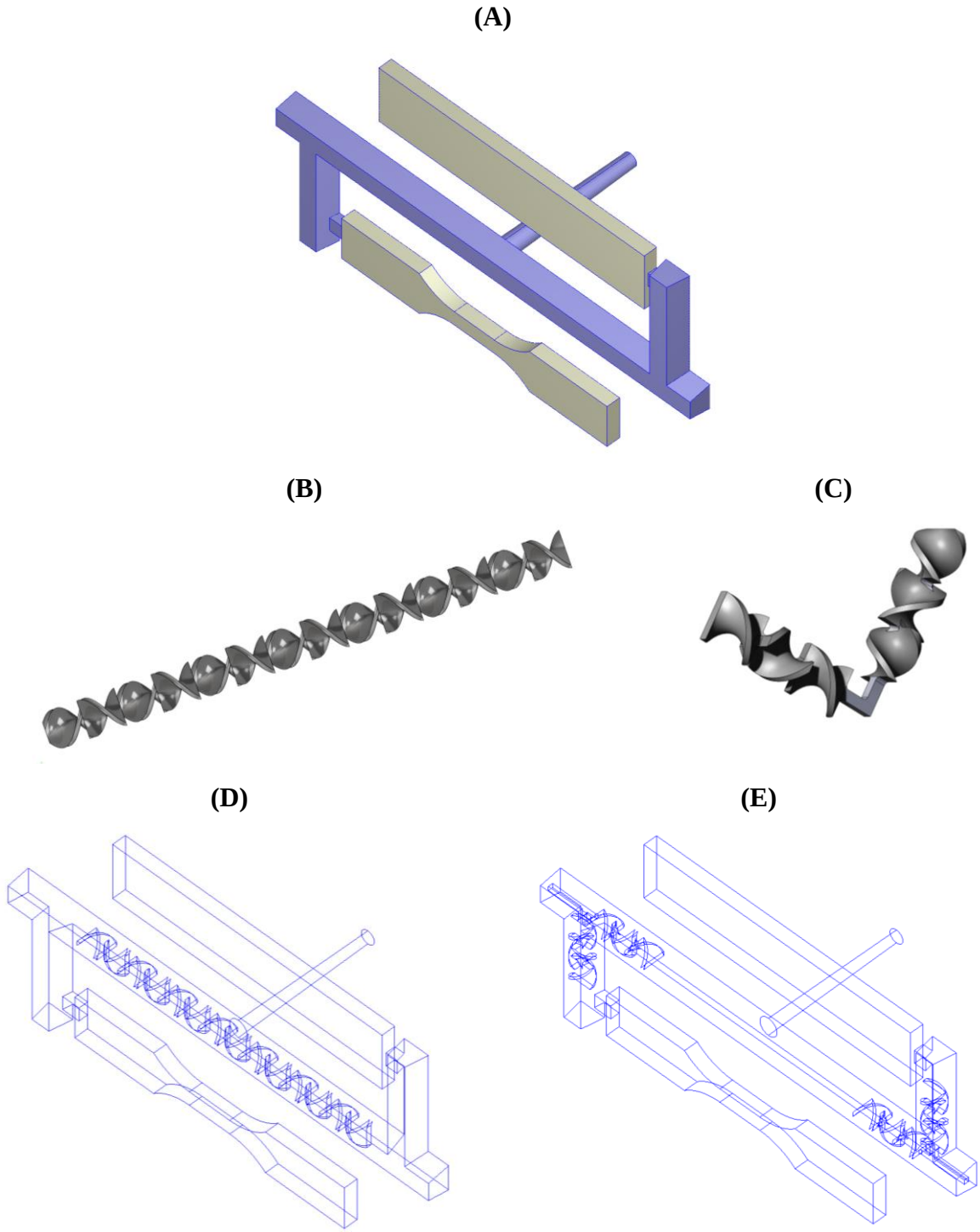

Figure 3: Two-cavity impact + tensile bar mold. (A) Overall mold cavity: tan geometry are the parts and blue geometry are the runners. (B) Straight helical mixer. (C) Corner helical mixer. (D) Line drawing of the straight helical mixer within the mold. (E) Line drawing of the corner helical mixer within the mold.

2.2 Volume Ratio

To compare the restriction of flow more easily within the runner between different molds and mixers, a non-dimensional unit volume ratio is proposed and described in Equation (1).

$$
\begin{aligned}
R_V &= \frac{V_R - V_m}{V_R} \\
R_V &= Unit\ Volume\ Ratio\ (w.r.t.\ runner) \\
V_R &= Volume\ of\ runner\ in\ region\ of\ mixer \\
V_m &= Volume\ of\ mixer
\end{aligned}
\tag{1}
$$

The unit volume ratio is determined with respect to the runner. Thus, it describes the percentage of the runner that remains after the mixer is installed within the mold. Since the length of the runner used in the runner volume is equal to the mixer length, this calculation does not take into consideration the length of the mixer, i.e., the unit volume ratio will be the same for a three-element mixer as a six-element mixer if all other geometry features are the same. The ratio is calculated by subtracting the volume of the mixer from the volume of the runner (in the region of the mixer) and dividing by the original volume of the runner.

The disk mold was simulated with an 80, 90, and 100% volume runner ratio corresponding to the 1-mm thick mixer, 0.5-mm thick mixer, and no-mixer cases, respectively. The two-cavity impact + tensile bar mold was simulated with an 80, and 100% volume runner ratio corresponding to the 1-mm thick mixer and no-mixer cases, respectively. The volume ratio for the molding experiment matches the volume ratio for the two-cavity impact + tensile bar mold simulations.

2.3 Materials

2.3.1 Simulations

Two polypropylene (PP) materials were used in the simulations, one with glass fiber and one without. The materials selected from the Moldex3D material database are:

- Polypropylen (PP): A. Schulman, POLYFORT FIPP XSR5000
- Polypropylene + 40% glass fiber (PP40GF): A. Schulman, POLYFORT FPP 40 GFC SHI

In the simulations, the mixers were assumed to be the same material as the mold, namely, tool steel.

2.3.2 Experiments

In the molding experiment, due to the constraints of available resins, a polypropylene (PP) material (Lyondell Basell, Pro-Fax SR256M) was used with the addition of approximately 20 wt% glass fiber to create sample parts with and without the static mixer.

The mixers used were polyacetal/polyoxymethylene (POM) material donated by Stamixco for this experiment. The mixers matched the geometry of the straight mixers in the simulations as shown in Figure 3B and Figure 3D.

Due to the supply chain disruption caused by Covid-19, different grades of PP were used for the simulations and experiment since the experimental material is not included in the Moldex3D material library and the materials used in the simulation were not available for experiments. However, it was found that both PPs followed similar trends in the results, so it was deemed an acceptable solution.

2.4 Meshing and Simulation Runs

The finite element simulation software, Moldex3D, was used to investigate the effects of a helical static mixer in a runner system on the injection molded parts. The geometry was meshed using a boundary layer meshing scheme with a reasonable uniform mesh density for each geometry case. The simulations were run with the processing parameters shown in Table 2. Note that the Filling Time varies depending on the volume of the mold geometry. For the mixer cases, that volume is equal to the no-mixer mold geometry minus the mixer volume. The Melt Temperature varies based on the material simulated. Polypropylene without glass fiber is recommended to run at a higher temperature than polypropylene with glass fiber. A maximum injection pressure of 140 MPa was specified in the simulation.

Ten simulation runs with varying geometry and material were completed and are tabulated in Table 3. The plots and tables of results in the Results and Discussion section follow the same naming convention for each case.

Table 2: Processing parameters used for the simulation runs.

	Disk Mold: No-mixer 0.5-mm thick mixer 1-mm thick mixer (PP40GF, PP)	**Two-cavity Impact + Tensile Bar Mold: No-mixer 1-mm thick straight (PP40GF)**	**Two-cavity Impact + Tensile Bar Mold: No-mixer 1-mm thick corner (PP40GF)**
Filling Time (sec)	0.25, 0.22, 0.24	0.38, 0.36	0.38, 0.36
Packing Time (sec)	3	3	3
Melt Temperature (°C)	210, 230	210	210
Mold Temperature (°C)	55	55	55
Cooling Time (sec)	10.6	11.0	11.0

Table 3: Simulation runs and legend of simulation cases.

Case	**Mold**	**Mixer**	**Material**
1	Disk	0.5-mm thick straight	PP40GF
2	Disk	1-mm thick straight	PP40GF
3	Disk	No-mixer	PP40GF
4	Disk	0.5-mm thick straight	PP
5	Disk	1-mm thick straight	PP
6	Disk	No-mixer	PP
7	Two-Cavity Impact + Tensile Bar	1-mm thick straight	PP40GF
8	Two-Cavity Impact + Tensile Bar	No-mixer	PP40GF
9	Two-Cavity Impact + Tensile Bar	1-mm thick corner	PP40GF
10	Two-Cavity Impact + Tensile Bar	No-mixer	PP40GF

2.5 Measuring Fiber Orientation

Samples from the molded parts were cut at the approximate locations as shown in Figure 4. These samples were scanned using a ZEISS Metrotom 800 µCT (Carl Zeiss AG, Oberkochen, Germany) scanner. Within the runner the sample thickness with respect to the flow direction was thicker so 40 scanned images through the thickness were gathered and analyzed. Within the

samples from the tensile bar part the flow direction was thinner so only 20 slices through the thickness were considered for analysis. The µCT scan settings are given in Table 4.

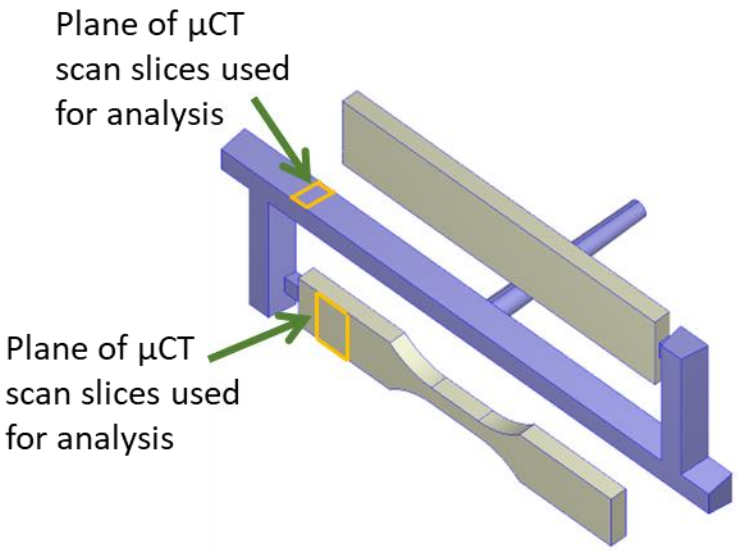

Figure 4: Locations where µCT scanning samples were cut out of the molded part and runner.

Table 4: µCT scan parameter values.

Variable	Value
Voltage (kV)	75
Current (µA)	100
Integration Time (ms)	1000
Gain (-)	8
Number of Projections (-)	2200
Resolution (nm)	4
Scan Time (hr)	2.5

For each sample three directions of cross-sectional image slices were generated, thereby yielding full 3D results. Since the focus of this work is the orientation of the fibers along the flow direction, only 2D images in the flow and thickness directions will be presented. Figure 5A shows an unedited, representative µCT scan image displaying a slice from one of the tensile bar parts. To prepare to quantify the orientation, the scanned images were processed using MATLAB. First, they were cropped to a more uniformed rectangle and then binarized and

denoised to yield a greater definition between the fibers and polymer. The MATLAB-edited version of Figure 5A is shown in Figure 5B.

(A)

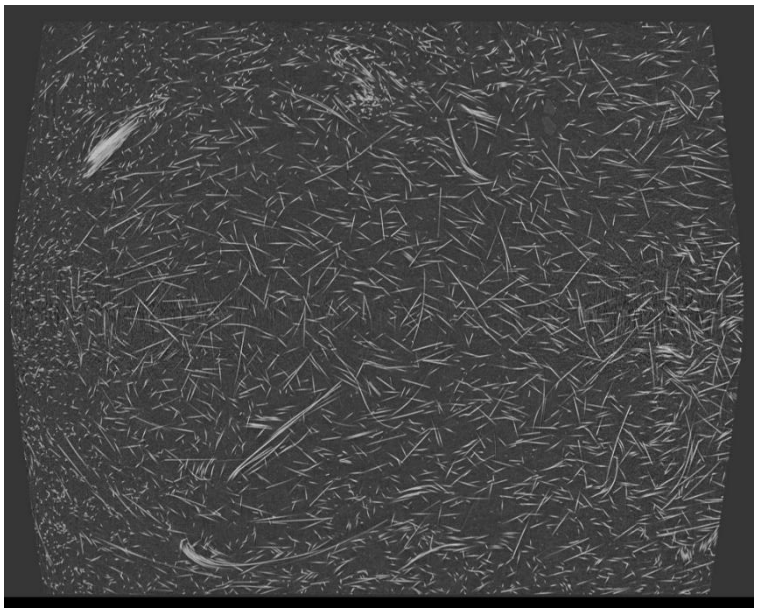

(B)

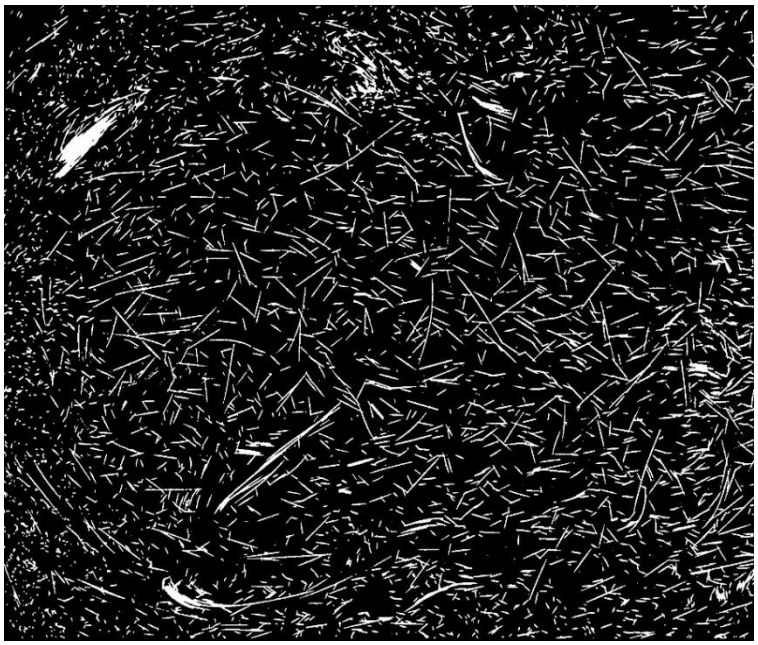

Figure 5: (A) An unedited image from the µCT scan. The polymer flows from left to right. (B) The MATLAB-edited sample cross section µCT scan image based on Figure 5A.

In Figure 5B the fibers, being denser, show as lighter lines in the black, less dense polymer matrix as the background. The orientation of the fibers in the 2D images were then analyzed using the image processing package Fiji [33]. As was shown in Figure 4, it was chosen to analyze the orientation along the flow direction in the tensile bar parts near the gate and in the runner system after the mixer location to determine the effectiveness of the mixer in changing the fiber orientation. To quantify the fiber orientation on a 2D image, the orientation of each of the fibers was determined relative to a global coordinate system where 0° equaled fibers aligned in the flow direction and 90° or -90° equaled fibers perpendicular to the flow. Then, each fiber's orientation angle was plotted in a histogram. This histogram was analyzed to determine the "goodness of fit" to a normal Gaussian function as shown in Equation (2).

$$\begin{gathered} f(x) = ae^{-\frac{(x-b)^2}{2c^2}} \\ f(x) = Gaussian\ fuction\ of\ x \\ a = Height\ of\ the\ curve's\ peak \\ b = Position\ of\ the\ center\ of\ the\ peak \\ c = Standard\ deviation \end{gathered} \tag{2}$$

An example of quantifying the fiber orientation is shown in Figure 6. The Direction is the center point of the Gaussian curve fitted to the data directionality histogram at the bottom of the figure. The Goodness of Fit indicates how well the histogram is fit by the Gaussian curve and can be used to determine the level of alignment along the flow direction. If all the fibers were oriented along the flow direction, the goodness of fit would be 1. If there is less alignment along the flow direction, as with this example, then the goodness of fit is less than 1. The fibers in the image are color coded to indicate their orientation angle following the color scale shown on the right. Based on the cross-section fiber orientation image shown in Figure 6, it has a Direction value of -1.37° and a Goodness of Fit value of 0.59. Comparing to the extremely tedious traditional approach of analyzing all of the fibers and their cross-sectional shape and area on a 2D polished plane to determine the fiber orientation distribution tensor coefficients, this goodness of fit approach is much quicker and more efficient.

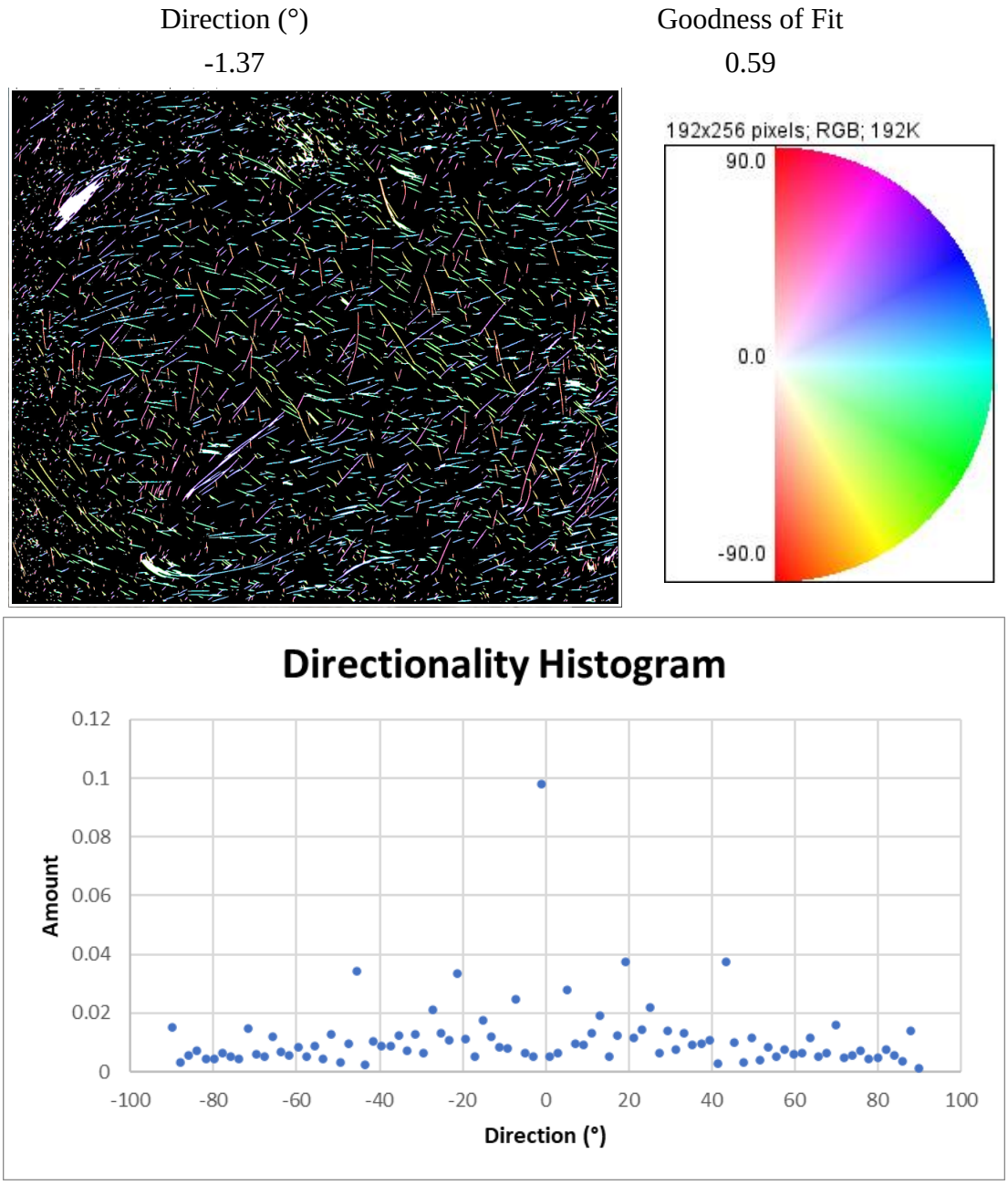

Figure 6: Sample orientation analysis of fibers based on the cross-section image shown above.

3. Results and Discussion

3.1 Simulations

3.1.1 Pressure

Figure 7 shows the sprue pressure versus time during the filling stage. Figure 7A shows the runs with the disk mold (cf. Cases 1-6 in Table 3). The plot shows that the fiber-reinforced PP requires higher pressure and, the thicker the mixer, the higher the required sprue pressure.

(A)

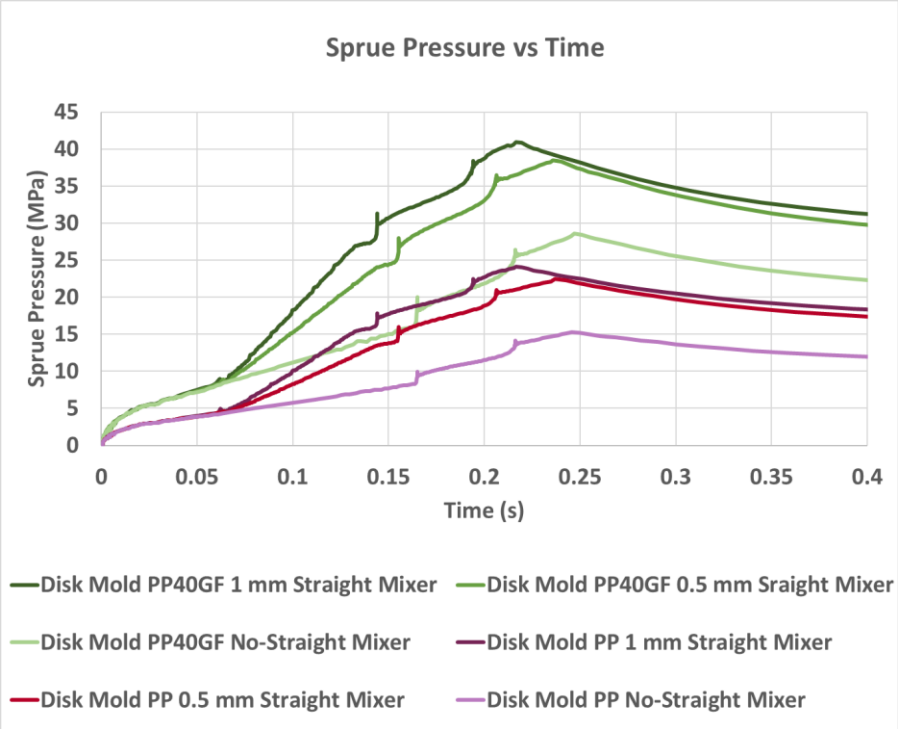

(B)

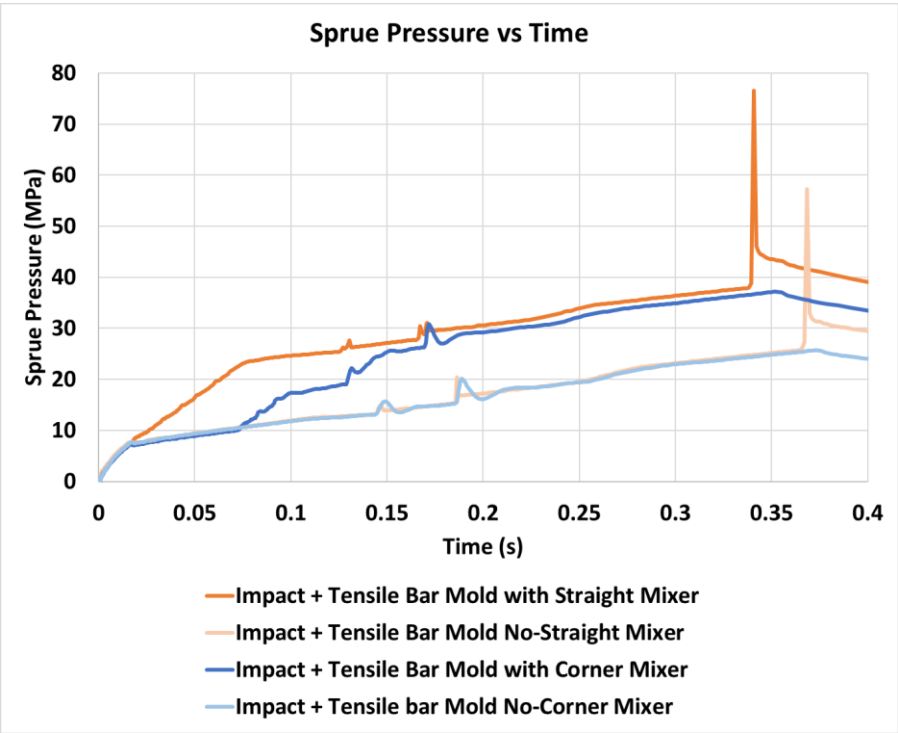

Figure 7: Sprue pressure vs cycle time. The injection molding cycle starts at 0 s.

Figure 7B shows the runs with the two-cavity impact + tensile bar mold (cf. Cases 7-10 in Table 3). Both mixers (straight and corner) require higher pressure than the no-mixer cases. The two no-mixer cases were meshed at the same time as their mixer counterparts, thus the small differences in the results are likely due to numerical differences in the meshes and simulation set-up. Comparing the straight and corner mixers in the two-cavity impact + tensile bar mold there is a slight increase in pressure requirements for the straight mixer, which is likely due to the increased number of mixer elements and therefore increased overall mixer length and flow resistance. In general, the mixers require higher injection pressure due to the reduced cross-sectional area they cause, and the thicker mixer requires higher pressure than the thinner mixer.

3.1.2 Temperature

The average temperature and standard deviation of temperature throughout the part for all cases is shown in the first row of results in Table 5, Table 6, Table 7, and Table 8. For all the cases, the mixers cause a reduction in the average temperature at the end of the filling (EOF) stage. This could be due to the increase in conductive heat transfer to the mold and decrease in the melt's thermal mass due to splitting the polymer melt as it flows around the mixer, which was assumed to be made of mold steel. In the disk mold cases, as shown in Table 5 and Table 6 (cf. Cases 1-6 in Table 3), it can be seen that the temperature decrease is less with the 1-mm thick mixer than the 0.5-mm mixer. This could be due to an increase in shear heating due to greater restriction in the runner cross-section. Finally, this result could also be affected by the change in mold volume due to the space the mixer occupies and how this impacts the filling time in the simulation set up as shown in Table 2. Table 7 and Table 8 show that there is not a significant change in the temperature based on different mixers with the same element thickness.

Table 5: Temperature, volumetric shrinkage, and density results from simulations for the disk mold with PP40GF material.

	Case 1		Case 2		Case 3	
	Disk mold, 0.5 mm thick straight mixer, PP40GF		Disk mold, 1 mm thick straight mixer, PP40GF		Disk mold, No-mixer, PP40GF	
	Average	Standard Deviation	Average	Standard Deviation	Average	Standard Deviation
Temperature EOF (°C)	193.2	±39.29	199.1	±31.79	199.6	±32.43
Temperature EOP (°C)	106.7	±23.81	107.7	±23.83	108.9	±24.31
Volumetric Shrinkage EOP (%)	5.625	±2.566	5.707	±2.722	5.719	±2.712
Density EOP (g/cc)	1.159	$\pm 3.352 \times 10^{-2}$	1.157	$\pm 3.404 \times 10^{-2}$	1.157	$\pm 3.394 \times 10^{-2}$

Table 6: Temperature, volumetric shrinkage, and density results from simulations for the disk mold with PP material.

	Case 4		Case 5		Case 6	
	Disk mold, 0.5 mm thick straight mixer, PP		Disk mold, 1 mm thick straight mixer, PP		Disk mold, No-mixer, PP	
	Average	Standard Deviation	Average	Standard Deviation	Average	Standard Deviation
Temperature EOF (°C)	195.6	±41.73	201.7	±36.45	207.6	±39.56
Temperature EOP (°C)	72.39	±8.704	71.80	±8.023	73.80	±10.94
Volumetric Shrinkage EOP (%)	4.301	±1.024	4.988	±1.001	3.534	±1.258
Density EOP (g/cc)	0.8926	$\pm 9.867 \times 10^{-3}$	0.8860	$\pm 9.464 \times 10^{-3}$	0.8995	$\pm 1.185 \times 10^{-2}$

Table 7: Temperature, volumetric shrinkage, and density results from simulations for the two-cavity impact + tensile bar mold with the straight mixer.

	Case 7		Case 8	
	Two-cavity impact + tensile bar mold, 1 mm thick straight mixer, PP40GF		Two-cavity impact + tensile bar mold, No-straight mixer, PP40GF	
	Average	Standard Deviation	Average	Standard Deviation
Temperature EOF (°C)	195.2	±29.57	199.9	±30.63
Temperature EOP (°C)	133.0	±37.75	134.9	±38.84
Volumetric Shrinkage EOP (%)	4.717	±0.8745	4.765	±0.9142
Density EOP (g/cc)	1.128	$\pm 1.981 \times 10^{-2}$	1.128	$\pm 2.030 \times 10^{-2}$

Table 8: Temperature, volumetric shrinkage, and density results from simulations for the two-cavity impact + tensile bar mold with the corner mixer.

	Case 9		Case 10	
	Two-cavity impact + tensile bar mold, 1 mm thick corner mixer, PP40GF		Two-cavity impact + tensile bar mold, No-corner mixer, PP40GF	
	Average	Standard Deviation	Average	Standard Deviation
Temperature EOF (°C)	195.0	±29.54	199.9	±30.59
Temperature EOP (°C)	135.2	±37.68	135.6	±38.26
Volumetric Shrinkage EOP (%)	4.840	±0.9416	4.934	±1.010
Density EOP (g/cc)	1.126	$\pm 1.983 \times 10^{-2}$	1.125	$\pm 2.031 \times 10^{-2}$

Table 5, Table 6, Table 7, and Table 8 also shows the average temperature throughout the part for all the simulation cases at the end of the packing/holding (EOP) stage on the second row of results. The temperature does not vary significantly between mixer or no-mixer cases, suggesting that the effect of mold cooling during the packing/holding stage played a more significant role despite different melt temperature at the end of filling. However, the average temperature still varies based on material and mold geometry.

3.1.3 Volumetric Shrinkage and Density

The third row of results in Table 5, Table 6, Table 7, and Table 8 shows the average volumetric shrinkage at the end of the packing stage and the fourth and final row shows the related results of average density at the end of the packing stage. These results show different trends depending on the inclusion of the glass fiber filler. When the glass fiber is included, there is little change in the average volumetric shrinkage or density with or without the use of a mixer (i.e., cases 1, 2, 3, 7, 8, 9, and 10). However, for the neat PP cases (i.e., cases 4, 5, and 6) the mixer negatively affects the average volumetric shrinkage and density, leading to an increase in volumetric shrinkage and a decrease in density. This is likely due to the additional flow resistances introduced by the mixer that hampered the effectiveness of packing. Considering the standard deviation of the volumetric shrinkage and density values for PP, there is a decrease when a mixer is used. Thus, this could reduce warpage in the part since the part is predicted to shrink in a more uniform fashion. This trend also occurs with PP40GF but is less significant than with PP.

3.1.4 Fiber Orientation

The predicted fiber orientation results for the disk mold are shown in Figure 8 and Figure 9. Figure 8 shows color images of the predicted fiber orientation for the disk part corresponding to Cases 1-3 in Table 3. The images show the disruption of the fiber alignment pattern in the runner when a mixer is used and the slight decrease in alignment within the disk part. The red color indicates regions with strongly aligned fiber orientation (e.g., near the gate and end of the fill) whereas the blue color denotes areas with randomly aligned fiber orientation.

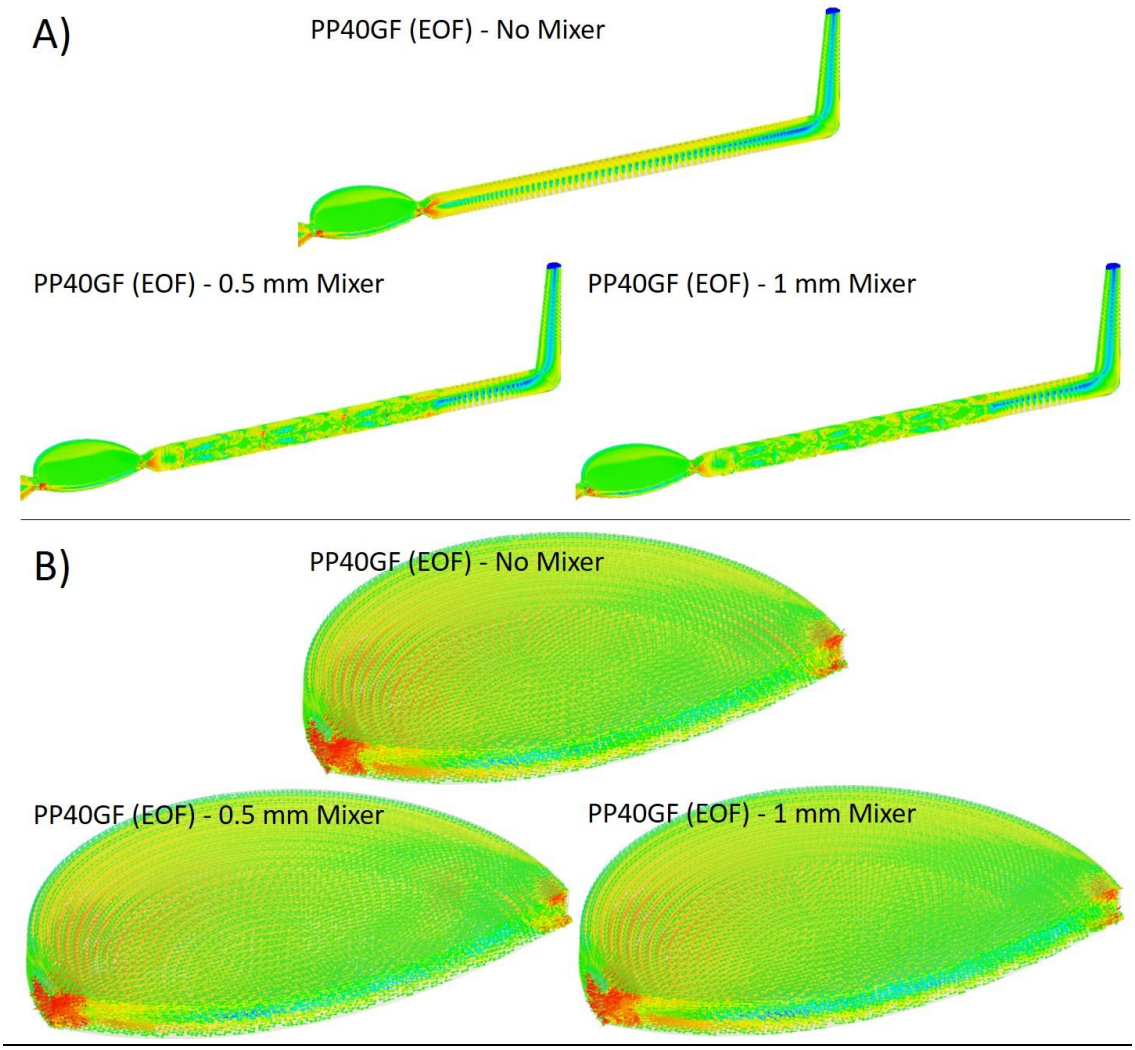

Figure 8: Fiber orientation for disk mold with and without mixer (A) in the runner system and (B) in the part. Red: strongly aligned fiber orientation, blue: randomly aligned fiber orientation.

The orientation is further quantified in Figure 9 for the disk mold and two-cavity impact + tensile bar mold with different mixer designs. Since the 3D fiber orientation simulation was performed, the predicted filler orientation was output in terms of the second-order fiber orientation tensor components [34]. For example, the tensor component corresponding to a_{11}, varies from 1/3 to 1, where 1/3 represents fully random fiber orientation and 1 represents perfectly aligned fibers. Both the disk and two-cavity impact + tensile bar molds show very strong fiber alignment along the flow direction with a slight decrease in fiber alignment when the mixer is present. For the disk mold there is a 2.5% decrease in average orientation when comparing the no-mixer to 0.5 mm mixer cases and 2.3% average orientation decrease for the 1

mm case. The two-cavity impact + tensile bar mold shows a 0.87% average orientation decrease for the straight mixer and a 0.43% average orientation decrease for the corner mixer when compared to their respective no-mixer case. Although both molds show a trend of lower fiber orientation when a mixer is used, the change in orientation within the two-cavity impact + tensile bar mold is much less significant than that in the disk mold.

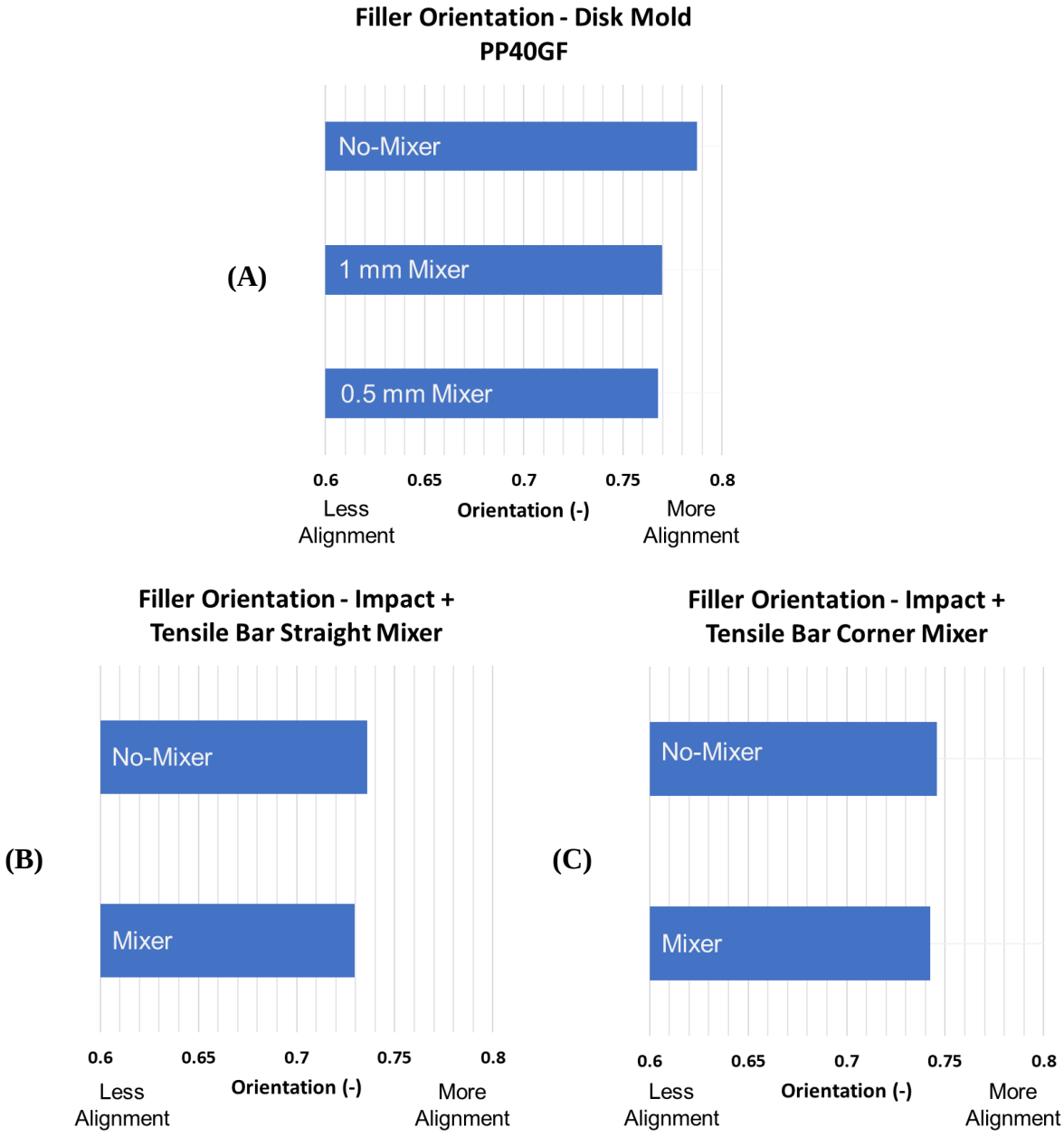

Figure 9: Fiber orientation results as a function of mixer, mold, and material case.

3.2 Experimental Fiber Orientation Data

Based on the physical injection molding experiments, plots showing the goodness of fit or degree of fiber orientation vs. cross sectional slices through the sample were created. Recall that the straight mixer was used in the experiments (cf. Figure 3B and Figure 3D) and samples were taken from the molded parts in the locations shown in Figure 4. These plots are shown in Figure 10, Figure 11, and Figure 12.

It should be noted that the degree of fiber orientation is quantified differently between the simulation and experimental process. For the full 3D simulations, the average orientation is output in terms of the second-order orientation (distribution) tensor components. In contrast, 2D scanned μCT images are obtained from the injection molding trial and analyzed as described in the Simulation and Experimental section. Given the large number of scanned images and numerous fibers on each of the 2D images, the average value of fiber orientation for each image is quantified using the "goodness of fit" to a normal Gaussian function as shown in Equation (2). Despite the different quantification methods, the overall trends of fiber orientation can still be compared for cases with or without a mixer based on the orientation (distribution) tensor component and goodness of fit values to validate the simulation results.

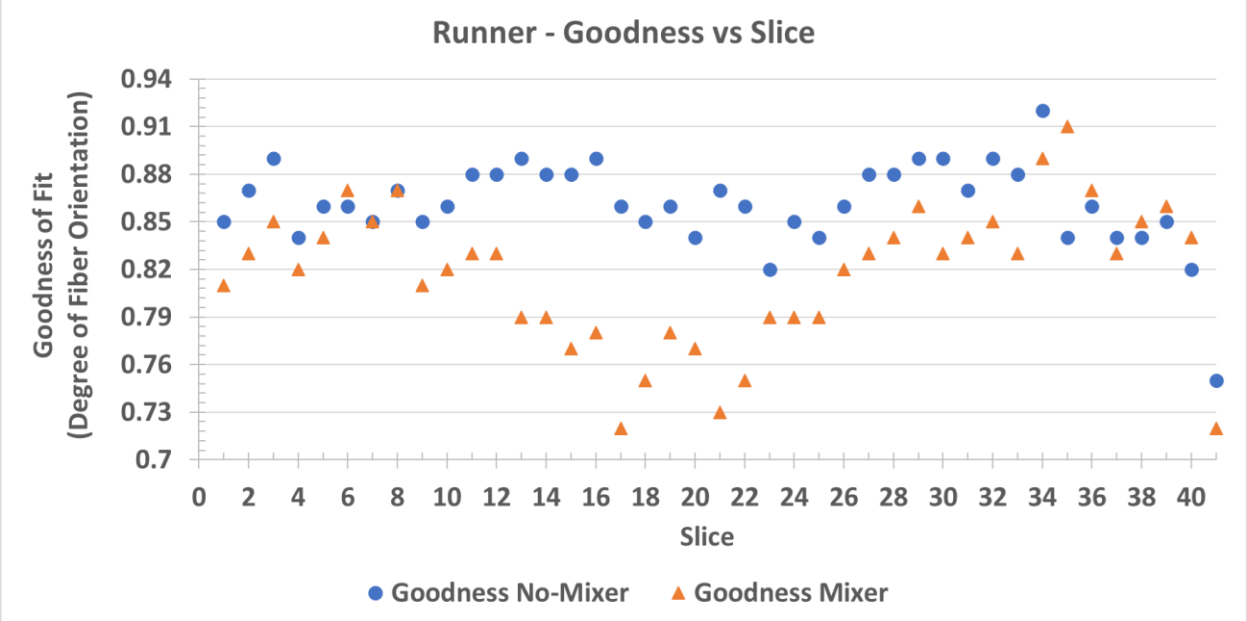

Figure 10: The goodness of fit or degree of fiber orientation as a function of CT-scan slice through the runner system samples with a mixer (triangle symbols) and without a mixer (circle symbols).

(A)

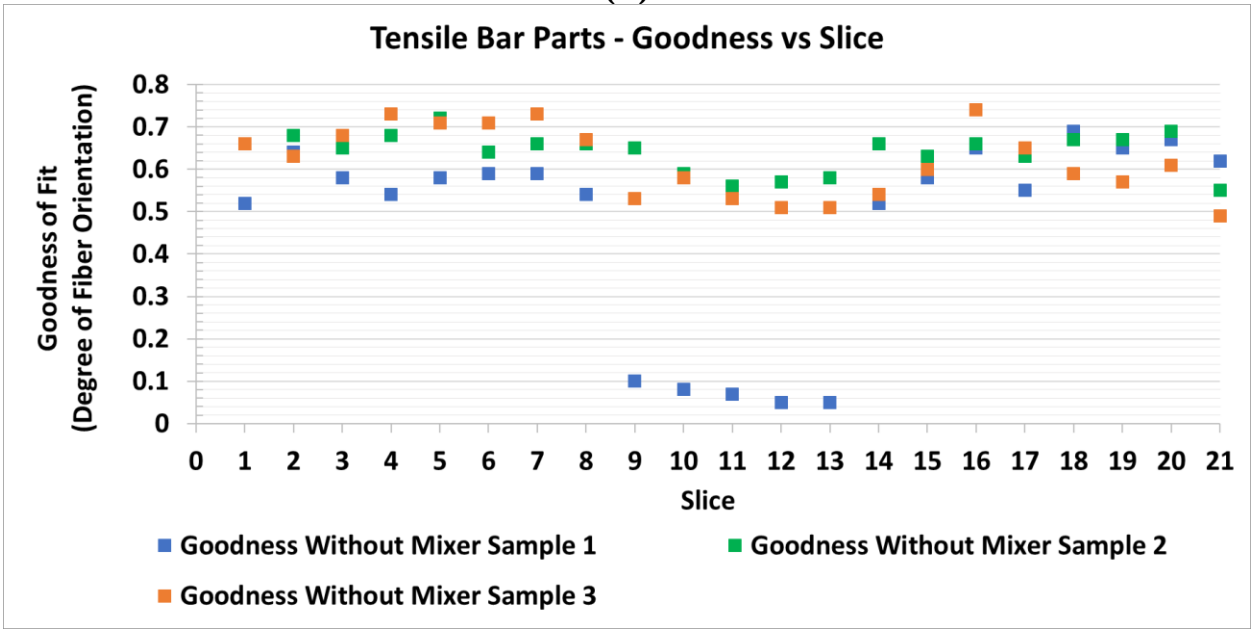

(B)

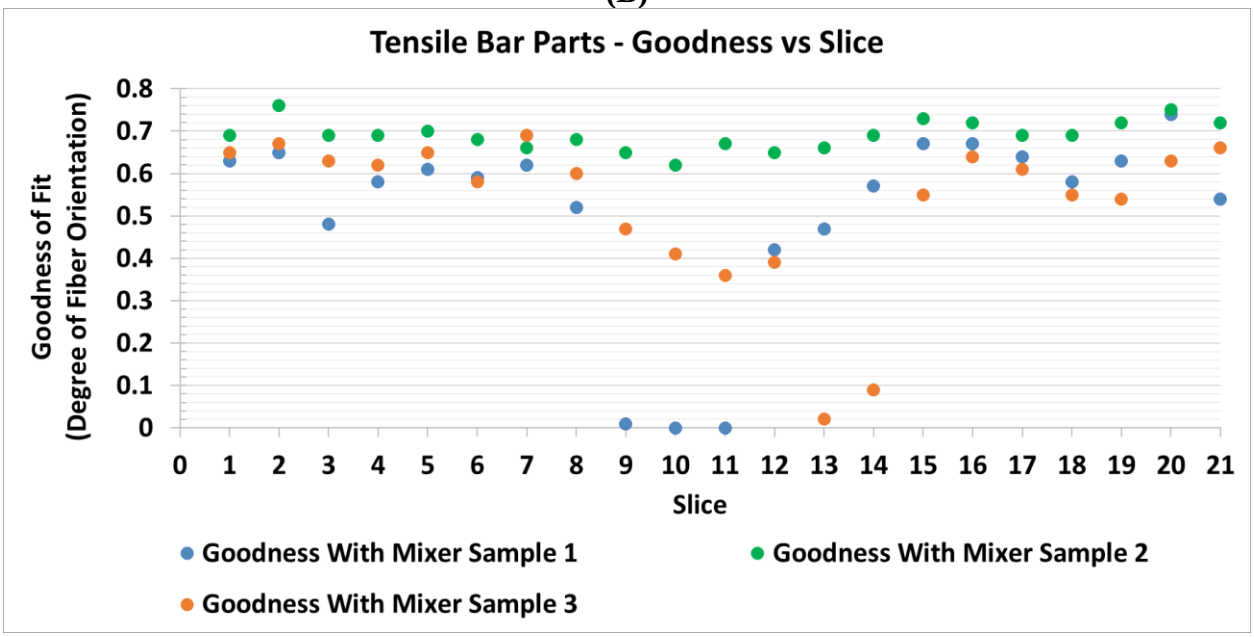

Figure 11: The goodness of fit or degree of fiber orientation as a function of CT-scan slice through the tensile bar part samples: (A) without a mixer and (B) with a mixer.

Figure 10 depicts the fiber orientation within the runner with a straight mixer (triangle symbols) vs a runner without the mixer (circle symbols). In Figure 10 the slices start at the edge of the sample (e.g., Slice 1), go through the core layers in the middle slices (e.g., Slice 20), and end on the opposite edge of the sample (e.g., Slice 41). As expected, the orientation results are

correspondingly symmetric. From the plot there is a noticeable decrease in fiber orientation for a good portion of the runner thickness, especially within the core layer when a mixer is used. There is little change on the surface layers where the fountain flow behavior still dominates. This supports the functionality of the mixer and confirms that the static mixer can successfully disrupt the flow and change the orientation of the fibers, especially in the runner.

To show the repeatability of fiber orientation measurement, Figure 11 plots the data points for the three samples taken at the same part cavity locations (cf. Figure 4) without using the mixer (cf. Figure 11A) and with the straight mixer (cf. Figure 11B).

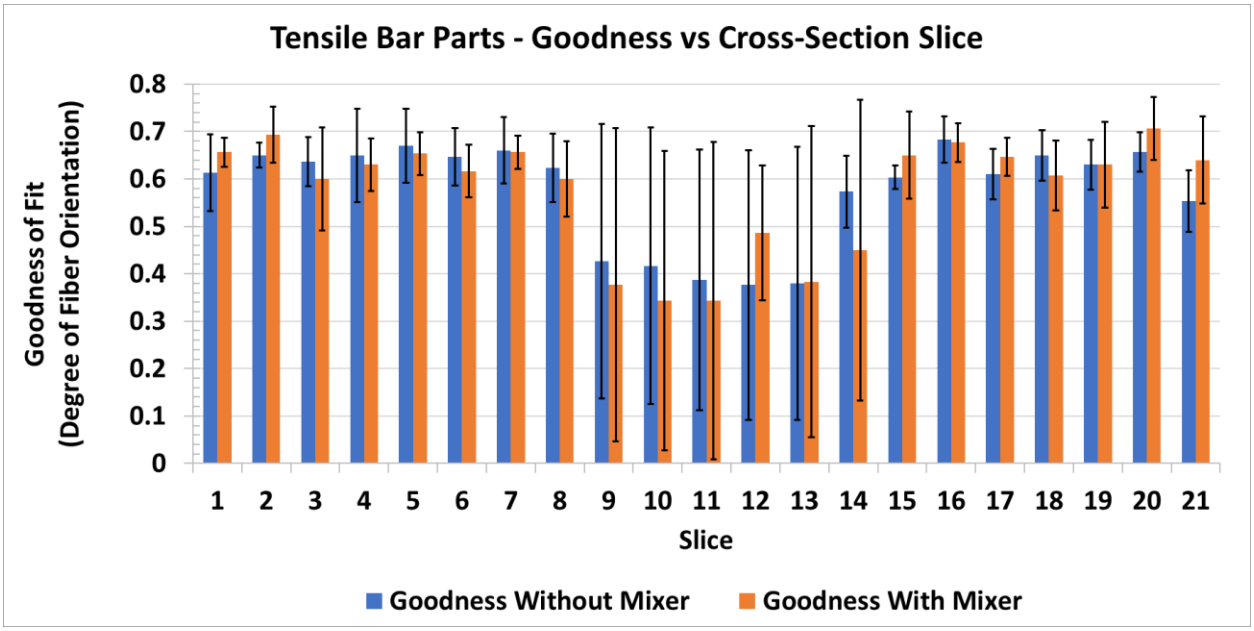

Figure 12: The average goodness of fit or degree of fiber orientation as a function of CT-scan slice through the tensile bar part samples with a mixer (circle symbols) and without a mixer (square symbols). The standard deviation is included as error bars in the plot.

In both plots in Figure 11 the slices start at the edge of the sample (e.g., Slice 1), go through the core layers in the middle slices (e.g., Slice 10), and end on the opposite edge of the sample (e.g., Slice 21). As expected, the orientation results are correspondingly symmetric. There does not appear to be a significant difference between these two plots. This can be more clearly seen in Figure 12, which plots the averaged data and standard deviation taken from Figure 11. From this it can be concluded that there is no significant difference in the fiber orientation through the thickness layers in the parts with or without the use of the mixer, even though fiber orientation is

more random in the runner with the mixer. It is likely that the remaining runner segment post-mixer realigned the fibers to match cases without the mixer. These results suggest that mixing does occur, but fiber realignment will take place post-mixer and offset the effect of the mixer. This agrees with the simulation results for the two-cavity impact + tensile bar mold geometry as previously shown in Figure 9.

4. Conclusion

The use of a static mixer within the runner system in an injection mold with fiber-reinforced polypropylene material was explored with simulations and molding experiments. It was found that the mixers had the expected result of increasing machine injection pressure requirements during the injection stage due to the restriction of flow area in the runners. The mixers had a more complex effect on the temperature results due to the increased conductive cooling and shear heating from the flow restriction. For the general quality parameters of volumetric shrinkage and density at the end of packing the mixers appeared to cause increased shrinkage and decreased density but also yielded improved uniformity in the shrinkage results, thereby, indicating a potential reduction in part warpage when a mixer is used. The mixers successfully disrupted the fiber alignment in the runner, which was shown both in simulations and the molding experiments. There was also a slight decrease in the degree of fiber alignment for the disk mold as predicted in the simulations. However, the degree of fiber alignment was restored to near no-mixer values for the two-cavity impact + tensile bar mold by the time the melt reached the part cavity, yielding diminishing change in the orientation of the fibers within the part. In summary, the use of a static mixer shows potential in allowing for mixing after the plasticizing unit, but its impact in the fiber orientation in the final molded parts will depend on where it is positioned, the number of mixer elements, and the subsequent fiber re-orientation effect.

Chapter 2: Effect of Static Mixer on Optical Properties of Plastic Injection Molded Parts

1. Introduction

Improving the quality and accuracy of injection molded parts has been an objective since the injection molding machine was developed in the nineteenth century [35]. Polymers, and their ability to be molded into an infinite number of shapes, allow for the manufacture of simple plastic products like billiard balls, to complex parts such as micro-camera lenses. In the optical field, the use of polymers versus traditional glass is highly desirable; polymers can be easily manufactured into complex shapes, which are lightweight and readily mass-produced via injection molding and other methods [36]. About a hundred years after the first injection molding machines the materials and process had advanced sufficiently to allow for the manufacture of precision plastic lenses with optical qualities that competed with their glass counterparts [37, 38]. This advancement can be credited to several sources, including the development of optical polymers, the improvement of injection molding machines and machine control, the increased understanding of viscoelasticity and rheology of polymers, and the high-quality standards of the injection molding machine mold. However, there is a limit to the quality improvements that can be obtained in the standard injection molding process due to the inherent properties of the molecular structure of polymers, which cause either geometric or birefringence defects as shown in Figure 13 [39]. To overcome these material and process shortcomings, many novel approaches are pursued to further improve the quality of plastic optic parts. This work explores the approach of adding a static mixer to the runner system of the mold to improve part quality for optical applications.

To aid in the manufacture of high-quality polymer optical components, several novel approaches have been developed. These include process modifications, mold modifications, or combinations of the two. Injection-compression molding, for example, requires specialty molds, which can provide compression action on the part, thus replacing the packing stage in the injection molding cycle [35, 40]. In this way both the injection molding process and mold are modified. Other novel approaches used for plastic optics include rapid heat cycle molding (RHCM) [39], conformal cooling systems [41], micro-injection molding [35], process optimization and/or defect compensation via simulation [42, 43, 44, 45, 46, 47, 48], multi-shot molding [43], and runner modifications to improve melt homogenization [31, 49].

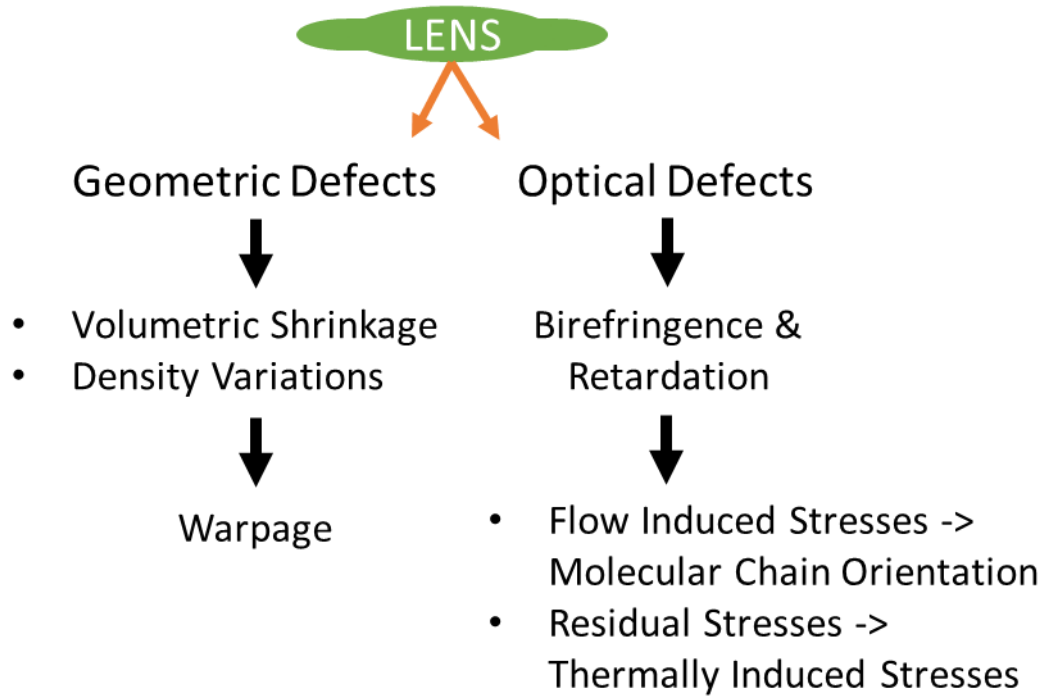

Figure 13: The as-molded defects that occur within an injection molded lens.

This work focuses on the mold modification of adding a reusable metal or single-use plastic static mixer to the runner system of a mold. This approach has a low implementation (capital) cost and, therefore, could be easily utilized as modifications on existing manufacturing lines or as a design choice for new molds. These static mixers would be installed for each cycle or, geometry allowing, could be built into the mold runner and could benefit the molding of various types of plastic parts. For optical applications, the mixer could help to homogenize the melt properties such as temperature distribution and reduce molecular orientation and, therefore, improve the optical properties.

Homogeneous polymer melts and uniform filler distributions are essential for high quality injection molded parts with consistent, uniform, and reproducible mechanical properties. Common injection molding processes employ mixing heads or kneading blocks in their screw design to achieve this task [50, 7, 8]. However, these screw elements contribute to an increase in shear rate, shear stress, and melt temperature, which can cause degradation to the polymer material [9, 10, 11, 12, 13]. Further, in multi-cavity molds complex runner systems can allow for

orientation and non-homogeneous material properties to develop prior to the filling of the part cavity. A method of alleviating these issues is to introduce a static mixer into the process.

Several concepts of integrating static mixing technology in the injection molding process have been patented and discussed in literature [25, 51, 27] and some are commercially available [28, 29]. The inclusion of a static mixer in the process has shown promising results regarding temperature and mass homogeneity. These solutions all have in common that the mixing device is installed between machine barrel and mold, which requires investment and significant modification to the standard injection molding machine. One static mixer of particular importance is a helical mixer, which is a static mixer with several consecutive helical elements [14]. The continuous, laminar flow is divided, rotated, and recombined to achieve a homogeneous material distribution while maintaining low shear stress [15, 16, 17]. Over the last 60 years, various numerical studies and simulations have been developed to analyze the complex flow within this type of mixer. The results coincided with experimental data regarding residence time and pressure drop and showed the effectiveness of the helical static mixer [18, 19, 20, 21, 22, 23, 24].

Runner melt homogenization techniques have been studied since the 1990s when Beaumont et. al. presented the “melt flipper” solution to mold filling imbalances in geometrically balanced runner systems [30]. This solution provides homogenization of the melt temperature by shifting a segment of the runner with respect to the parting line, thus providing a means to correct for thermal effects that occur as the melt is pushed through the runner system [30]. The melt flipper solution, however, does not mix the melt to a great extent so a temperature distribution still exists within the melt [30]. In 2011, Tsai presented a runner modification specifically designed to increase the melt homogenization for the molding of optical lenses [31]. Tsai produced a melt restrictor design within the runner system, which caused the melt profile to change significantly as it was moved through the narrow segment [31]. Since the geometrically balanced multicomponent mold used would likely exhibit mold filling imbalance due to thermal effects, the runner restrictor effectively corrected the temperature distribution, so it is nearly symmetrical again [31]. The author then completed both simulation and molding experiments showing the geometric stability improvements with the restrictor and concluded that the runner restrictor reduced the as-molded warpage within the lens part [31]. Still, this method does not mix the melt to a great extent and does not consider any optical properties, such as birefringence.

The goal of this research project is to analyze the influence of static mixers on the melt homogeneity and part quality when integrated directly into the runner system. This approach allows for homogenization of the melt properties directly before the melt fills the part gate and does not require any changes to the injection molding machine or significant changes to the mold design. To the best of our knowledge, there has been no public literature on the influence of static mixers within the runner system on the filling behavior and optical quality of plastic parts. In this study, the effects of static mixers on the quality of plastic parts will be evaluated through both injection molding simulations and experiments.

2. Experimental and Simulations

2.1 Geometry

A two-cavity impact + tensile bar mold shown in Figure 3 was used for this study. In previous work a disk mold was created to evaluate the potential impacts and benefits of the helical static mixer for injection molding using computer simulation. After promising effects of a helical static mixer were revealed by the simulation software for six different types of neat thermoplastics in terms of density and temperature variations [32], the two-cavity impact + tensile mold with trapezoidal cross section runners was designed and built to experimentally test the process feasibility and benefits of adding a static mixer in injection molding trials. Two runner types and several mixer designs were considered in the study. These are summarized in Table 1. Two circular runner types with equivalent hydraulic radii were used to allow for meshing of the complex helical static mixers with a high quality hybrid meshing method for the molding simulation.

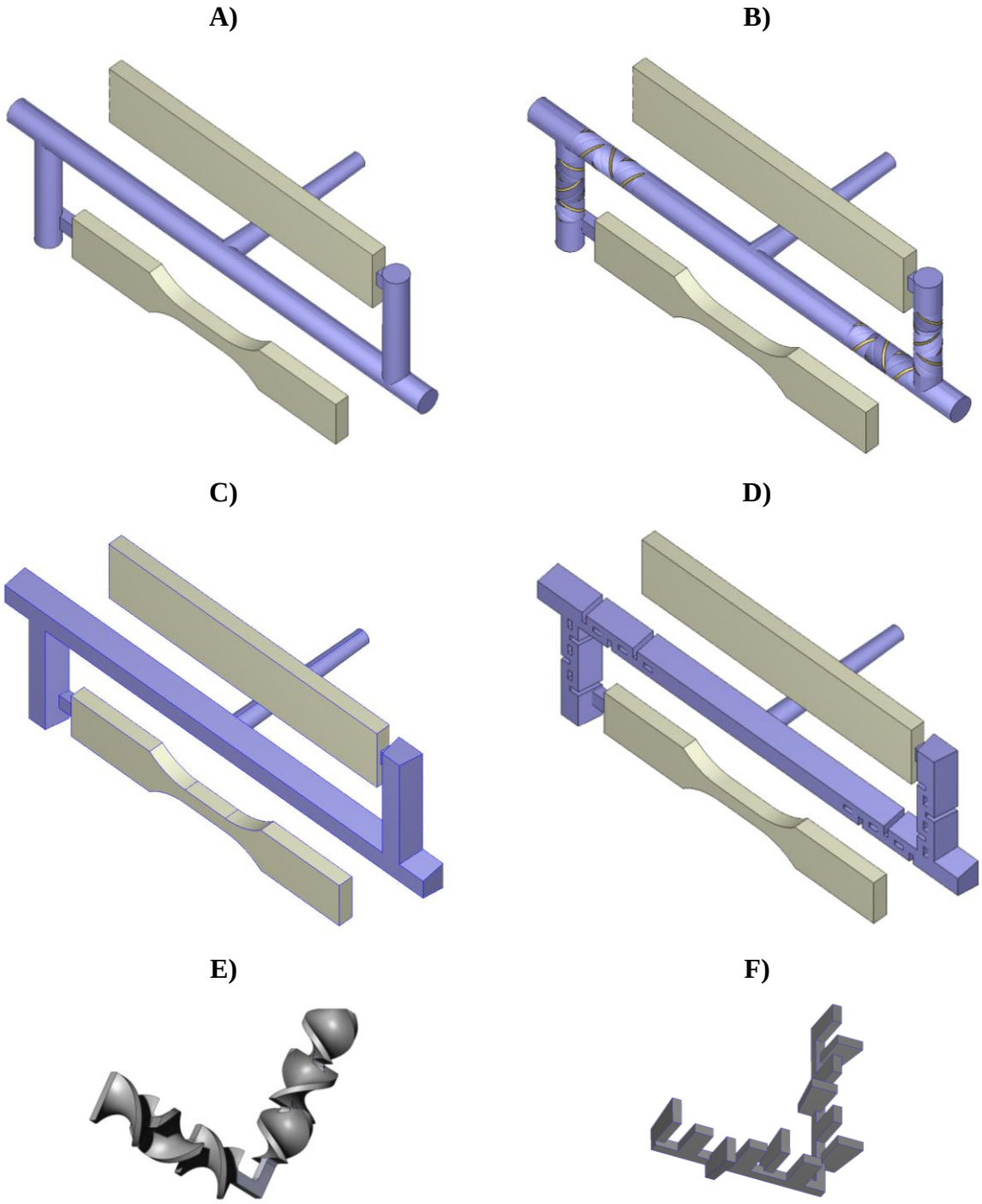

Figure 14: The mold and mixer geometries considered in the study. (A) and (B) show the circular runner mold geometry used in the simulations without and with a helical mixer. (C) and (D) show the trapezoidal runner mold geometry used in the simulations and molding experiments without and with a built-in mixer. (E) and (F) show the 3D printed mixers (helical and built-in, respectively) used in the molding experiments.

Two mixer styles were considered with the two-cavity impact + tensile bar mold shown in Figure 3. Two mixers were installed each cycle within the mold and were located at the corners of the runner. The first mixer assessed was a helical static mixer with a 4.75 mm diameter and alternating right- and left-handed helical pitch elements. Each element had a length equal to the 4.75 mm diameter and each mixer had 6 elements. The second mixer was the built-in mixer, which was designed based on the geometry of the helical mixer while being a permanent mold feature within the mold and still allowing for ejection. These mixers had fins alternating parallel and perpendicular to the flow of the polymer melt. Considering each pair of fins to be equivalent to one helical mixer element, the built-in mixer also had 6 elements. To allow for testing with an existing mold the built-in mixer idea was converted into the geometry as shown in Figure 3F, which could be 3D printed and added into the runner system for each cycle. A no-mixer case was included as a control for both mixer designs and layouts.

Table 9: Simulation and experimental runs considered in study.

Case	Mold Runners	Mixer Geometry	Simulation Run	Experimental Run
1	Circular	No-Mixer	Yes	No
2	Circular	1 mm Helical Mixer	Yes	No
3	Circular	0.75 mm Helical Mixer	Yes	No
4	Circular	0.5 mm Helical Mixer	Yes	No
5	Trapezoidal	No-Mixer	Yes	Yes
6	Trapezoidal	1 mm Built-In Mixer	Yes	Yes
7	Trapezoidal	0.5 mm Built-In Mixer	No	Yes
8	Trapezoidal	1 mm Helical Mixer	No	Yes
9	Trapezoidal	0.5 mm Helical Mixer	No	Yes
10	Trapezoidal	No-Mixer No-Packing Stage	No	Yes

Within the mold the first of the two parts was a tensile bar test specimen, which had overall dimensions of 63.5×9.53×3.00 mm, where the 9.53 mm width dimension is located at the widest

region of the specimen. The other part was the impact bar test specimen, which was a basic rectangle of 63.5×12.7×3.00 mm. Both gates had a rectangular cross-section with dimensions 3.00×2.00 mm and were slightly off center with respect to the thickness of the part, so the mold parting plane was at the top of the parts. The runners were either trapezoidal with the dimensions of 5.7 mm at the top of the runner and 4 mm at the bottom and a height of 4.8 mm or circular with an equivalent hydraulic diameter of 4.8 mm. Due to limitations in meshing, the simulations of the helical static mixers used the circular runners (cf. Figure 2B) but the corresponding experiments were completed with trapezoidal runners (cf. Figures 2C and 2E). For the built-in mixers, the trapezoidal runners were used for experiments and simulations (cf. Figures 2D and 2F).

2.2 Hydraulic Diameter Calculation

To allow for reasonable optical simulations, a hybrid meshing scheme was used consisting mostly of hexagonal elements. To build this mesh with the helical static mixer the runner cross-section was converted from trapezoidal to circular by using equivalent hydraulic diameters. The calculation of the hydraulic radius is given by Equation (3).

$$\begin{aligned} R_h &= \frac{2A}{P} \\ R_h &= Hydraulic\ Radius \\ A &= Cross-Sectional\ Area \\ P &= Wetted\ Perimeter \end{aligned} \tag{3}$$

This calculation takes two times the cross-sectional area and divides it by the wetted perimeter. For a circular cross section, the hydraulic radius is equal to the actual radius. Isaev et al. showed that the hydraulic radius can be a reasonable value to relate polymer flow through cannels of varying cross-sections [52]. For the trapezoidal runner, the geometry parameters and corresponding hydraulic radius and diameter are given in Table 10. The calculated hydraulic diameter was then used for the circular cross-section runner.

Table 10: The cross-sectional geometry of the trapezoidal runner and corresponding hydraulic radius and diameter.

Trapezoidal Runner	
Height (mm)	4.8
Width at Top (mm)	5.7
Width at Bottom (mm)	4.0
Cross-Sectional Area (mm^2)	23
Wetted Perimeter (mm)	19
Hydraulic Radius (mm)	2.4
Hydraulic Diameter (mm)	4.8

2.3 Volume Ratio

To compare the restriction of flow more easily within the runner between different molds and mixers, a non-dimensional unit volume ratio is proposed and described in Equation (1).

$$\begin{aligned} R_V &= \frac{V_R - V_m}{V_R} \\ R_V &= Unit\ Volume\ Ratio\ (w.r.t.\ runner) \\ V_R &= Volume\ of\ runner\ in\ region\ of\ mixer \\ V_m &= Volume\ of\ mixer \end{aligned} \tag{4}$$

The unit volume ratio is determined with respect to the runner. Thus, it describes the percentage of the runner that remains after the mixer is installed within the mold. Since the length of the runner used in the runner volume is equal to the mixer length, this calculation does not take into consideration the length of the mixer, i.e., the unit volume ratio will be the same for a three-element mixer as a six-element mixer if all other geometry features are the same. The ratio is calculated by subtracting the volume of the mixer from the volume of the runner (in the region of the mixer) and dividing by the original volume of the runner.

The various cases and their corresponding volume ratios are summarized in Table 11. Due to the changes in the cross-sectional area between the trapezoidal and circular runners the volume ratio changes slightly between runners with the same mixer. The lowest volume ratio, and, therefore, the greatest cross-sectional restriction of flow by the mixer, was the circular runner with the 1 mm helical mixer at 74.2%. The highest volume ratio, and, thus, the lowest cross-

sectional restriction of flow by the mixer, was the trapezoidal runner with the 0.5 mm built-in mixer at 91.6%.

Table 11: The calculated unit volume ratio for the various mold and mixer cases.

Unit Volume Ratio (%)			
Helical Mixers			
Runner Type	**1 mm**	**0.75 mm**	**0.5 mm**
Trapezoidal	79.5	84.7	89.8
Circular	74.2	80.6	87.1
Built-In Mixers			
Runner Type	**1 mm**		**0.5 mm**
Trapezoidal	83.2		91.6
Circular	78.2		89.1

2.4 Materials

2.4.1 Simulations

A commercial finite element injection molding simulation software package, Moldex3D, was used for the simulations. The PS material selected from the Moldex3D material database was BASF Polystyrol 456 M PS. The helical mixers material selected from the Moldex3D database was assumed to be Generic CAE Epoxy EMC-1. The built-in mixer material was assumed to be the same as the mold material, i.e., tool steel.

2.4.2 Experiments

In the molding experiment, due to the constraints of available resins, a polystyrene (PS) material (GE Polymerland 708300 PS) was used to produce sample parts with and without the static mixer. The mixers used were 3D printed using a Formlabs Stereolithography (SLA) printer with a Formlabs High Temp thermoset resin.

It was necessary to use different grades of PS for the simulations and experiment since the experimental material is not included in the Moldex3D material library. However, it was found that both PS grades followed similar trends in the results, so it was deemed an acceptable assumption.

2.5 Meshing and Simulation Runs

The finite element simulation software was first used to investigate the effects of a helical static mixer in a runner system on the injection molded parts. The geometry was meshed in

Rhino 5 with the Moldex3D plug-in using a hybrid meshing scheme with fully solid mesh. Primarily, high quality Hexa elements were used with Prism elements used sparingly.

The simulation parameters for each of the six simulation runs are tabulated in Table 12. To compare between geometry cases the processing parameters were held constant where possible. Since the mixer and runner geometry change the overall volume of the mold there are differences in the filling stage parameters and the meshing parameters between cases.

Table 12: Simulation set-up and processing parameters.

Mixer Type	1 mm Built-In Mixer	No-Mixer	0.5 mm Helical Mixer	0.75 mm Helical Mixer	1 mm Helical Mixer	No-Mixer
Runner Type	Trapezoidal	Trapezoidal	Circular	Circular	Circular	Circular
	Case 6	**Case 5**	**Case 4**	**Case 3**	**Case 2**	**Case 1**
Filling Stage						
Stroke Time (sec)	0.73	0.75	0.67	0.66	0.66	0.69
Flow Rate (cc/sec)	10	10	10	10	10	10
Injection Volume (cc)	17.1	17.4	16.4	16.4	16.3	16.6
Injection Pressure (MPa)	150	150	150	150	150	150
V/P Switch-Over and Packing Stage						
V/P Switch-Over By Ram Position (mm)	1	1	1	1	1	1
Packing Time (sec)	3	3	3	3	3	3
Packing Pressure (MPa)	50	50	50	50	50	50
Process Temperatures						
Melt Temperature (ºC)	225	225	225	225	225	225
Mold Temperature (ºC)	38	38	38	38	38	38
Meshing						
Prism Element Count	1,720	0	0	0	0	0
Hexa Element Count	278,944	178,985	302,760	302,760	270,718	291,816

a. Injection Molding Set-up

The injection molding experiments were completed using an Arburg Allrounder 270 A machine with the processing parameters described in Table 13. They were completed in two runs (First and Second) and the results were compared between the different runs to ensure repeatability. Additionally, during the second run the samples were taken in groups of five, switching between mixer and no-mixer cases to assess the stability of the results during the molding run.

Table 13: Injection molding machine information and process parameter settings.

Arburg Allrounder 270 A 38 tons e^2 Alldrive	
Injection Rate (cc/s)	10
Hopper to Nozzle Temperature Profile (^oC)	20-200-225-225-225
Mold Temperature (^oC)	38
Switch-Over Volume (cc)	3.2
Packing Time (sec)	3
Packing Pressure (MPa)	50
Cooling Time (sec)	30

b. Birefringence Measurements

To measure the optical properties of the samples a custom-made birefringence measurement studio was devised. Birefringence and retardation, i.e., birefringence multiplied by the sample thickness, were chosen as the optical parameters of note for both the injection molding experiments and simulations. The values of birefringence and retardation are minimized for improved optical quality. To complete these measurements, a measurement studio was created. A schematic of the studio is shown in Figure 15.

The optical properties measurement studio is based on the concept of a polariscope with two polarized films/filters surrounding a sample. By shining light through the polarized films/filters and part the birefringence can be visualized as rainbow colors, which can be quantified and compared between samples. To create the photographs for analysis, a Nikon camera was used with the settings and attachments described in Table 14.

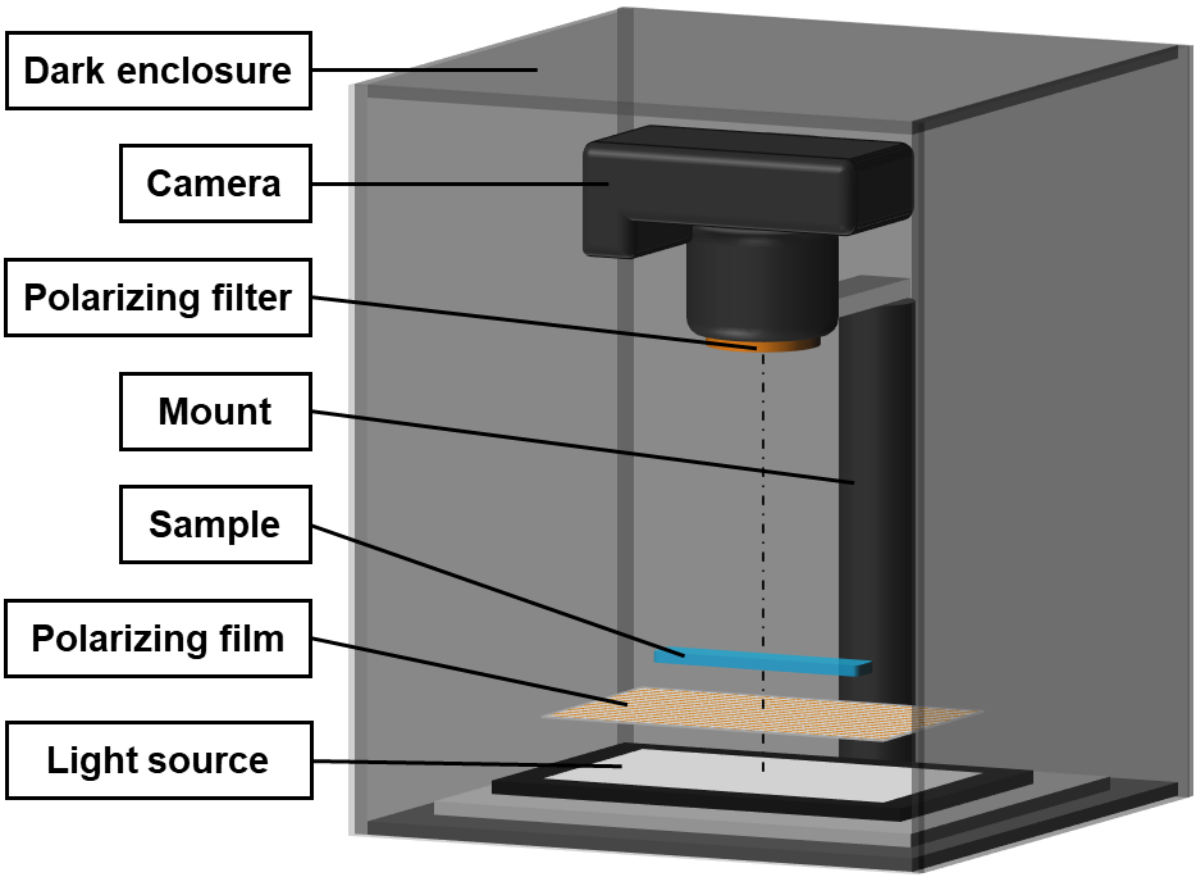

Figure 15: Custom-made polariscope used to measure the retardation.

Table 14: Camera and accessory information and settings used.

Camera	Nikon D90, Manual mode
Lens	Tamron SP 60 mm F/2 Macro
Filter	HOYA alpha CIR-PL 55 mm
F-stop	f/8
Exposure time (sec)	1/60
ISO speed	ISO-200
Light Temperature (K)	10,000

After generating the images with the custom-made polariscope, the photos were analyzed using image processing. First, Adobe Photoshop was used to crop and align the images and then OpenCV and Scikit Image were used to quantify the birefringence though the length of the impact bar parts. The image processing method is described in Figure 16.

(A) Michel-Lévy interference color chart [53]

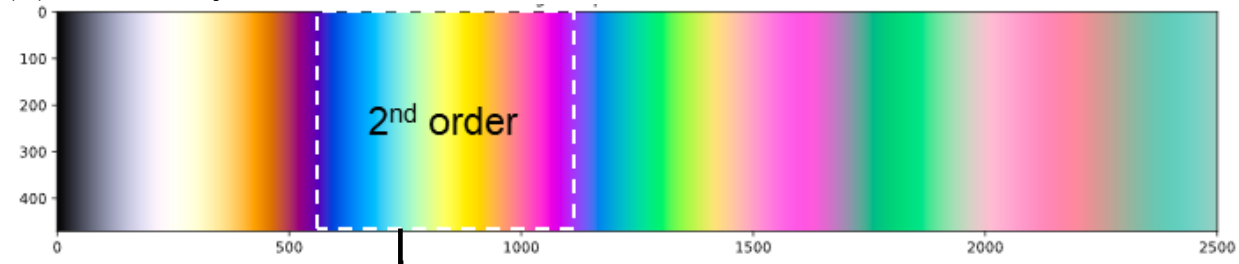

(B) Sample image **Chart insert**

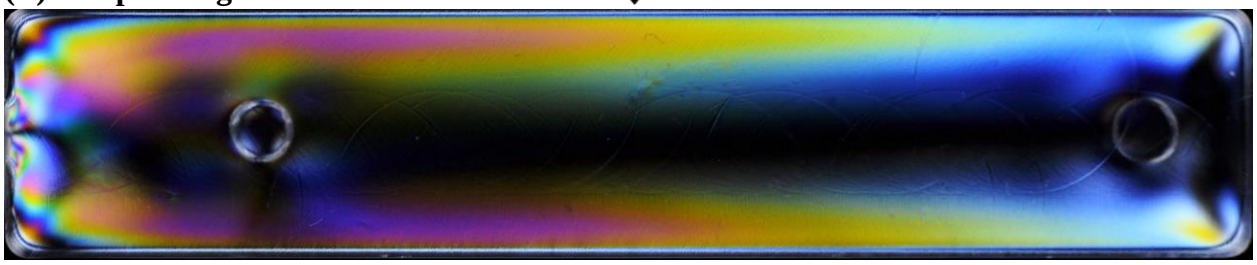

(C) Flow chart for determination of phase retardation

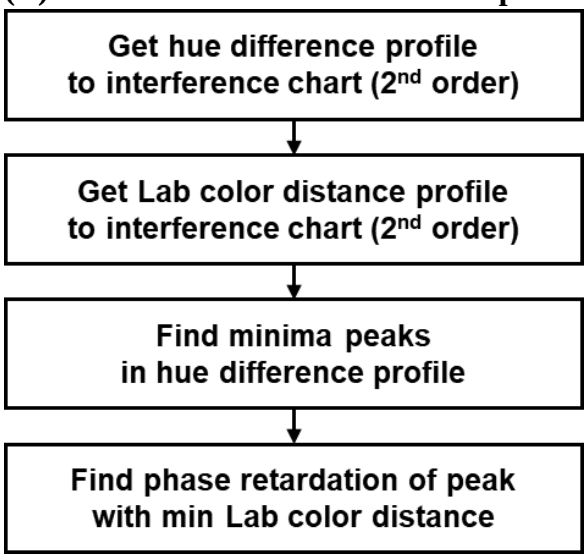

(D) Phase retardation measurement locations

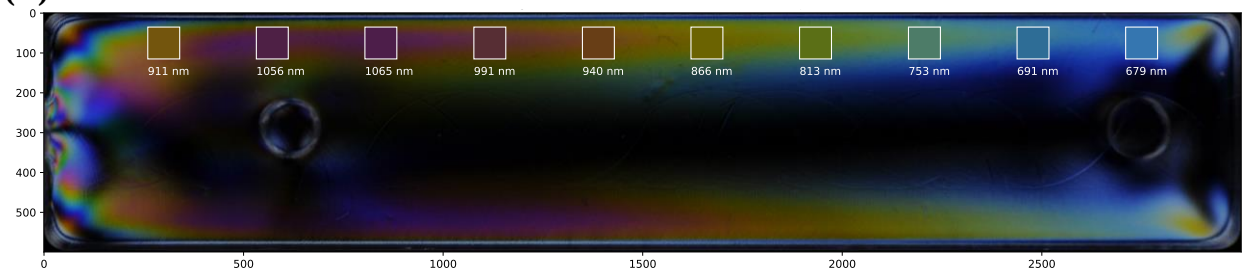

Figure 16: Retardation measurement process.

3. Results and Discussion

3.1 Simulations

3.1.1 Pressure

Figure 17 shows the sprue pressure versus time during the filling stage. The plot shows that when a mixer is used the pressure required during the injection-rate controlled filling stage is higher than the cases without a mixer. For the different mixer cases the highest pressure requirements were with the 1 mm helical mixer (Case 2) and the lowest pressure requirements were the 0.5 mm helical mixer and 1 mm built-in mixer cases. The no-mixer case with the circular runner geometry needed higher sprue pressure than the trapezoidal runner, which is likely due to the reduction of cross-sectional area when converting between the two runner cross-sections. In all cases the sprue pressure requirements were less than the 50 MPa packing pressure setting.

3.1.2 Temperature

Figure 18 shows the particle tracer results for the 1 mm helical mixer and 1 mm built in mixer cases. From this it can be seen how the mixer disrupts the thermal distribution within the runner and could be used to reduce issues like mold flow imbalance. Further, it graphically shows the functionality of the mixers. It should be noted that the mixers cause the particles to gather upstream of the mixers so there are fewer particles post-mixers than in the same mold regions in the no-mixer cases. Because of this it appears that the melt is hotter in the mixer cases, which is not the case. Table 15 shows the results at the end of filling and Table 16 shows the results at the end of packing. From this study's results and the results of our previous work [32], it is understood the thermal properties are made complex by the competing shear heating and conductive cooling occurring due to the combined restricted flow and increased runner and mixer surface area. For these runs, the average temperatures tend to be slightly less when a mixer is used than with the no-mixer cases, thus, it appears conductive cooling dominates. However, the changes are 3% lower or less, so the trend is not significant.

(A)

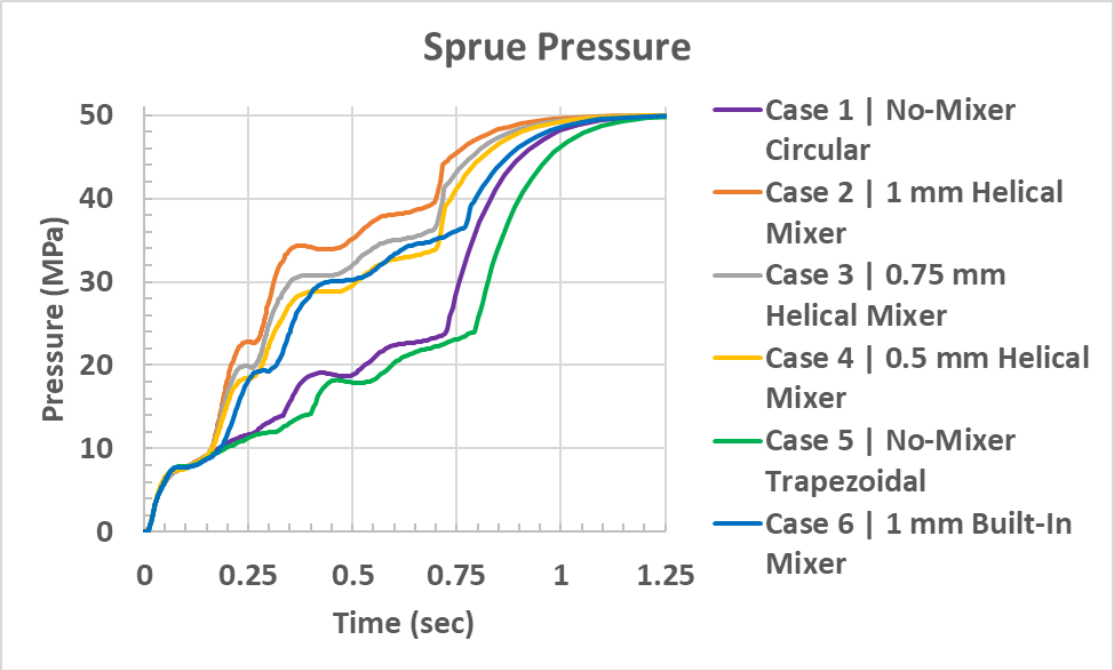

(B)

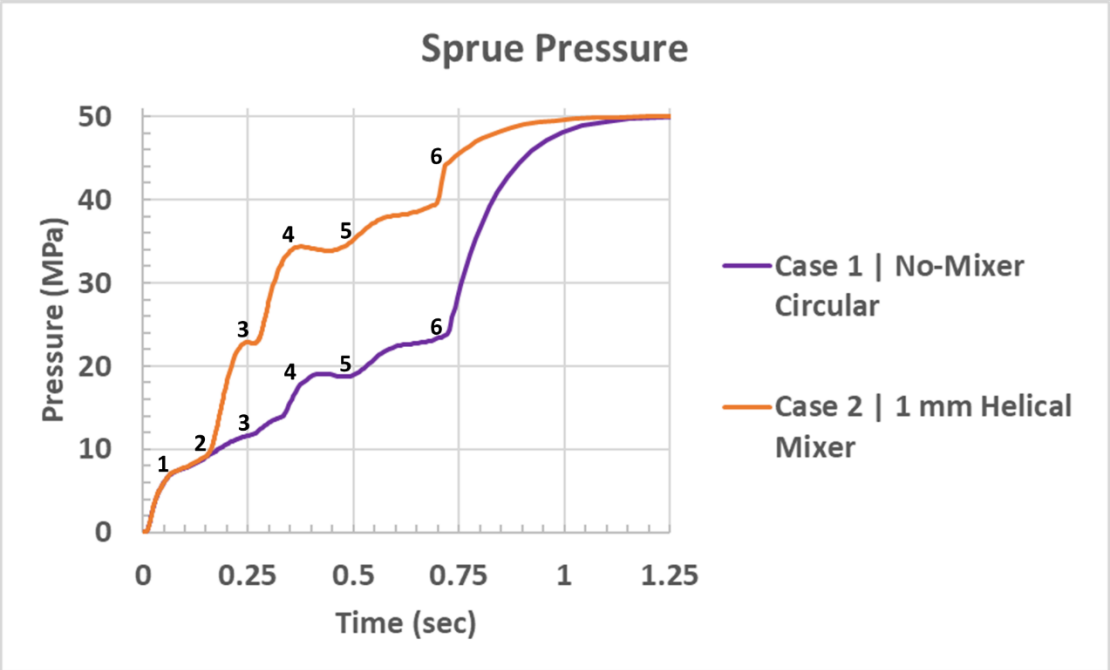

(1) Melt at end of mold sprue
(2) Melt reaches mixer
(3) Melt reaches corners of mold
(4) Melt reaches gates
(5) Melt reaches middle, narrow region of tensile bar part
(6) Melt fills mold

Figure 17: (A) Sprue pressure as a function of time where 0 sec is the start of the injection molding cycle. (B) Change of sprue pressure with respect to various filling stages.

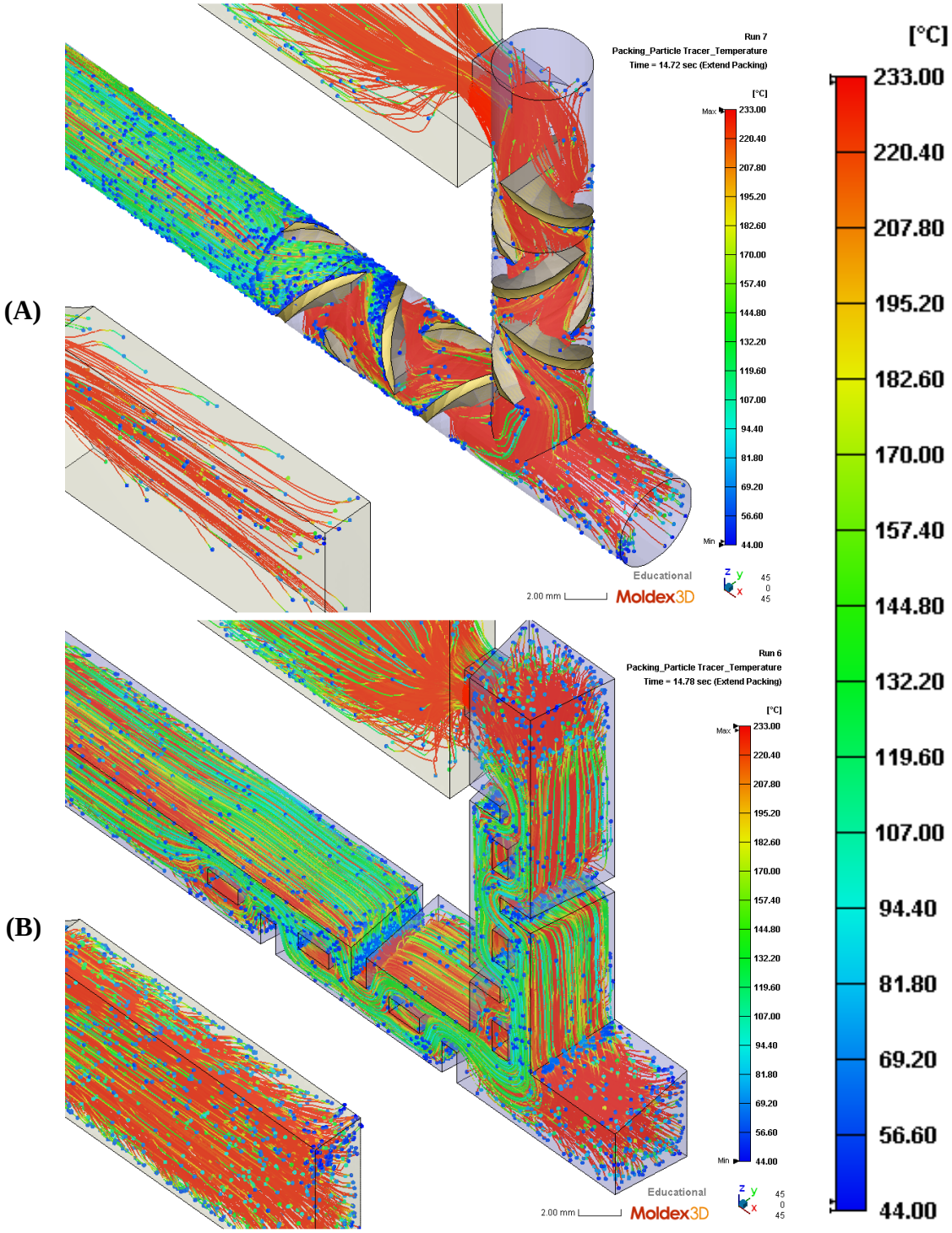
(A)
Run 7
Packing_Particle Tracer_Temperature
Time = 14.72 sec (Extend Packing)
[°C]
Max
233.00
220.40
207.80
195.20
182.60
170.00
157.40
144.80
132.20
119.60
107.00
94.40
81.80
69.20
56.60
Min
44.00
Educational
2.00 mm
Moldex3D
(B)
Run 6
Packing_Particle Tracer_Temperature
Time = 14.78 sec (Extend Packing)
[°C]
Max
233.00
220.40
207.80
195.20
182.60
170.00
157.40
144.80
132.20
119.60
107.00
94.40
81.80
69.20
56.60
Min
44.00
Educational
2.00 mm
Moldex3D
[°C]
233.00
220.40
207.80
195.20
182.60
170.00
157.40
144.80
132.20
119.60
107.00
94.40
81.80
69.20
56.60
44.00

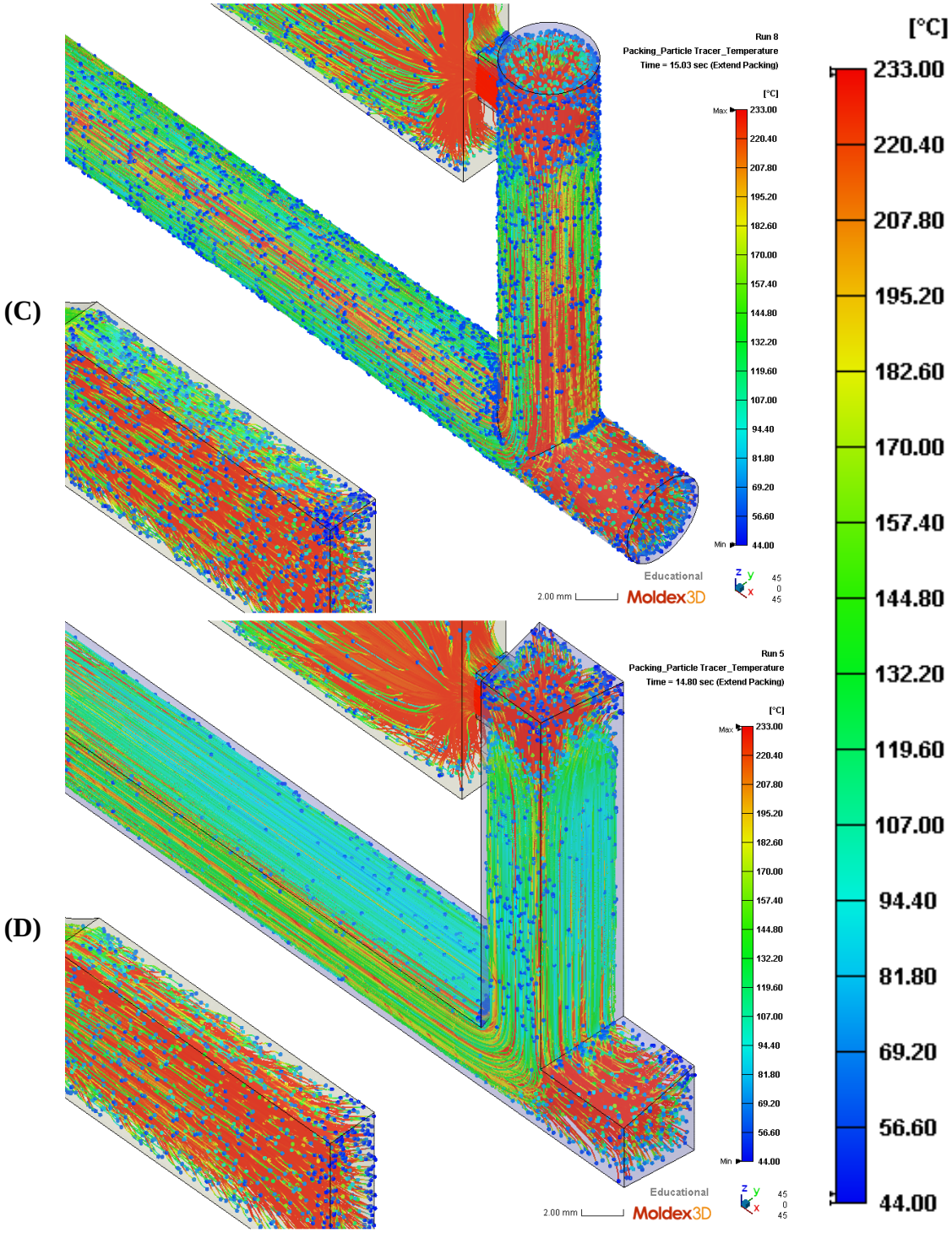

Figure 18: Particle tracer results of the temperature as the mold is filled (A) and (B) with the two 1 mm mixer geometries shown in Figure 3, (C) and (D) without mixers.

3.1.3 Shear Rate

Table 15 shows the results at the end of filling and Figure 19 shows the average maximum shear rate. As expected, the maximum shear rate experienced by the melt as it fills the mold, and in particular, flows though the runners, increases when a mixer is used. This means that the potential for shear heating and molecular damage due to the shear flow is higher with the mixers. The increase is most significant with the 1 mm helical mixer (Case 2), which shows a 35% increase in the average shear rate.

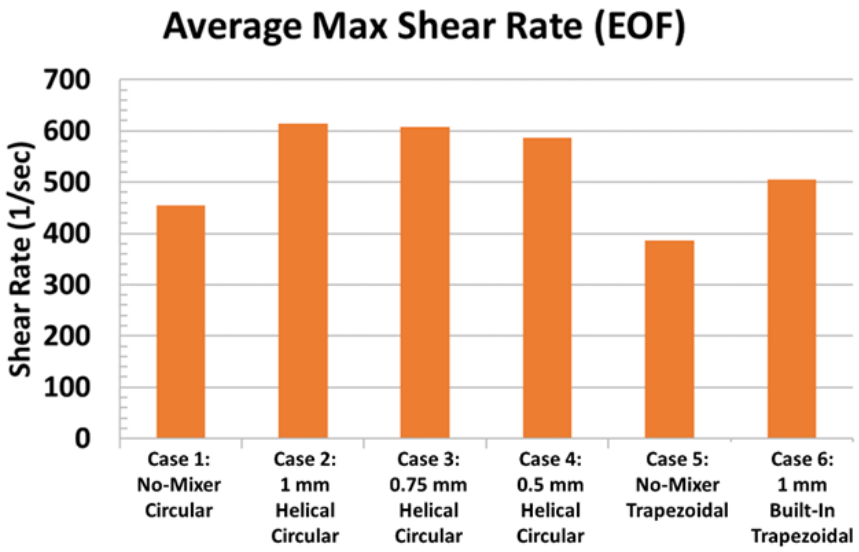

Figure 19: Average maximum shear rate through the parts as a function of geometry case.

3.1.4 Displacement, and Residual Stresses

Table 17 shows the average displacement and thermally induced residual stresses in the parts. There is little change in the displacement and residual stresses with or without the mixers. This is expected since these results are based on thermally induced warpage and as was shown in sub-section 3.1.2, there is little change for the average temperatures within the parts with or without the mixers.

3.1.5 Volumetric Shrinkage and Density

Table 16 shows simulated results at the end of the packing stage. Considering the volumetric shrinkage, density, and max volumetric shrinkage results, it can be seen that the mixer causes these results to stay the same or get slightly worse when compared to the no-mixer cases. The

most notable change is between the 1 mm helical mixer and no-mixer case where there is an increase in average volumetric shrinkage of 14%. The other mixer cases have less significant change.

3.1.6 Birefringence and Retardation

Table 18 summarizes the simulated optical results. Since retardation and birefringence are related to thickness and all the parts have the same geometry, the trends for both results are the same. Figure 20 shows the predicted flow-induced retardation, the thermal retardation, and the total retardation. It is clear that the flow-induced optical defect dominates when compared to the thermally induced defects due to the parts being thin with a high aspect ratio. It can also be seen that the thermally induced retardation does not change significantly between cases. The flow-induced retardation stays approximately constant or decreases slightly with the use of the static mixer. For the thicker (1.0 mm) mixers (Case 2 and Case 6) the improvement varies from 9 to 14%, respectively, when compared to the no-mixer cases (Case 1 and Case 5). Figure 21 shows the predicted flow-induced birefringence at the end of the filling stage (Figure 21A), at the end of the packing stage (Figure 21B), and at the end of the cooling stage (Figure 21C). This shows that the birefringence starts higher at the end of the filling stage, and it reduces through the packing stage and remains almost constant through the cooling stage. Figure 22 shows the representative flow-induced retardation pattern prediction through the impact bar part of Case 2, with a 1 mm helical mixer and circular runner. This pattern is similar for all parts simulated and shows the expected regions of high retardation near the gate and at the edges and lower retardation near the end of the part. Further, Figure 22 also shows the location of the measurement probes used to show the change in retardation through the part. Figure 23 shows that the absolute retardation is highest near the gate region and decreases towards the end of the part. The trapezoidal runner parts have lower retardation than the circular runner parts. The 1 mm built-in mixer has lower retardation near the gate reagion and then equal or a little higher retardation near the end of the part (cf. Figure 23B). The 1 mm helical mixer has the lowest retardation at each position when comparing the circular runners (cf. Figure 23A).

Table 15: Simulation results at the end of the filling stage.

Filling														
Description		**Unit**	**Impact**	**Tensile**	**Impact**	**Tensile**	**Impact**	**Tensile**	**Impact**	**Tensile**	**Impact**	**Tensile**	**Impact**	**Tensile**
			No-Mixer Circular		**1 mm Helical Mixer**		**0.75 mm Helical Mixer**		**0.5 mm Helical Mixer**		**No-Mixer Trapezoidal**		**1 mm Built-In Mixer**	
			Case 1		**Case 2**		**Case 3**		**Case 4**		**Case 5**		**Case 6**	
Temperature	Avg	°C	208	203	206	200	206	200	206	201	207	203	205	203
	Standard Deviation	°C	45.0	49.2	45.0	48.6	44.7	48.4	44.8	48.7	46.0	49.7	47.1	47.7
Max Shear Rate	Avg	1/sec	455		613		607		587		386		506	
	Standard Deviation	1/sec	496		714		683		638		436		510	
Flow Induced Residual Stress Max Principal Stress Total	Avg	MPa	1.41E-01	9.01E-02	1.46E-01	7.71E-02	1.49E-01	7.90E-02	1.48E-01	7.62E-02	8.73E-02	1.36E-01	1.38E-01	7.54E-02
	Standard Deviation	MPa	8.75E-02	7.23E-02	9.02E-02	6.24E-02	9.61E-02	6.92E-02	9.55E-02	6.74E-02	5.19E-02	7.15E-02	6.80E-02	4.67E-02
Flow Induced Residual Stress Max Shear Stress	Avg	MPa	8.99E-02	5.77E-02	9.32E-02	4.91E-02	9.50E-02	4.99E-02	9.45E-02	4.83E-02	5.68E-02	8.67E-02	8.90E-02	4.87E-02
	Standard Deviation	MPa	4.93E-02	3.95E-02	5.12E-02	3.39E-02	5.42E-02	3.74E-02	5.39E-02	3.64E-02	3.00E-02	4.09E-02	3.99E-02	2.59E-02

Table 16: Simulation results at the end of the packing stage.

Packing														
Description		**Unit**	**Impact**	**Tensile**	**Impact**	**Tensile**	**Impact**	**Tensile**	**Impact**	**Tensile**	**Impact**	**Tensile**	**Impact**	**Tensile**
			No-Mixer Circular		**1 mm Helical Mixer**		**0.75 mm Helical Mixer**		**0.5 mm Helical Mixer**		**No-Mixer Trapezoidal**		**1 mm Built-In Mixer**	
			Case 1		**Case 2**		**Case 3**		**Case 4**		**Case 5**		**Case 6**	
Temperature	Avg	°C	156	148	155	145	153	144	154	145	156	148	155	147
	Standard Deviation	°C	53.2	54.3	52.6	53.3	52.4	52.9	52.6	53.2	53.1	54.1	53.0	53.3
Volumetric Shrinkage	Avg	%	2.90	2.63	3.41	3.06	3.19	2.85	3.08	2.75	2.89	2.62	3.23	2.90
	Standard Deviation	%	1.87	1.85	2.01	1.96	1.94	1.88	1.90	1.86	1.87	1.84	1.95	1.92
Density	Avg	g/cc	1.02	1.02	1.01	1.02	1.01	1.02	1.02	1.02	1.02	1.02	1.01	1.02
	Standard Deviation	g/cc	2.20E-02	2.21E-02	2.32E-02	2.30E-02	2.26E-02	2.23E-02	2.23E-02	2.21E-02	2.19E-02	2.20E-02	2.27E-02	2.25E-02
Max Volume Shrinkage	Avg	%	4.65	4.33	5.28	4.86	5.01	4.59	4.87	4.47	4.67	4.36	5.09	4.69
	Standard Deviation	%	1.05	1.15	1.09	1.18	1.10	1.19	1.08	1.18	0.98	1.08	0.981	1.13
Flow Induced Residual Stress Max Principal Stress Total	Avg	MPa	4.06E-02	5.19E-02	3.58E-02	4.70E-02	4.13E-02	5.09E-02	4.16E-02	5.04E-02	3.94E-02	5.08E-02	3.44E-02	4.49E-02
	Standard Deviation	MPa	7.76E-02	8.60E-02	7.08E-02	7.43E-02	8.23E-02	8.19E-02	8.13E-02	8.01E-02	6.36E-02	7.17E-02	5.35E-02	6.16E-02
Flow Induced Residual Stress Max Shear Stress	Avg	MPa	2.45E-02	3.04E-02	2.18E-02	2.79E-02	2.48E-02	3.00E-02	2.50E-02	2.97E-02	2.36E-02	2.99E-02	2.10E-02	2.67E-02
	Standard Deviation	MPa	4.27E-02	4.68E-02	3.92E-02	4.09E-02	4.54E-02	4.48E-02	4.48E-02	4.39E-02	3.50E-02	3.93E-02	2.99E-02	3.40E-02

Table 17: Simulation results considering thermally induced displacement and residual stresses.

Warpage														
Description		**Unit**	**Impact**	**Tensile**	**Impact**	**Tensile**	**Impact**	**Tensile**	**Impact**	**Tensile**	**Impact**	**Tensile**	**Impact**	**Tensile**
			No-Mixer Circular		**1 mm Helical Mixer**		**0.75 mm Helical Mixer**		**0.5 mm Helical Mixer**		**No-Mixer Trapezoidal**		**1 mm Built-In Mixer**	
			Case 1		**Case 2**		**Case 3**		**Case 4**		**Case 5**		**Case 6**	
Total Displacement	Avg	mm	7.76E-02	7.73E-02	7.82E-02	7.84E-02	7.71E-02	7.69E-02	7.71E-02	7.70E-02	7.70E-02	7.75E-02	7.69E-02	7.71E-02
	Standard Deviation	mm	3.90E-02	3.47E-02	3.93E-02	3.51E-02	3.88E-02	3.45E-02	3.88E-02	3.46E-02	3.88E-02	3.46E-02	3.87E-02	3.45E-02
Thermally Induced Residual Von Mises Stress	Avg	MPa	1.06	1.36	1.04	1.36	1.03	1.34	1.03	1.34	0.99	1.30	1.00	1.31
	Standard Deviation	MPa	0.614	0.672	0.611	0.679	0.602	0.664	0.601	0.665	0.582	0.647	0.580	0.649

Table 18: Simulation results of the optical properties of the parts.

Optics														
Description		**Unit**	**Impact**	**Tensile**	**Impact**	**Tensile**	**Impact**	**Tensile**	**Impact**	**Tensile**	**Impact**	**Tensile**	**Impact**	**Tensile**
			No-Mixer Circular		**1 mm Helical Mixer**		**0.75 mm Helical Mixer**		**0.5 mm Helical Mixer**		**No-Mixer Trapezoidal**		**1 mm Built-In Mixer**	
			Case 1		**Case 2**		**Case 3**		**Case 4**		**Case 5**		**Case 6**	
Flow Induced Birefringence In Filling Stage	Avg	-	-6.28E-04	-4.48E-04	-6.50E-04	-3.86E-04	-6.69E-04	-3.95E-04	-6.64E-04	-3.82E-04	-4.01E-04	-6.56E-04	-6.13E-04	-3.74E-04
	Standard Deviation	-	4.02E-04	3.46E-04	4.15E-04	3.00E-04	4.42E-04	3.31E-04	4.38E-04	3.22E-04	2.41E-04	3.56E-04	3.07E-04	2.33E-04
Flow Induced Birefringence In Packing Stage	Avg	-	-1.84E-04	-2.50E-04	-1.60E-04	-2.25E-04	-1.86E-04	-2.44E-04	-1.88E-04	-2.42E-04	-1.80E-04	-2.45E-04	-1.53E-04	-2.16E-04
	Standard Deviation	-	3.66E-04	4.16E-04	3.32E-04	3.56E-04	3.87E-04	3.93E-04	3.83E-04	3.85E-04	3.02E-04	3.51E-04	2.49E-04	3.00E-04
Flow Induced Birefringence In Cooling Stage	Avg	-	-1.62E-04	-2.21E-04	-1.42E-04	-1.97E-04	-1.65E-04	-2.13E-04	-1.65E-04	-2.09E-04	-1.58E-04	-2.13E-04	-1.35E-04	-1.87E-04
	Standard Deviation	-	3.67E-04	4.19E-04	3.33E-04	3.59E-04	3.88E-04	3.96E-04	3.84E-04	3.88E-04	3.04E-04	3.55E-04	2.51E-04	3.04E-04
Flow Induced Retardation	Avg	nm	-561	-900	-501	-815	-568	-865	-570	-852	-555	-952	-479	-861
	Standard Deviation	nm	376	785	362	676	407	716	397	712	351	947	299	797
Thermally Induced Birefringence	Avg	-	4.69E-06	6.56E-06	4.59E-06	6.51E-06	4.60E-06	6.47E-06	4.58E-06	6.45E-06	4.51E-06	6.36E-06	4.48E-06	6.42E-06
	Standard Deviation	-	4.46E-06	5.03E-06	4.43E-06	5.06E-06	4.39E-06	4.97E-06	4.38E-06	4.97E-06	4.34E-06	4.95E-06	4.21E-06	5.11E-06
Thermally Induced Retardation	Avg	nm	22.2	30.4	21.8	30.4	21.8	30.0	21.7	29.9	21.5	29.7	20.9	30.6
	Standard Deviation	nm	17.6	18.6	17.5	18.9	17.3	18.4	17.3	18.4	17.2	18.5	16.0	19.7
Total Birefringence	Avg	-	-1.58E-04	-2.15E-04	-1.37E-04	-1.90E-04	-1.61E-04	-2.07E-04	-1.60E-04	-2.03E-04	-1.54E-04	-2.06E-04	-1.30E-04	-1.81E-04
	Standard Deviation	-	3.66E-04	4.17E-04	3.32E-04	3.58E-04	3.87E-04	3.94E-04	3.83E-04	3.87E-04	3.04E-04	3.54E-04	2.50E-04	3.02E-04
Total Retardation	Avg	nm	-539	-870	-480	-784	-546	-835	-549	-822	-533	-923	-458	-831
	Standard Deviation	nm	371	774	357	664	403	705	392	701	345	935	292	783

(A)

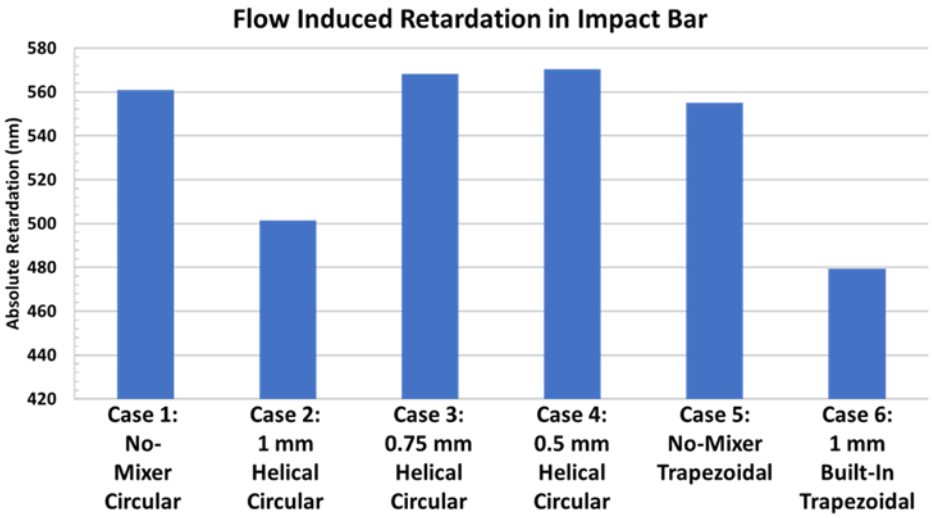

(B)

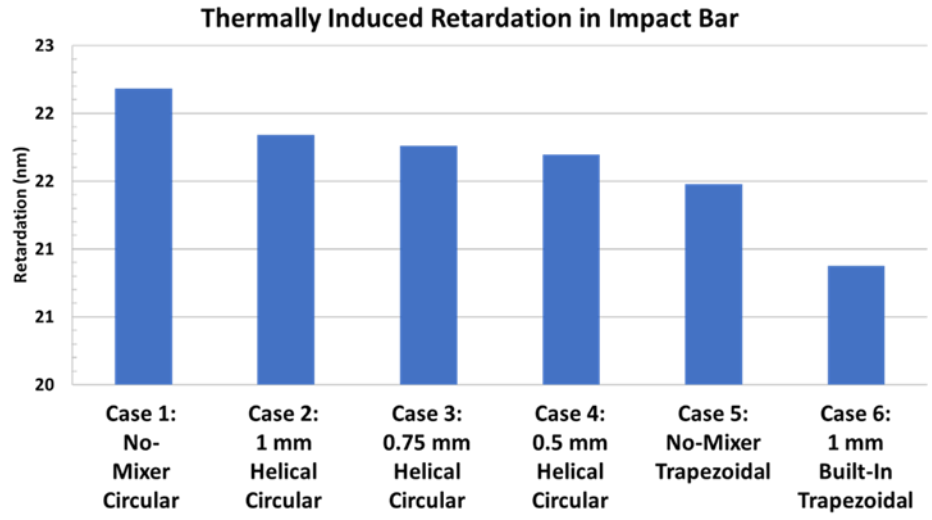

(C)

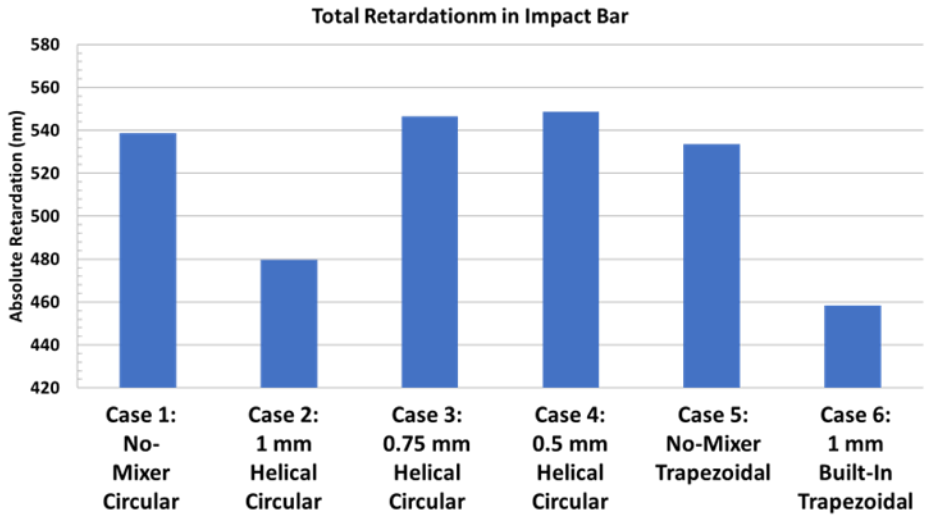

Figure 20: The numerically predicted retardation through the impact bar parts as a function of geometry case.

(A)

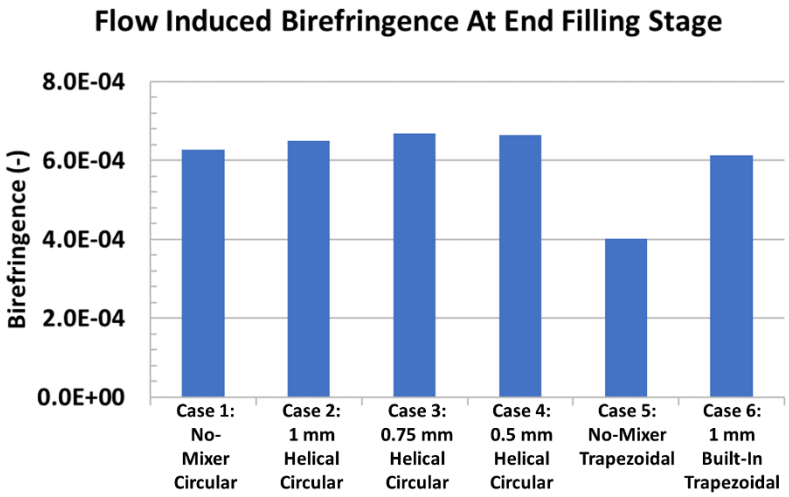

(B)

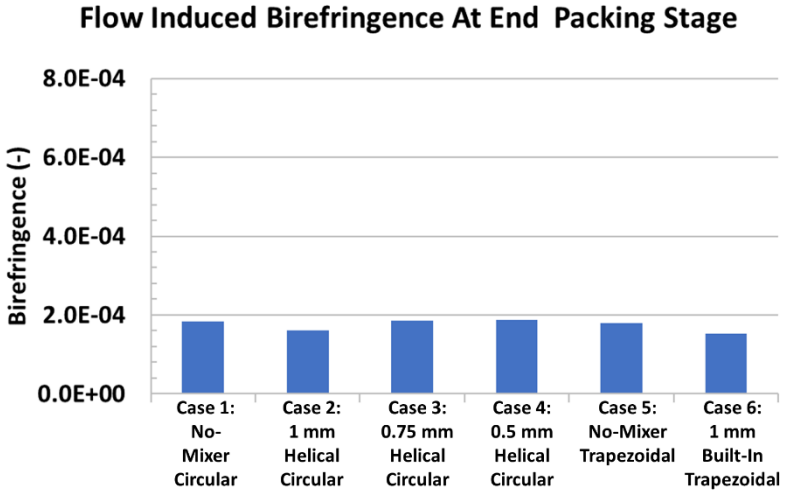

(C)

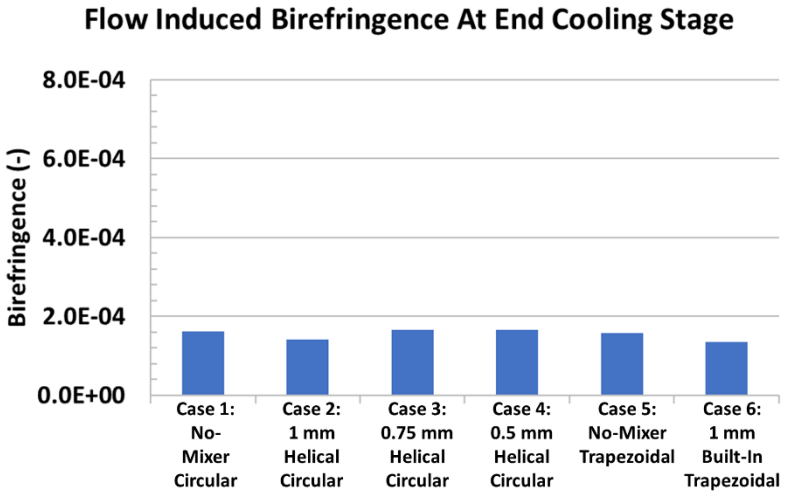

Figure 21: The numerically predicted flow-indued birefringence through the impact bar parts as a function of geometry case.

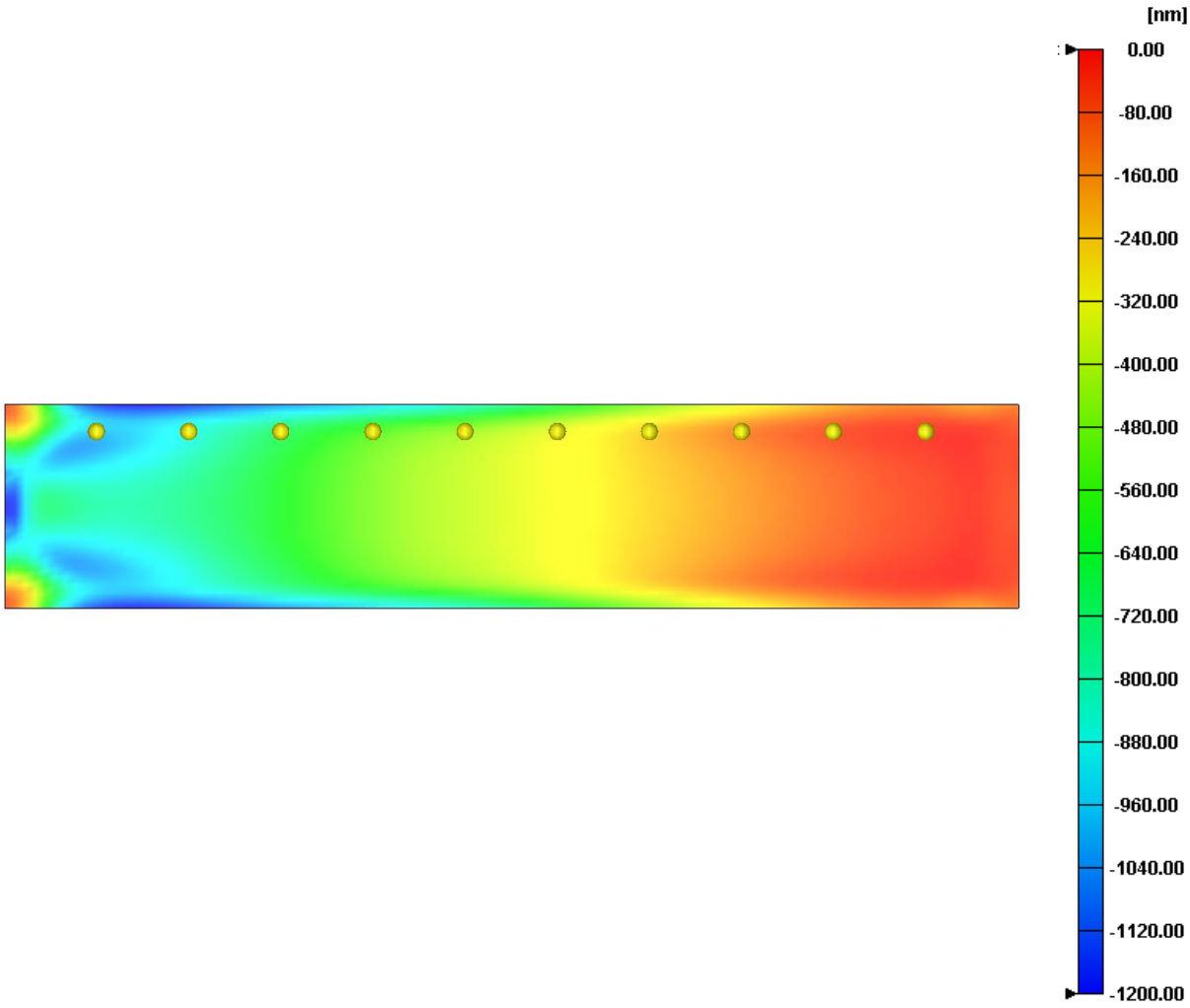

Figure 22: Predicted flow-induced retardation pattern for the impact bar part of Case 2, circular runner with 1 mm helical mixer. The yellow dots show the location of retardation measurements shown in Figure 23.

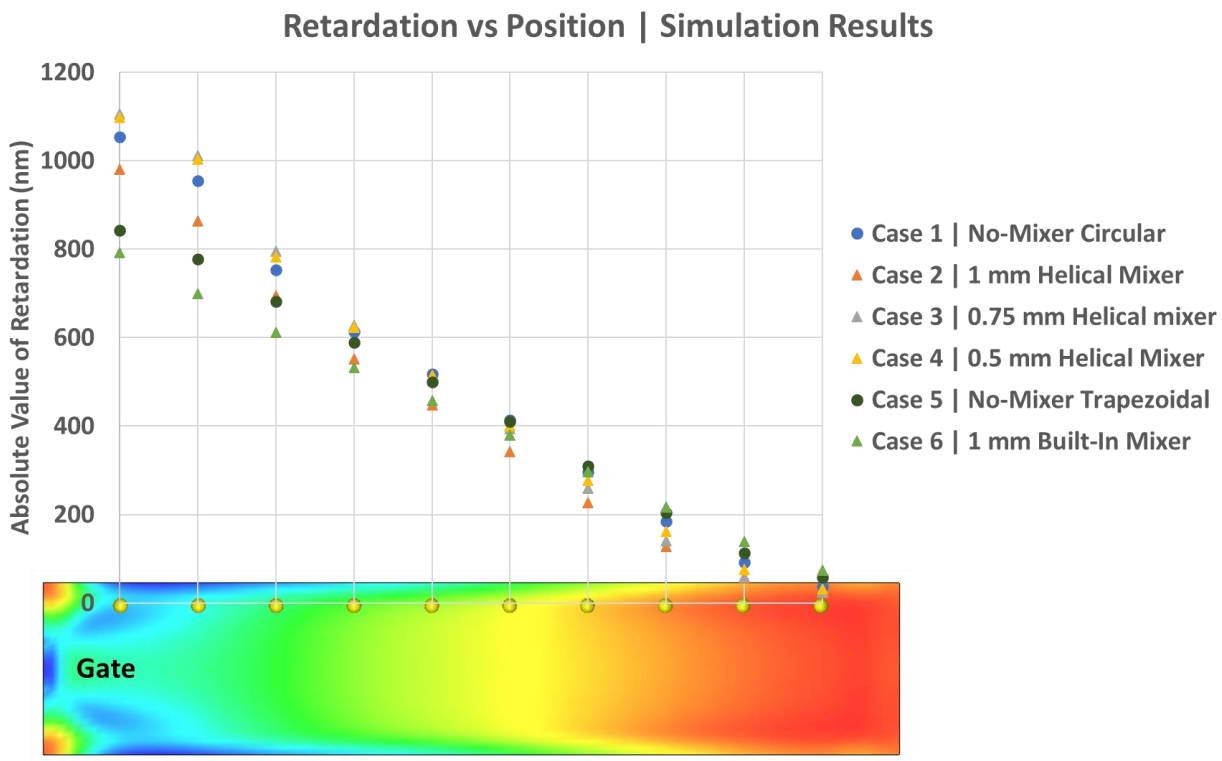

Figure 23: Retardation vs position along the impact bar part in the simulation results.

3.2 Experimental Optical Quality

Figure 24 shows the average retardation versus position for the molded samples with the no-mixer case (Figure 24A), the 1 mm helical mixer case (Figure 24B), and the no-mixer no-packing case (Figure 24C). These plots show that there is good repeatability in the retardation measurements within the injection molding run and between runs.

Figure 25 shows the averaged results for each of the molded cases. The 1 mm mixer case showed the largest retardation for each position. The second highest retardation was the 0.5 mm case. The built-in mixer cases both showed slightly lower retardation than the no-mixer case, and the no-mixer, no-packing case showed the lowest retardation value. The retardation had the most significant variation in the regions near the gate. Far from the gate, the retardation did not vary significantly between all the cases evaluated. The most notable change in the retardation value occurred between the no-mixer no-packing case and the rest of the cases. This shows that the packing stage plays a particularly significant role in dictating the retardation of the molded parts. The changes in the retardation values between the other cases does not appear to be statistically significant.

These results overall match the predicted flow-induced retardation pattern shown in Figure 22 with higher retardation near the gate and lower at the end of the part. However, the experimental trends do not match the simulations exactly. For the mixer versus no-mixer cases it could be that the measurement technique does not have high enough resolution to see the same trends as the simulations or due to differences in the experiments such as injection pin locations on the parts or other factors such as resin difference, mixer material differences, and mold surface roughness that are not captured completely within the simulations.

(A)

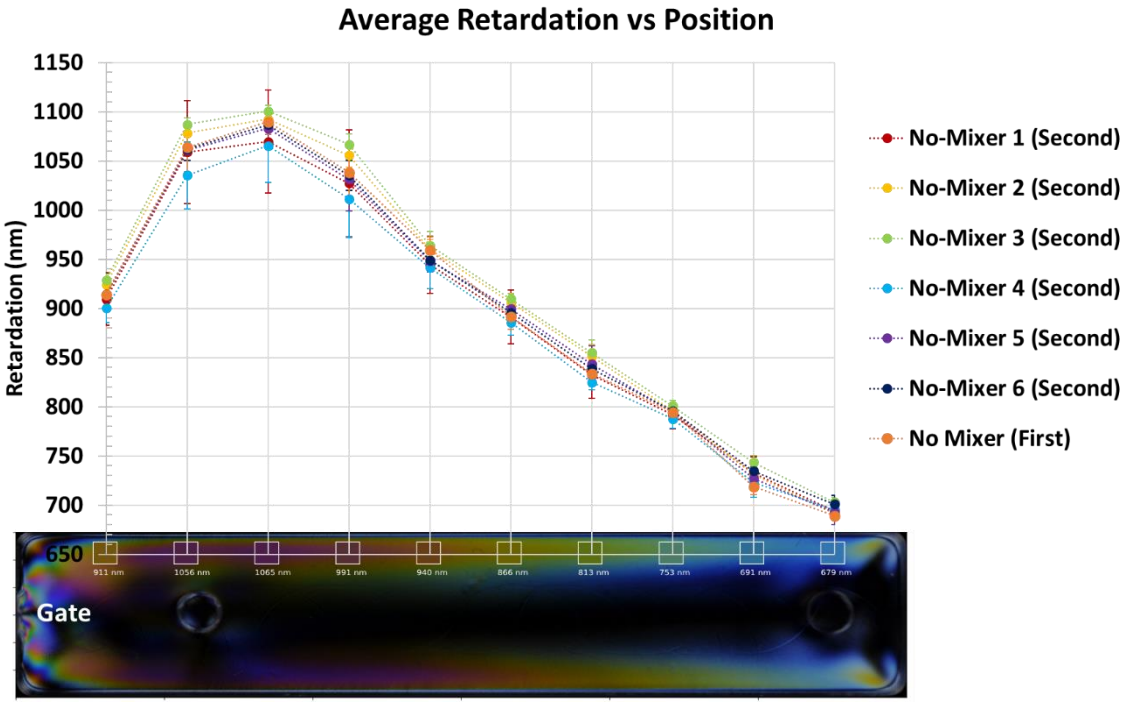

(B)

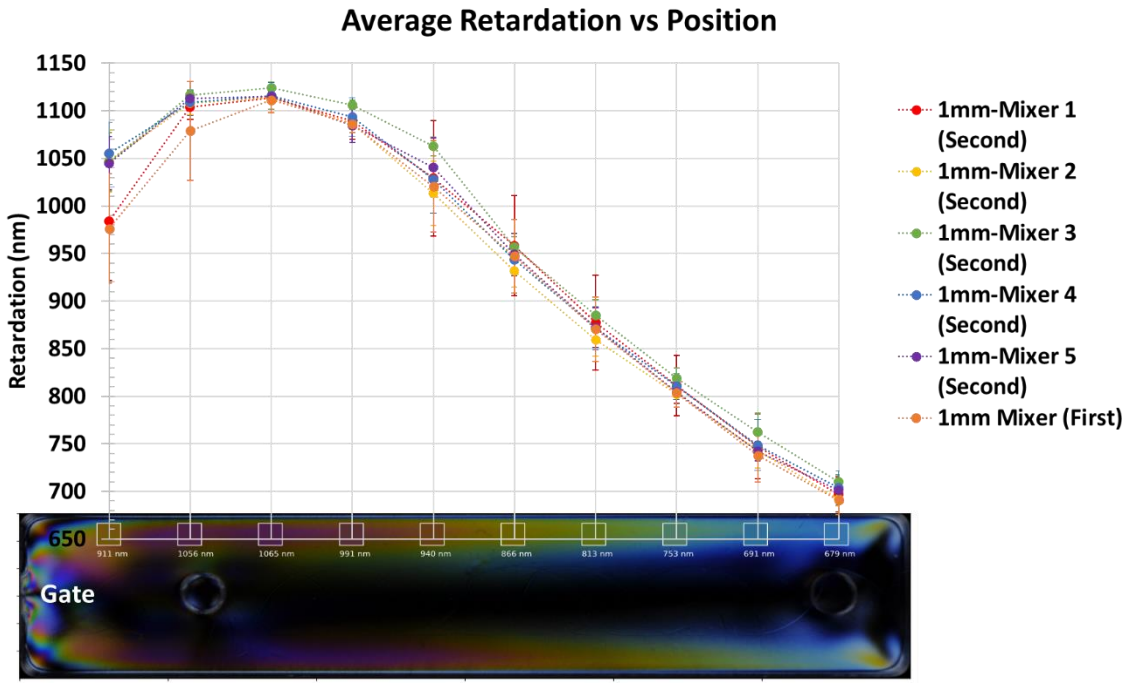

(C)

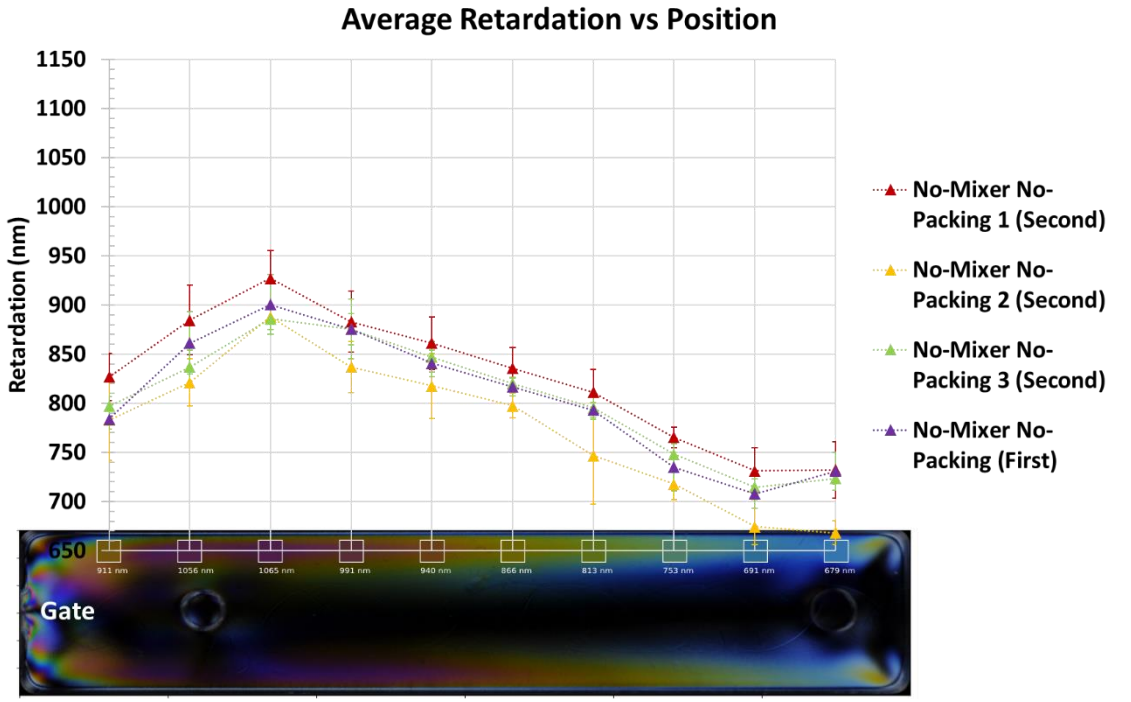

Figure 24: The average retardation versus the position on the molded samples. Position 1 is closest to the gate. Each data point represents the average of five or more samples taken continuously during one of the two injection molding runs. The error bars show the standard deviation of the sample group.

(A)

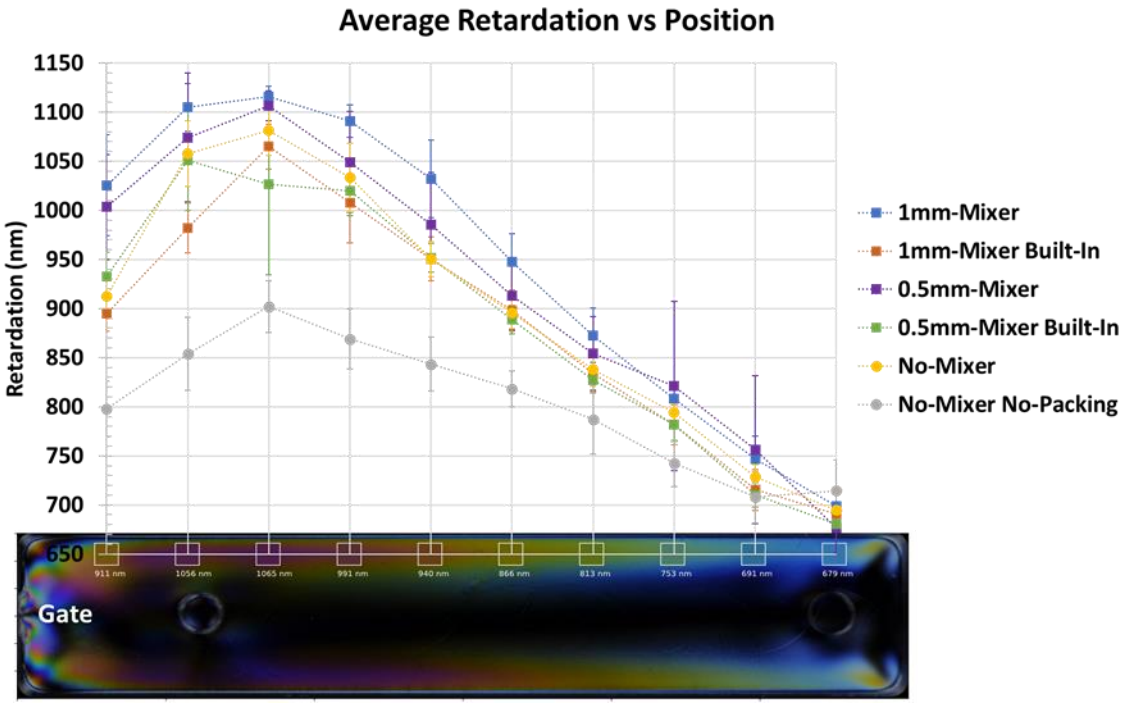

(B)

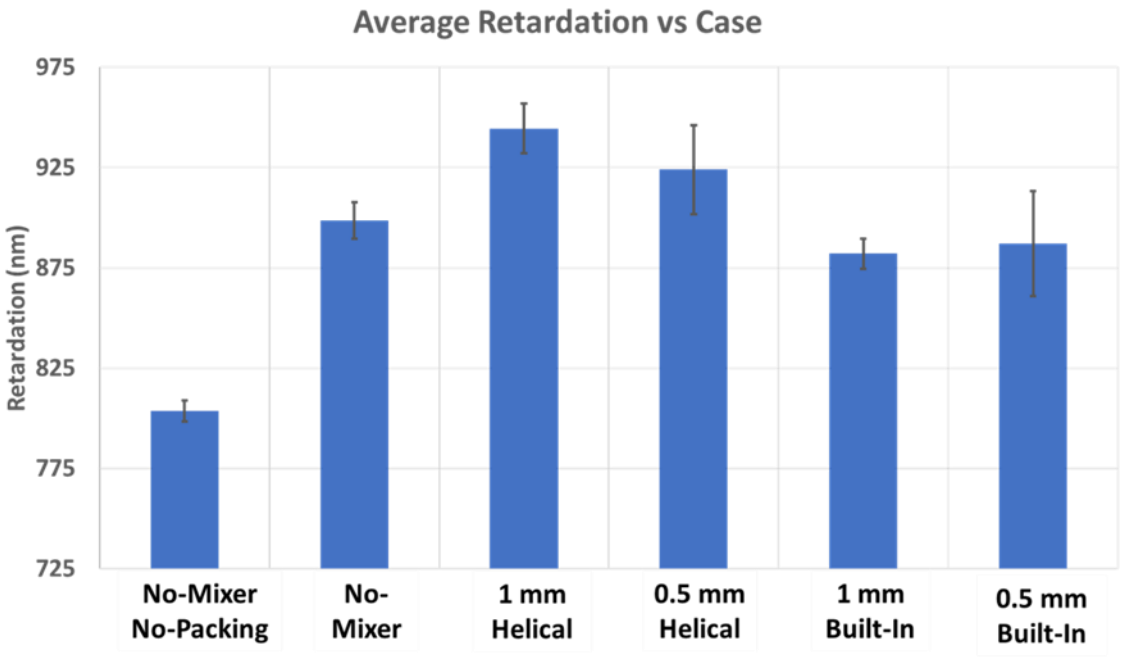

Figure 25: The average retardation versus (A) the position on the molded samples and (B) the case. Position 1 is closest to the gate. Each data point represents the average of all samples taken for that particular geometry case. The error bars show the standard deviation of the case.

4. Conclusion

The use of a static mixer within the runner system in an injection mold with polystyrene (PS) materials was explored with simulations and molding experiments. It was found that the mixers had the expected result of increasing machine injection pressure requirements during the injection stage due to the restriction of flow area in the runners. The mixers also increased the shear rate when a fixed flow rate was used. For the general quality variables of volumetric shrinkage and density at the end of packing, the mixers appeared to cause increased shrinkage and decreased density, but the change was small. The mixer had a slight effect on the optical property of retardation, which is shown both in simulations and the molding experiments. In the simulations the thicker, 1 mm helical and built-in mixer cases (Cases 2 and 6) showed some improvements for the flow-induced optical properties. However, in the experiments the built-in mixers showed improvements in the retardation and the helical mixers showed that they caused the retardation to increase slightly. All the cases yielded similar retardation values except the no-mixer, no-packing case, suggesting the importance of the packing stage on the part retardation. In summary, the use of a static mixer shows potential in allowing for mixing after the plasticizing unit, but its impact in the optical properties in the final molded parts appears to be slight. Nonetheless, the mixers could still be used for post-plasticizing unit mixing to alleviate issues such as mold-flow imbalance without affecting the final part properties.

Chapter 3: Effect of Sacrificial Reservoir Runner Geometry on Optical Properties of Plastic Injection Molded Parts

1. Introduction

Improving the quality and accuracy of injection molded parts has been an objective since the injection molding machine was developed in the nineteenth century [35]. Polymers, and their ability to be molded into an infinite number of shapes, allow for the manufacture of one of the original plastic products like billiard balls, to complex precision parts such as micro-camera lenses. In the optical field, the use of polymers versus traditional glass is highly desirable; polymers can be easily manufactured into complex shapes, which are lightweight and readily mass-produced via injection molding and other methods [36]. About a hundred years after the first injection molding machines the materials and process had advanced sufficiently to allow for the manufacture of precision plastic lenses with qualities that competed with their glass counterparts [37, 38]. This advancement can be credited to several sources, including the development of optical polymers, the improvement of injection molding machines and machine control, the increased understanding of viscoelasticity and rheology of polymers, and the high-quality standards of the injection molding machine mold. However, there is a limit to the quality improvements that can be obtained in the standard injection molding process due to the inherent properties of the molecular structure of polymers, which cause either geometric or birefringence defects as shown in Figure 26 [39]. To overcome these material and process shortcomings, many novel approaches are pursued to further improve the quality of plastic optic parts. This work explores the approach of adding a sacrificial reservoir to the mold to improve part quality for optical applications.

To aid in the manufacture of high-quality polymer optical components, several novel approaches have been developed. These include process modifications, mold modifications, or combinations of the two. Injection-compression molding, for example, requires specialty molds, which can provide compression action on the part, thus replacing the packing stage in the injection molding cycle [35, 40]. In this way both the injection molding process and mold are modified. Other novel approaches used for plastic optics include rapid heat cycle molding (RHCM) [39], conformal cooling systems [41], micro-injection molding [35], process

optimization and/or defect compensation via simulation [42, 43, 44, 45, 46, 47, 48], multi-shot molding [43], and runner modifications to improve melt homogenization [31, 49].

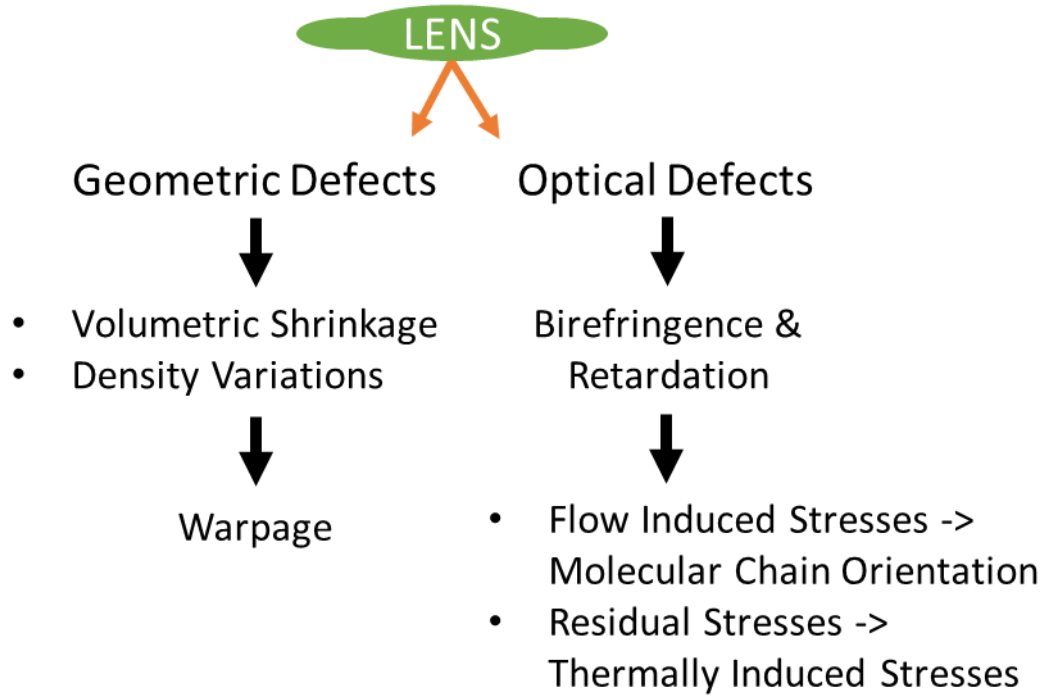

Figure 26: The as-molded defects that occur within an injection molded lens.

In the injection molding process, the filling of the mold is mostly controlled by the melt flow rate or the speed of the injection screw as it pushes the polymer melt into the mold [35]. This correspondingly controls the melt-front velocity (MFV), or the speed of the polymer melt front as it travels into the mold [39]. For high-precision parts such as optical lenses, it is desired for the MFV to be held constant while the part cavity in the mold is filled [39]. This reduces the development of surface profile defects and improves optical properties by decreasing density variations through the part and preventing strong or non-uniform molecular orientation, which can lead to anisotropy, warpage, and birefringence [35]. For large, simple geometries, constant MFV can be achieved though flow control by the injection molding machine [39]. However, for small components with complex geometries such as optical lenses, this is very challenging and frequently impossible. The reservoir mold modification is a sacrificial mold cavity included on a separate branch of a multi-component mold; a sketch of a possible implementation is shown in

Figure 27. The principal idea behind this design is that MFV in one branch can be controlled by changing the geometry in another branch, since the melt will want to flow in the direction of least resistance. Thus, the first goal of the reservoir mold modification is to provide MFV control for the filling of the part cavities.

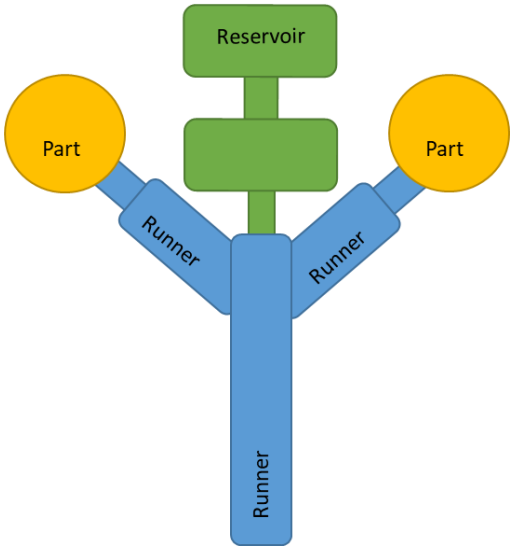

Figure 27: A possible implementation of a mold reservoir which controls the melt flow of two symmetrically placed parts.

Near the end of filling the mold, the injection molding machine control switches from flow control to pressure control (F/P switch-over) [35]. This provides protection from pressure spikes for the machine and prevents defects like flashing from occurring on the part [35]. In a traditional mold the final portion to be filled is at the end of the part. Thus, there is a change in MFV near the end of filling the part. This leads to the development of variable molecular orientation within the part and therefore, shrinkage variation (warpage) and birefringence defects [39]. Since molds are typically oriented so the part cavity is the last geometry filled, these defects occur within the part geometry. However, if there is still volume to be filled in a sacrificial reservoir, the part cavity can be filled completely prior to the F/P switch over. The second goal of the reservoir mold modification is to act as a "damping cushion" to reduce pressure and melt velocity changes at the F/P switch over from negatively affecting the part quality.

The concept of using the runner system as a means of flow control has been previously studied with regard to artificially balancing unbalanced multi-cavity molds [54, 55, 56, 57, 58].

During the early days of injection molding simulations, Wang et. al. developed a program for runner design [54]. The algorithm driving this program started with isothermal and power-law assumptions and using the balance laws determined relations between unbalanced runners by holding the pressure drop between channels as equal and relating the volumetric flow rates between channels [54]. In this way the researchers were able to specify flow restrictors for runners, which would result in the target part cavities to fill at the same time [54]. The authors also took into consideration the thermal effects that were overlooked by their assumptions, by doing an iterative correction process [54]. Work on artificially balancing unbalanced molds continued into the 90s with improved algorithms, which took into account thermal effects, runner geometries that are not round, other flow phenomena, and more advanced iterative optimization techniques [55, 56, 57, 58]. All the methods worked off from the power-law assumption and started with the fundamental balance laws.

The goal of this project is to develop a method for designing an effective mold reservoir, which can provide, for the part cavity, flow control, F/P switch over point damping, and complete material packing. This method will be based on engineering intuition and the use of the fundamental balance laws and the power-law constitutive equation and will be verified using commercial injection molding simulation software Moldex3D.

2. Method

As is described in Figure 28, the aim in adding a reservoir cavity is to:

- Slow down the flow rate as the melt reaches and enters the lens gate.
- Provide flow control to ensure that the lens is completely filled and packed with a near constant melt front velocity.
- Minimize the transition effect of filling to packing switch-over point (SOP).

To achieve this, the cross-sectional area of the reservoir is varied to compensate for the changing cross-sectional area of the lens gate and lens geometry, and to control the melt front velocity so that it is constant through the filling of the lens cavity.

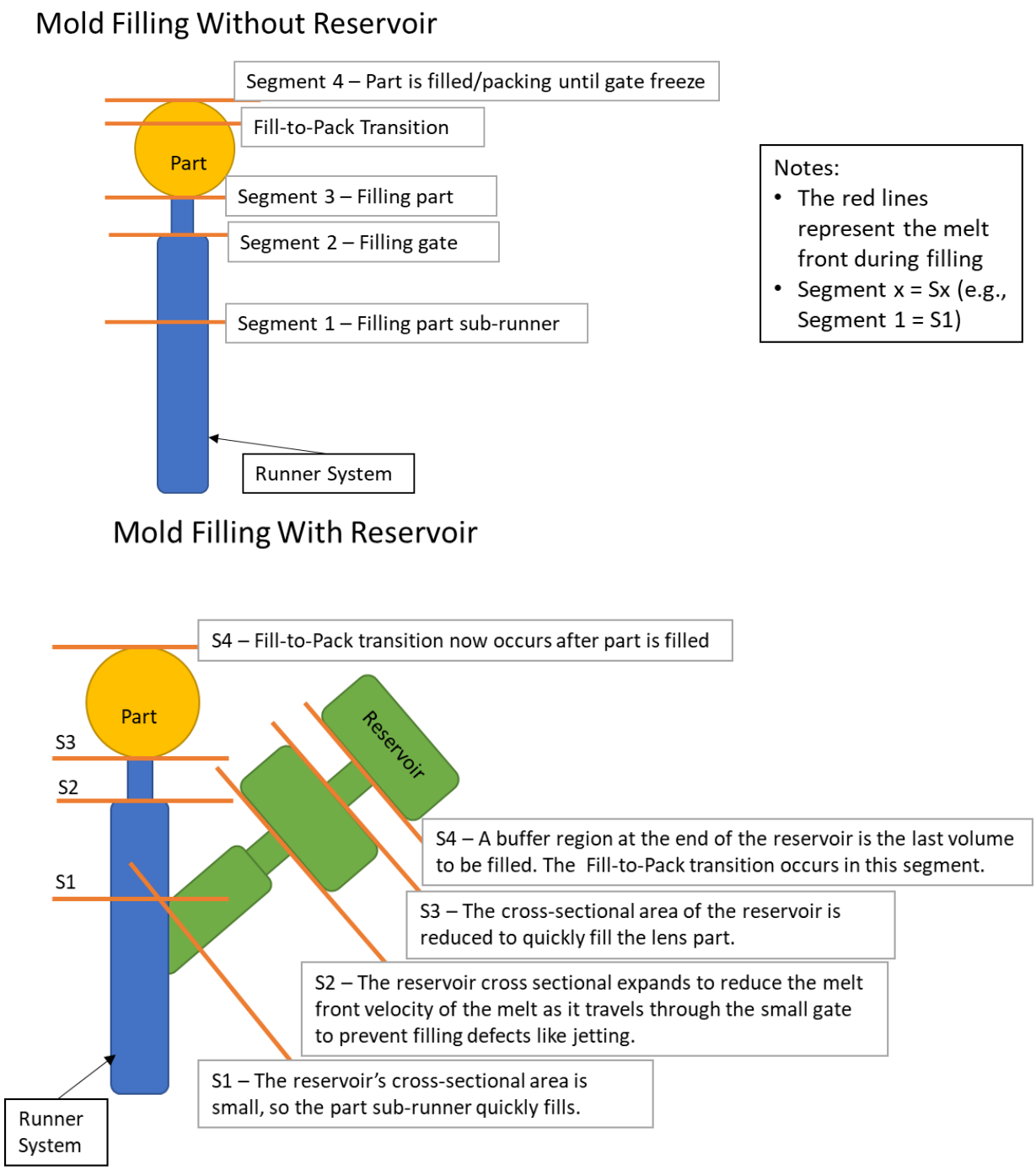

Figure 28: The basic reservoir concept.

The initial approach to develop a reservoir was a guess-and-check engineering intuition approach. With this approach changes in the reservoir design were made based on examination of previous simulation results and how the material was suspected to flow. Since the lens parts used in the initial testing were geometrically similar disk shapes and due to the complex flow

properties of polymers finetuning, the reservoir to be optimized for a particular lens was very difficult. An approach using a simple mass balance was considered next. Finally, to provide a more detailed methodical approach a mathematical procedure using mass and momentum balance equations was proposed.

2.1 Derivations

The following two derivations were completed with guidance from the textbooks, *Transport Phenomena* [59] and *Polymer Processing: Modeling and Simulation* [60]. The notation mostly follows *Transport Phenomena* [59]. Table 19 gives a brief glossary of the notation used. Figure 29 shows the geometry of interest. The channel/sub-runners leading to the parts are designated as channels 1 and 2, and the reservoir channel is designated as channel 3. Therefore, notation shown in Table 19 with a 1, 2, or 3 subscript corresponds to that channel. Since channels 1 and 2 are mirrored copies, they are assumed to be identical in these derivations.

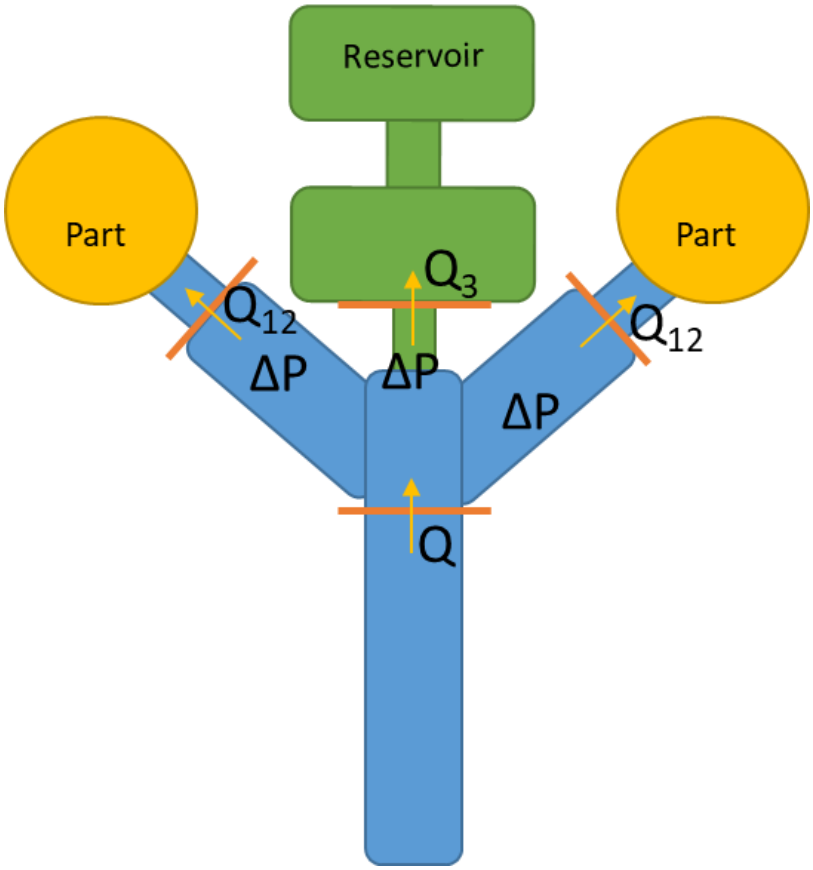

Figure 29: Approximate control volume for derivations.

Table 19: Derivation notation guide.

Variable	Description
Q	Scalar volumetric flow rate
$\boldsymbol{v}$	Vector of melt front velocity
$\bar{v}$	Scalar average melt front velocity
p	Scalar pressure
$\boldsymbol{g}$	Vector gravity force
ρ	Scalar material density
$\boldsymbol{\tau}$	Tensor shear stress
μ	Scalar material viscosity
m and n	Scalar Power-Law model constants

The system volumetric flow rate is assumed to be set and held constant, and we can relate it to the three channels by a volume balance or:

$$Q = 2Q_{12} + Q_3 \tag{5}$$

It would be ideal to fill the lens parts with a constant melt front speed, thus we prescribe a value for the average velocity term, $\overline{v_{12}}$ for the lens channels. Further, the pressure drop though the length of each of the channels is held to be equal, thus the pressure relation yields:

$$\Delta p_{12} = \Delta p_3 = \Delta p \tag{6}$$

The geometry shown in Figure 29 is made up of cross-sectional areas that can be approximated by two shapes: First, the runner portion of channels 1 and 2 are circular, second, the cross-sectional shape of the gate and part regions are roughly rectangular along the material flow direction. The reservoir channel is taken to be circular (with varying diameter). It is important to note that the reservoir geometry is taken to be circular based on ease of calculations, since a circular cross section can be defined by one geometry parameter. The first derivative given is for the circular geometry, then the rectangular geometry solution is presented.

2.1.1 Circular Regions/Segments – Hagen-Poiseuille Equation

Figure 30 shows a rough schematic of the system. The corresponding assumptions and definitions are:

- Flow is axis-symmetric

- Cylindrical coordinates $(r,\ \theta,\ z)$
- $v_z = v_z(r),\ \ v_r = v_\theta = 0,\ \ p = p(z)$
- Only non-zero term of the rate-of-deformation is zr
- Considering the generalized Newtonian flow, only τ_{zr} is nonzero and $\tau_{zr} = \tau_{zr}(r)$

There are two boundary conditions:

- Symmetry at $r = 0$ which requires that the flow front slope equals zero
- No-slip wall condition at $r = R$, thus, $v_z(r = R) = 0$

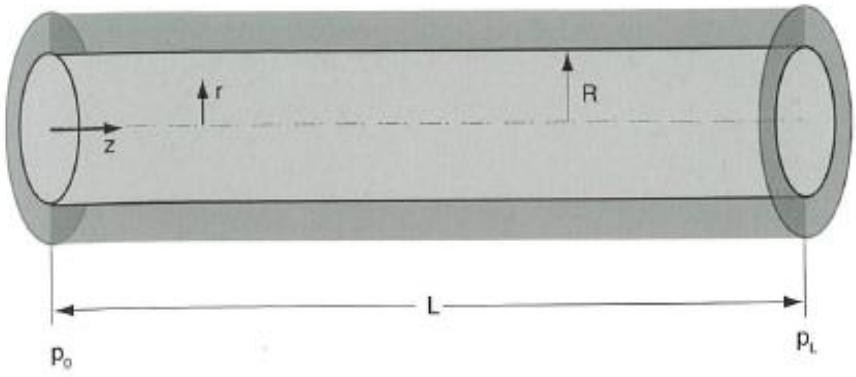

Figure 30: Flow through a circular tube [60].

Continuity Balance:

$$\frac{\partial \rho}{\partial t} + \frac{1}{r}\frac{\partial}{\partial r}(\rho r v_r) + \frac{1}{r}\frac{\partial}{\partial \theta}(\rho v_\theta) + \frac{\partial}{\partial z}(\rho v_z) = 0 \qquad (7)$$

Momentum Balance

r)
$$\rho\left(\frac{\partial v_r}{\partial t} + v_r\frac{\partial v_r}{\partial r} + \frac{v_\theta}{r}\frac{\partial v_r}{\partial \theta} - \frac{v_\theta^2}{r} + v_z\frac{\partial v_r}{\partial z}\right) = -\frac{\partial p}{\partial r} - \left(\frac{1}{r}\frac{\partial (r\tau_{rr})}{\partial r} + \frac{1}{r}\frac{\partial \tau_{r\theta}}{\partial \theta} - \frac{\tau_{\theta\theta}}{r} + \frac{\partial \tau_{rz}}{\partial z}\right) + \rho g_r$$

θ)
$$\rho\left(\frac{\partial v_\theta}{\partial t} + v_r\frac{\partial v_\theta}{\partial r} + \frac{v_\theta}{r}\frac{\partial v_\theta}{\partial \theta} + \frac{v_r v_\theta}{r} + v_z\frac{\partial v_\theta}{\partial z}\right) = -\frac{1}{r}\frac{\partial p}{\partial \theta} - \left(\frac{1}{r^2}\frac{\partial (r^2\tau_{r\theta)}}{\partial r} + \frac{1}{r}\frac{\partial \tau_{\theta\theta}}{\partial \theta} + \frac{\partial \tau_{\theta z}}{\partial z}\right) + \rho g_\theta \qquad (8)$$

z)
$$\rho\left(\frac{\partial v_z}{\partial t} + v_r\frac{\partial v_z}{\partial r} + \frac{v_\theta}{r}\frac{\partial v_z}{\partial \theta} + v_z\frac{\partial v_z}{\partial z}\right) = -\frac{\partial p}{\partial z} - \left(\frac{1}{r}\frac{\partial (r\tau_{rz})}{\partial r} + \frac{1}{r}\frac{\partial \tau_{\theta z}}{\partial \theta} + \frac{\partial \tau_{zz}}{\partial z}\right) + \rho g_z$$

Shear Stress

$$\tau_{rr} = -\mu\left[2\frac{\partial v_r}{\partial r} - \frac{2}{3}(\boldsymbol{\nabla}\cdot\boldsymbol{v})\right] \qquad \tau_{r\theta} = \tau_{\theta r} = -\mu\left[r\frac{\partial}{\partial r}\left(\frac{v_\theta}{r}\right) + \frac{1}{r}\frac{\partial v_r}{\partial \theta}\right]$$
$$\tau_{\theta\theta} = -\mu\left[2\left(\frac{1}{r}\frac{\partial v_\theta}{\partial \theta} + \frac{v_r}{r}\right) - \frac{2}{3}(\boldsymbol{\nabla}\cdot\boldsymbol{v})\right] \qquad \tau_{\theta z} = \tau_{z\theta} = -\mu\left[\frac{\partial v_\theta}{\partial z} + \frac{1}{r}\frac{\partial v_z}{\partial \theta}\right] \qquad (9)$$
$$\tau_{zz} = -\mu\left[2\frac{\partial v_z}{\partial z} - \frac{2}{3}(\boldsymbol{\nabla}\cdot\boldsymbol{v})\right] \qquad \tau_{zr} = \tau_{rz} = -\mu\left[\frac{\partial v_z}{\partial r} + \frac{\partial v_r}{\partial z}\right]$$
$$(\boldsymbol{\nabla}\cdot\boldsymbol{v}) = \frac{1}{r}\frac{\partial(r v_r)}{\partial r} + \frac{1}{r}\frac{\partial v_\theta}{\partial \theta} + \frac{\partial v_z}{\partial z}$$

Power Law

$$\boldsymbol{\tau} = -\{\mu\}\Delta \qquad \mu = m\left|\sqrt{\frac{1}{2}(\Delta:\Delta)}\right|^{n-1}$$
$$\Delta = \begin{bmatrix} 2\frac{\partial v_r}{\partial r} & r\frac{\partial}{\partial r}\left(\frac{v_\theta}{r}\right) + \frac{1}{r}\frac{\partial v_r}{\partial \theta} & \frac{\partial v_r}{\partial z} + \frac{\partial v_z}{\partial r} \\ r\frac{\partial}{\partial r}\left(\frac{v_\theta}{r}\right) + \frac{1}{r}\frac{\partial v_r}{\partial \theta} & 2\left(\frac{1}{r}\frac{\partial v_\theta}{\partial \theta} + \frac{v_r}{r}\right) & \frac{1}{r}\frac{\partial v_z}{\partial \theta} + \frac{\partial v_\theta}{\partial z} \\ \frac{\partial v_r}{\partial z} + \frac{\partial v_z}{\partial r} & \frac{1}{r}\frac{\partial v_z}{\partial \theta} + \frac{\partial v_\theta}{\partial z} & 2\frac{\partial v_z}{\partial z} \end{bmatrix} \qquad (10)$$

Based on the assumptions given, every term in the continuity balance (cf. equation *(7)*) and the r and θ direction momentum balances (cf. equation *(8)*) go to zero. Applying the assumptions to the z direction equation leads to the left-hand side terms going to zero. Then the right-hand side reduces to:

$$0 = -\frac{\partial p}{\partial z} - \frac{1}{r}\frac{\partial}{\partial r}(r\tau_{rz}) \qquad (11)$$

Reordering:

$$-\frac{\partial}{\partial r}(r\tau_{rz}) = r\frac{\partial p}{\partial z} \qquad (12)$$

Considering the shear stress all terms in the tensor go to zero except:

$$\tau_{rz} = -\mu \frac{\partial v_z}{\partial r} \tag{13}$$

The viscosity term simplifies to:

$$\mu = m \left| \sqrt{\left(\frac{\partial v_z}{\partial r}\right)^2} \right|^{n-1} \tag{14}$$

The term inside the absolute value signs can never be less than zero thus,

$$\mu = m \left(\frac{\partial v_z}{\partial r}\right)^{n-1} \tag{15}$$

And:

$$\tau_{rz} = -m \left(\frac{\partial v_z}{\partial r}\right)^{n} \tag{16}$$

Then:

$$\frac{\partial}{\partial r}\left(r \left(\frac{\partial v_z}{\partial r}\right)^{n}\right) = \frac{r}{m}\frac{\partial p}{\partial z} \tag{17}$$

This second order differential equation can be solved by integrating twice and applying the boundary conditions yielding velocity in the *z* direction as a function of *r*:

$$v_z = -\left(\frac{1}{2m}\frac{\Delta p}{L}\right)^{\frac{1}{n}}\left(\frac{n}{n+1}\right)\left(R^{\frac{1+n}{n}} - r^{\frac{1+n}{n}}\right) \quad (18)$$

Average velocity through the tube can be found:

$$\overline{v_z} = \frac{\int_0^{2\pi}\int_0^R v_z r dr d\theta}{\int_0^{2\pi}\int_0^R r dr d\theta} = \left(\frac{1}{2m}\frac{\Delta \mathrm{p}}{L}\right)^{\frac{1}{n}}\left(\frac{n}{1+3n}\right)R^{\frac{1+n}{n}} \quad (19)$$

Volumetric flow rate through the tube can be determined by integrating over the cross-sectional area:

$$Q = \int_0^{2\pi}\int_0^R v_z r dr d\theta = \left(\frac{R^{1+3n}}{2m}\frac{\Delta \mathrm{p}}{L}\right)^{\frac{1}{n}}\left(\frac{\pi n}{1+3n}\right) \quad (20)$$

2.1.2 Rectangular Regions/Segments

Figure 31 shows a rough schematic of the system. The corresponding assumptions and definitions are:

- Flow is symmetric
- Cartesian coordinates (x, y, z)
- $v_z = v_z(y),\ v_x = v_y = 0,\ p = p(z)$

There are two boundary conditions:

- Velocity profile is at a maximum value at the center of the velocity profile thus, $\frac{\partial v_z(y=0)}{\partial y} = 0$
- No-slip wall condition at y $= \pm\frac{H}{2}$, thus, $v_z\left(y = \pm\frac{H}{2}\right) = 0$

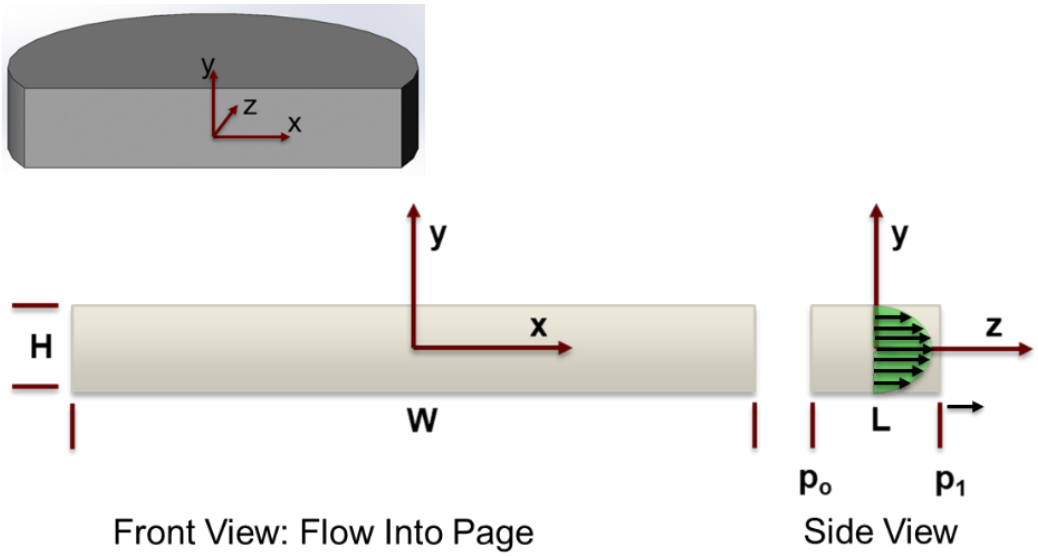

Figure 31: Flow through a rectangular tube to approximate the flow through a lens segment.

Continuity Balance

$$\frac{\partial \rho}{\partial t} + \frac{\partial}{\partial x}(\rho v_x) + \frac{\partial}{\partial y}(\rho v_y) + \frac{\partial}{\partial z}(\rho v_z) = 0 \qquad (21)$$

Momentum Balance

x) $$\rho\left(\frac{\partial v_x}{\partial t} + v_x\frac{\partial v_x}{\partial x} + v_y\frac{\partial v_x}{\partial y} + v_z\frac{\partial v_x}{\partial z}\right) = -\frac{\partial p}{\partial x} - \left(\frac{\partial \tau_{xx}}{\partial x} + \frac{\partial \tau_{yx}}{\partial y} + \frac{\partial \tau_{zx}}{\partial z}\right) + \rho g_x$$

y) $$\rho\left(\frac{\partial v_y}{\partial t} + v_x\frac{\partial v_y}{\partial x} + v_y\frac{\partial v_y}{\partial y} + v_z\frac{\partial v_y}{\partial z}\right) = -\frac{\partial p}{\partial y} - \left(\frac{\partial \tau_{xy}}{\partial x} + \frac{\partial \tau_{yy}}{\partial y} + \frac{\partial \tau_{zy}}{\partial z}\right) + \rho g_y \qquad (22)$$

z) $$\rho\left(\frac{\partial v_z}{\partial t} + v_x\frac{\partial v_z}{\partial x} + v_y\frac{\partial v_z}{\partial y} + v_z\frac{\partial v_z}{\partial z}\right) = -\frac{\partial p}{\partial z} - \left(\frac{\partial \tau_{xz}}{\partial x} + \frac{\partial \tau_{yz}}{\partial y} + \frac{\partial \tau_{zz}}{\partial z}\right) + \rho g_z$$

Shear Stress

$$\tau_{xx} = -\mu\left[2\frac{\partial v_x}{\partial x} - \frac{2}{3}(\boldsymbol{\nabla}\cdot\boldsymbol{v})\right] \qquad \tau_{xy} = \tau_{yx} = -\mu\left[\frac{\partial v_x}{\partial y} + \frac{\partial v_y}{\partial x}\right]$$

$$\tau_{yy} = -\mu\left[2\frac{\partial v_y}{\partial y} - \frac{2}{3}(\boldsymbol{\nabla}\cdot\boldsymbol{v})\right] \qquad \tau_{yz} = \tau_{zy} = -\mu\left[\frac{\partial v_y}{\partial z} + \frac{\partial v_z}{\partial y}\right] \qquad (23)$$

$$\tau_{zz} = -\mu\left[2\frac{\partial v_z}{\partial z} - \frac{2}{3}(\boldsymbol{\nabla}\cdot\boldsymbol{v})\right] \qquad \tau_{zx} = \tau_{xz} = -\mu\left[\frac{\partial v_z}{\partial x} + \frac{\partial v_x}{\partial z}\right]$$

$$(\boldsymbol{\nabla}\cdot\boldsymbol{v}) = \frac{\partial v_x}{\partial x} + \frac{\partial v_y}{\partial y} + \frac{\partial v_z}{\partial z}$$

Power Law

$$\boldsymbol{\tau} = -\{\mu\}\Delta \qquad \mu = m\left|\sqrt{\frac{1}{2}(\Delta:\Delta)}\right|^{n-1} \qquad \Delta_{ij} = \left(\frac{\partial v_i}{\partial x_j} + \frac{\partial v_j}{\partial x_i}\right)$$

$$\Delta = \begin{bmatrix} 2\frac{\partial v_x}{\partial x} & \frac{\partial v_x}{\partial y} + \frac{\partial v_y}{\partial x} & \frac{\partial v_x}{\partial z} + \frac{\partial v_z}{\partial x} \\ \frac{\partial v_y}{\partial x} + \frac{\partial v_x}{\partial y} & 2\frac{\partial v_y}{\partial y} & \frac{\partial v_y}{\partial z} + \frac{\partial v_z}{\partial y} \\ \frac{\partial v_z}{\partial x} + \frac{\partial v_x}{\partial z} & \frac{\partial v_z}{\partial y} + \frac{\partial v_y}{\partial z} & 2\frac{\partial v_z}{\partial z} \end{bmatrix} \quad (24)$$

After applying the assumptions and geometry, every term in the continuity balance and the x and y equations of the momentum balance go to zero. In the z direction momentum balance equation, all of the terms on the left-hand side go to zero and the right-hand side simplifies to:

$$0 = -\frac{\partial p}{\partial z} - \frac{\partial \tau_{yz}}{\partial y} \quad (25)$$

The shear stress and Power-Law equations simplify to:

$$\tau_{yz} = -\mu\frac{\partial v_z}{\partial y} \qquad \mu = m\left|\frac{\partial v_z}{\partial y}\right|^{n-1} \quad (26)$$

The absolute value term in viscosity (μ) means combining the above equations yields a non-linear second order differential equation:

$$\frac{1}{m}\frac{\partial p}{\partial z} = \frac{\partial}{\partial y}\left(\left|\frac{\partial v_z}{\partial y}\right|^{n-1}\frac{\partial v_z}{\partial y}\right) \quad (27)$$

To solve the non-linear second order differential equation, consider splitting the flow front in half along the z axis. The flow front is symmetric so only one half must be solved to describe the flow.

The "top" half where $\frac{\partial v_z}{\partial y} \leq 0$ and $0 \leq y \leq \frac{H}{2}$ has a negative velocity profile (melt front) slope. This means that the differential equation shown above must remain non-linear since we cannot safely ignore the absolute value sign.

The "bottom" half where $\frac{\partial v_z}{\partial y} \geq 0$ and $-\frac{H}{2} \leq y \leq 0$ has a positive velocity profile (melt front) slope. This means that the differential equation above can be simplified to,

$$\frac{1}{m}\frac{\partial p}{\partial z} = \frac{\partial}{\partial y}\left(\frac{\partial v_z}{\partial y}\right)^n \tag{28}$$

Using the boundary condition this equation can then be integrated twice to yield the velocity in the *z* direction as a function of *x*:

$$v_z = \left(\frac{1}{m}\frac{\Delta p}{L}\right)^{\frac{1}{n}}\left(\frac{n}{1+n}\right)\left[y^{\frac{1+n}{n}} + \left(\frac{H}{2}\right)^{\frac{1+n}{n}}\right] \tag{29}$$

Average velocity though the channel can be calculated:

$$\overline{v_z} = \frac{\int_{-\frac{H}{2}}^{0}\int_{-\frac{W}{2}}^{\frac{W}{2}} v_z dxdy}{\int_{-\frac{H}{2}}^{0}\int_{-\frac{W}{2}}^{\frac{W}{2}} dxdy} = \left(\frac{H}{2}\right)^{\frac{1+n}{n}}\left(\frac{1}{m}\frac{\Delta p}{L}\right)^{\frac{1}{n}}\left(\frac{n(1+3n)}{(1+n)(1+2n)}\right) \tag{30}$$

Volumetric flow rate through the tube then is two times the integration over half the cross-sectional area:

$$Q = 2\int_{-\frac{H}{2}}^{0}\int_{-\frac{W}{2}}^{\frac{W}{2}} v_z dxdy = 2W\left(\frac{1}{L}\right)^{\frac{1}{n}}\left(\frac{H}{2}\right)^{\frac{1+2n}{n}}\left(\frac{\Delta p}{m}\right)^{\frac{1}{n}}\left(\frac{n(1+3n)}{(1+n)(1+2n)}\right) \tag{31}$$

2.1.3 Application of the Derived Equations

With the derivations given for the circular and rectangular tube flows, a piecewise solution can be found for the geometry given. Figure 32 shows roughly how the lens sub-runner, gate, and part are segmented to allow for the piecewise solution and Figure 33 shows an example of the cross-sectional area measurements on a lens part.

Generally, the part sub-runner will have a circular geometry and then the gate and part regions will be rectangular. The following two sections will describe the piecewise solutions for the two cases, namely, (i) circular channel 1 and 2 and circular channel 3 (reservoir) and (ii) rectangular channel 1 and 2 and circular channel 3 (reservoir). With the solutions given for the circular and rectangular tube flow it would be easy to determine the solution for other cases as needed.

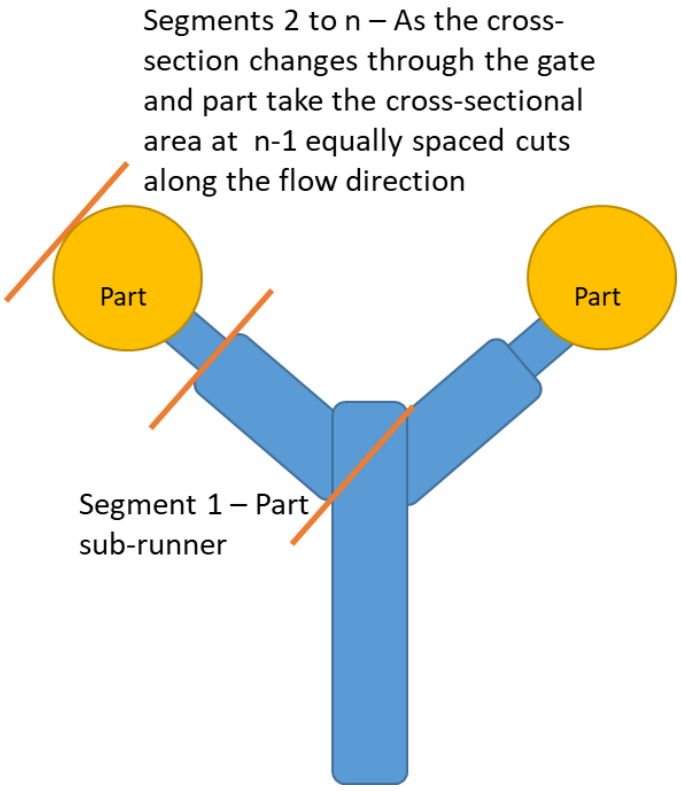

Figure 32: Geometry set-up for the piecewise solution.

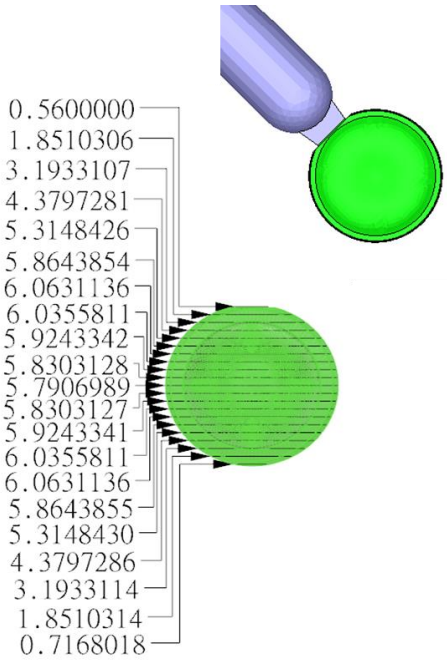

Figure 33: The cross-sectional area of a segmentized lens.

2.1.3.1 Circular/Circular Regions – Segment 1

- The known parameters are: $Q,\ \overline{v_{12}},\ d_{12}, L_{12},\ d_3\ or\ l_3,\ n,\ m.$
- The parameters to be solved for are: $Q_{12},\ \Delta p,\ Q_3, \overline{v_3}, L_3\ or\ d_3.$

First, the volumetric flow rate of channels 1 and 2 can be found from the prescribed melt front velocity $\overline{v_{12}}$ by combining the relations in Equations 19 and 20:

$$Q_{12} = \pi \left(\frac{d_{12}}{2}\right)^2 \overline{v_{12}} \tag{32}$$

Then, from the volumetric flow rate the pressure drop can be determined by reordering Equation 20:

$$\Delta p = 2mL_{12}\left(\frac{(1+3n)Q_{12}}{\pi n}\right)^n \left(\frac{d_{12}}{2}\right)^{-(1+3n)} \tag{33}$$

Equation 5 can then be used to determine the volumetric flow rate of channel 3:

$$Q_3 = Q - 2Q_{12} \tag{34}$$

Combining the relations in Equations 19 and 20 yield a relation for the melt front velocity of channel 3:

$$\overline{v_3} = \frac{4}{\pi}\frac{Q_3}{d_3^2} \tag{35}$$

Finally, using the relation presented in Equation 20 either the diameter or the length of the channel 3 (reservoir) segment can be determined. The equation used will be determined by which of the two parameters has been prescribed in the initial set up.

$$d_3 = 2\left(\frac{(1+3n)Q_3}{\pi n}\right)^{\frac{n}{1+3n}}\left(\frac{2mL_3}{\Delta p}\right)^{\frac{1}{1+3n}} \tag{36}$$

$$L_3 = \frac{\Delta p}{2m}\left(\frac{\pi n}{(1+3n)Q_3}\right)^{n}\left(\frac{d_3}{2}\right)^{1+3n} \tag{37}$$

2.1.3.2 Rectangular/Circular Regions – Segment 2 to *n*

- The known parameters are: $Q,\ \overline{v_{12}},\ H_{12},\ W_{12},\ L_{12},\ d_3\ or\ L_3,\ n,\ m.$
- The unknown parameters are: $Q_{12},\ \Delta p,\ Q_3, \overline{v_3}, L_3\ or\ d_3.$

First, the volumetric flow rate of channels 1 and 2 can be found from the prescribed melt front velocity $\overline{v_{12}}$ by combining the relations in Equations 30 and 31:

$$Q_{12} = H_{12}W_{12}\overline{v_{12}} \tag{38}$$

Then, from the volumetric flow rate the pressure drop can be determined by reordering Equation 31:

$$\Delta p = mL_{12}\left(\frac{2}{H_{12}}\right)^{1+2n}\left(\frac{Q_{12}(1+n)(1+2n)}{2W_{12}n(1+3n)}\right)^{n} \tag{39}$$

Equation 5 can then be used to determine the volumetric flow rate of channel 3:

$$Q_3 = Q - 2Q_{12} \quad (40)$$

Now with the volumetric flow rate of channel 3 and the pressure drop relation, Equations 35 and 36 or 37 can be used to determine the melt front velocity of channel 3 and the diameter or length of channel 3 (reservoir) for that segment.

The circular/circular or rectangular/circular solutions are used for each segment. Since the volumetric flow rate of the system and the melt front velocity of channels 1 and 2 are held constant the segments are thus connected but can be calculated independently.

2.1.4 Geometry

The three approaches for reservoir design were developed into ten geometry cases. One branch of a radially symmetric mold was used with ten variations in the reservoir geometry located centered between the two-part cavities. Figure 34 shows the different geometry cases. Table 20 gives the basic geometry of the lens part studied. Figure 35 shows the design approach for the engineering intuition approach. The different engineering intuition approach varied three different dimensions. In Figure 34, the first dimension in the name of the engineering intuition reservoirs corresponds to the second narrow region described in Figure 35. The first wide region and second wider region were held equal and were given as the second dimension in the engineering intuition name after the "T".

To allow for optical simulations meshing of the part is completed in Rhino so the part can be meshed with fully solid hexahedron or prism elements. The runner system and reservoir are meshed in Moldex3D with the default boundary layer meshing. Table 26 shows the simulation processing parameters used. For each geometry case three processing parameters were varied three levels thus 27 runs were completed for each geometry case.

Table 20: Geometry parameters of lens.

Volume (mm^3)	Radius (mm)	Area (mm^2)	Thickness at center (mm)	Approximate Thickness (Volume/Area) (mm)	Approximate Aspect Ratio (*D*iameter/*T*hickness) (-)
8.9	2.1	13.9	0.39	0.64	6.6

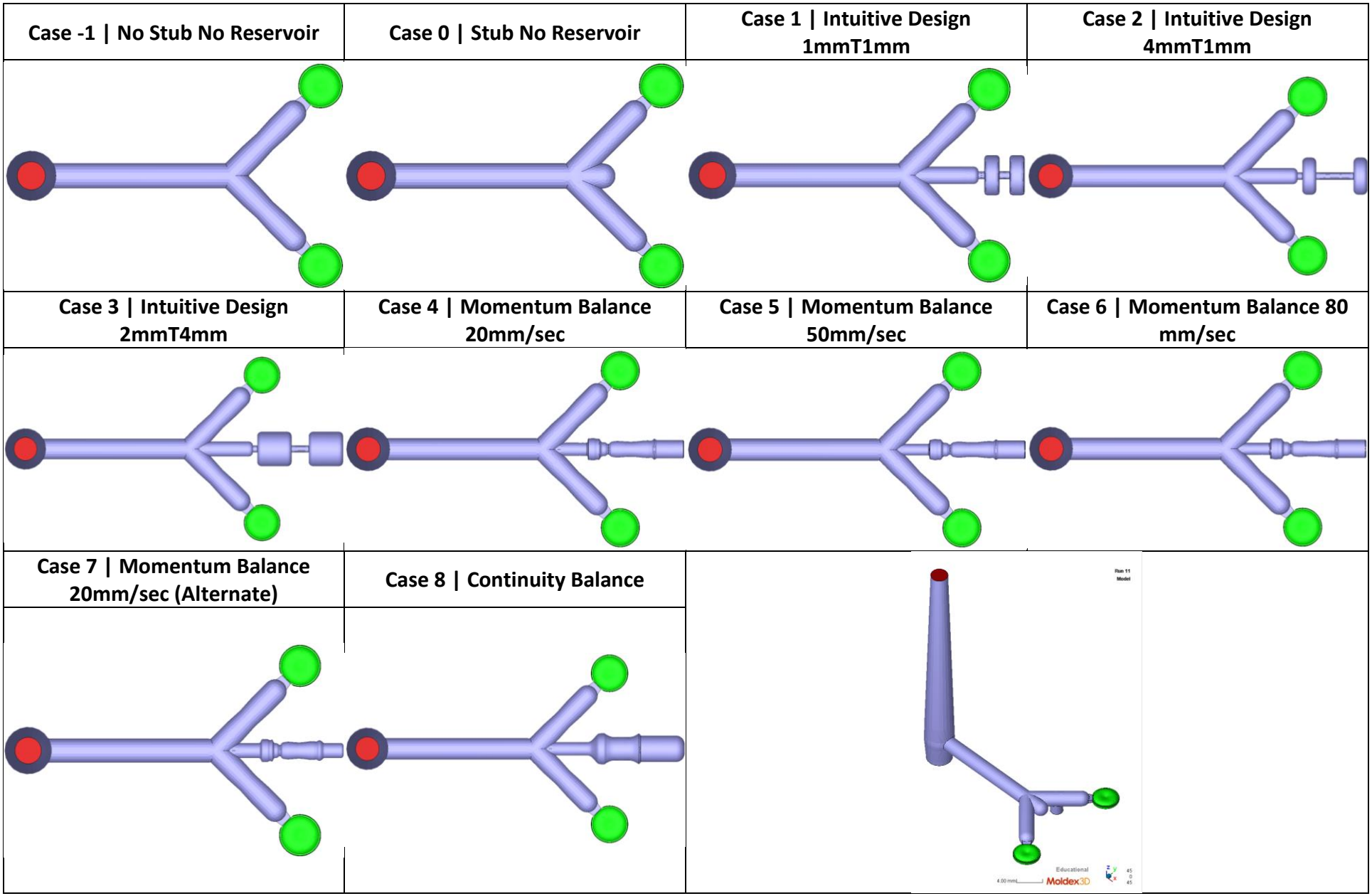

Figure 34: The mold with various reservoirs used in this study. The parts are green, the runners are blue, and the melt inlet is red. This mold is a simplified version of a radially symmetrical mold with multiple branches.

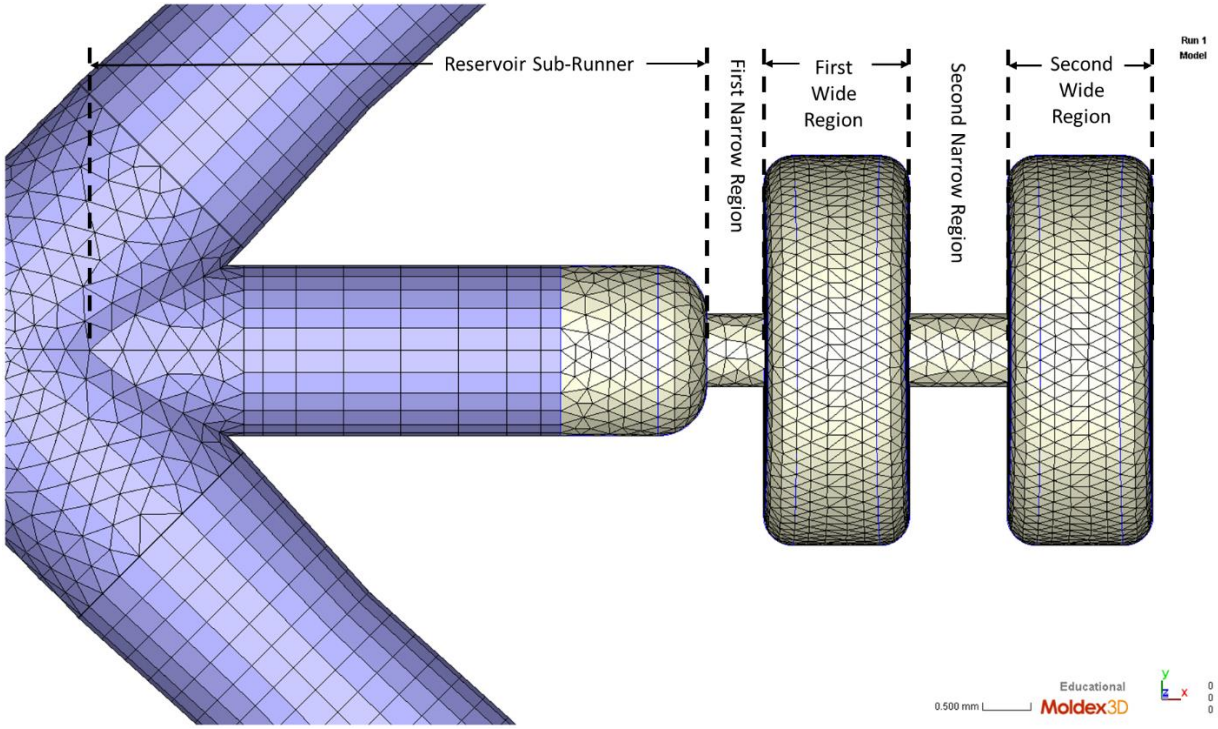

Figure 35: The engineering intuition reservoir design. The sub-runner has a diameter of 1.75 mm in every case.

The geometry parameters of the reservoirs designed via calculating the momentum and mass balance equations are given in Table 21, Table 22, Table 23, Table 24, and Table 25, respectively. The reservoirs were all assumed to be circular in cross-section and the specified diameter and length at that diameter are given in each table. To complete the equations a constant value for the measurement spacing, volumetric flow rate, and melt front velocity were determined. The volumetric flow rate was taken from the simulation processing parameters and the melt front velocity was determined from simulation results from previous work. Table 25 shows the parameters for the reservoir designed considering only a mass or volume balance. For this simple equation only the measurement spacing needs to be specified. Table 24 shows the reservoir design for an alternate version of the momentum balance equation for 20 mm/sec flow rate. This reservoir was chosen to help to understand how the constant variables change the reservoir design.

Table 21: Reservoir Case 4. Momentum balance for 20 mm/sec flow rate.

	Length (m)	D_3 (m)	Measurement Spacing (m)
1	1.97E-04	2.3E-03	1.97E-04
2	5.91E-04	2.4E-03	**Volumetric Flow Rate, Q (m^3/s)**
3	1.97E-04	2.3E-03	3.80E-06
4	1.97E-04	2.2E-03	**Melt front velocity (m/s)**
5	1.97E-04	1.6E-03	0.35
6	1.97E-04	1.5E-03	
7	1.97E-04	1.4E-03	
8	1.97E-04	1.1E-03	
9	1.97E-04	1.5E-03	
10	1.97E-04	1.7E-03	
11	5.91E-04	1.8E-03	
12	1.58E-03	1.7E-03	
13	3.94E-04	1.8E-03	
14	7.88E-04	1.9E-03	
15	1.97E-04	2.2E-03	

Table 22: Reservoir Case 5. Momentum balance for 50 mm/sec flow rate.

Length (m)	D_3 (m)	Measurement Spacing (m)
1.97E-04	2.1E-03	1.97E-04
1.97E-04	2.2E-03	**Volumetric Flow Rate, Q (m^3/s)**
3.94E-04	2.3E-03	1.00E-05
3.94E-04	2.2E-03	**Melt front velocity (m/s)**
1.97E-04	1.6E-03	1.00
1.97E-04	1.5E-03	
1.97E-04	1.4E-03	
1.97E-04	1.1E-03	
1.97E-04	1.5E-03	
1.18E-03	1.7E-03	
7.88E-04	1.6E-03	
5.91E-04	1.7E-03	
3.94E-04	1.8E-03	
1.97E-04	1.9E-03	
3.94E-04	1.8E-03	
1.97E-04	2.2E-03	

Table 23: Reservoir Case 6. Momentum balance for 80 mm/sec flow rate.

Length (m)	D_3 (m)	Measurement Spacing (m)
1.97E-04	2.1E-03	1.97E-04
1.97E-04	2.2E-03	**Volumetric Flow Rate, Q (m^3/s)**
3.94E-04	2.3E-03	1.52E-05
3.94E-04	2.2E-03	**Melt front velocity (m/s)**
1.97E-04	1.6E-03	1.50
1.97E-04	1.5E-03	
1.97E-04	1.4E-03	
1.97E-04	1.1E-03	
1.97E-04	1.5E-03	
3.94E-04	1.7E-03	
1.97E-04	1.8E-03	
5.91E-04	1.7E-03	
7.88E-04	1.6E-03	
3.94E-04	1.7E-03	
5.91E-04	1.8E-03	
3.94E-04	1.9E-03	
1.97E-04	1.8E-03	
1.97E-04	2.2E-03	

Table 24: Reservoir Case 7. Alternate momentum balance for 20 mm/sec flow rate.

Length (m)	D_3 (m)	Measurement Spacing (m)
1.30E-04	2.3E-03	1.30E-04
1.30E-04	2.5E-03	**Volumetric Flow Rate, Q (m^3/s)**
1.30E-04	2.7E-03	3.80E-06
1.30E-04	2.8E-03	**Melt front velocity (m/s)**
2.60E-04	2.7E-03	0.40
1.30E-04	1.9E-03	
1.30E-04	1.8E-03	
1.30E-04	1.7E-03	
1.30E-04	1.3E-03	
1.30E-04	1.8E-03	
1.30E-04	2.0E-03	
3.90E-04	2.1E-03	
3.90E-04	2.0E-03	
3.90E-04	1.9E-03	
2.60E-04	2.0E-03	
1.30E-04	2.1E-03	
6.50E-04	2.2E-03	
1.30E-04	2.7E-03	

Table 25: Reservoir Case 8. Mass balance reservoir design.

Length (m)	D_3 (m)	Measurement Spacing (m)
1.97E-04	1.6E-03	1.97E-04
1.97E-04	1.7E-03	
1.97E-04	2.0E-03	
1.97E-04	2.4E-03	
1.97E-04	2.8E-03	
1.97E-04	3.3E-03	
7.88E-04	3.5E-03	
1.97E-04	3.3E-03	
1.97E-04	3.0E-03	
1.97E-04	2.9E-03	
3.94E-04	2.7E-03	
1.97E-04	2.6E-03	
1.38E-03	2.7E-03	
1.97E-04	2.6E-03	
3.94E-04	2.7E-03	
1.97E-04	2.9E-03	
1.97E-04	3.0E-03	
1.97E-04	3.3E-03	
1.97E-04	3.5E-03	

Table 26: Simulation processing parameters.

Fill Rate (Linear screw velocity) (mm/s)	20, 60, or 99
F/P Switch Over Point (% Filled Excluding Runner)	90, 95, or 100
Injection Pressure (MPa)	160
Packing Time (sec)	3
Packing Pressure Profile (% Pressure at End of Filling Stage)	50, 100, or 150
Melt Temperature (°C)	252
Mold Temperature (°C)	122
Cooling Time (s)	25
Material	Optical Polycarbonate

3. Results and Discussion

For each of the ten mold geometry cases 27 simulation runs were completed. Table 27 gives the minimum values achieved for retardation and volumetric shrinkage. Further, Figure 36 and Figure 37 show the plotted minimum values.

The average flow induced, thermally induced, and total retardation are displayed. The lowest average flow induced retardation occurs with Cases 2 and 7 where Case 2 is the Intuitive Design 4mmT1mm and Case 7 is the Momentum Balance 20mm/sec (Alternate). The average flow induced retardation is greater than the average thermally induced retardation, but they are not significantly different meaning both thermal and flow induced optical defects are relevant. The cases with a reservoir all have significantly lower average thermally induced retardation than the cases without a reservoir. The lowest average thermally induced retardation occurs with Case 2, Intuitive Design 4mmT1mm. Following the same trend, the average total retardation is the smallest with Cases 2 and 7. The smallest average flow induced retardation occurred with higher flow rates of 99 mm/sec or 60 mm/sec, lower V/P switch of 90 or 95%, and lowest packing pressure of 50% of the pressure at the end of filling. The thermally induced retardation followed similar trends except with the flow rate. The minimum occurred with a high flow rate for the no-reservoir Cases 1 and 2 but with the lowest flow rate of 20 mm/sec for all the reservoir cases.

Case 2 (Intuitive Design 4mmT1mm) is predicted to have the lowest average volumetric shrinkage value and Case 1 (No Stub No Reservoir) is predicted to have the minimum standard deviation volumetric shrinkage. The average volumetric shrinkage and the standard deviation of volumetric shrinkage through the lens parts are minimum at opposite extremes of the processing settings. The lowest standard deviation values all occurred at the lowest values of flow rate, V/P switch, and packing pressures tested. However, the minimum volumetric shrinkage values occur at the highest or nearly highest values of the processing parameters with the only exception being the V/P switch which alternated between 95 to 100% for the different cases.

Considering these minimum values shows that the reservoirs can yield improved part qualities and could benefit the manufacturing of high-quality optical components.

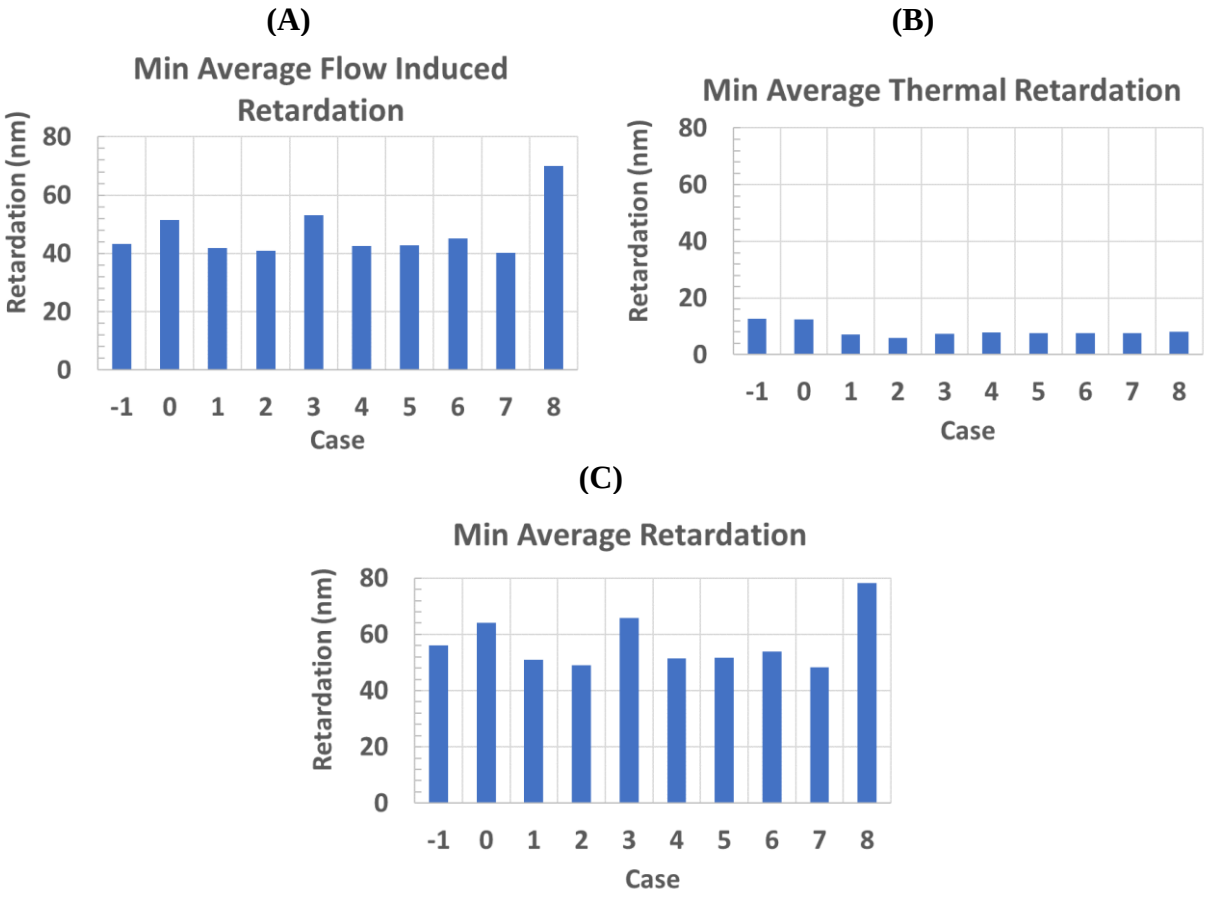

-1 No Stub No Reservoir
0 Stub No Reservoir
1 Intuitive Design 1mmT1mm
2 Intuitive Design 4mmT1mm
3 Intuitive Design 2mmT4mm
4 Momentum Balance 20mm/s
5 Momentum Balance 50mm/s
6 Momentum Balance 80 mm/s
7 Momentum Balance 20mm/s (Sept. 2021)
8 Continuity Balance

Figure 36: Minimum average retardation versus geometry case.

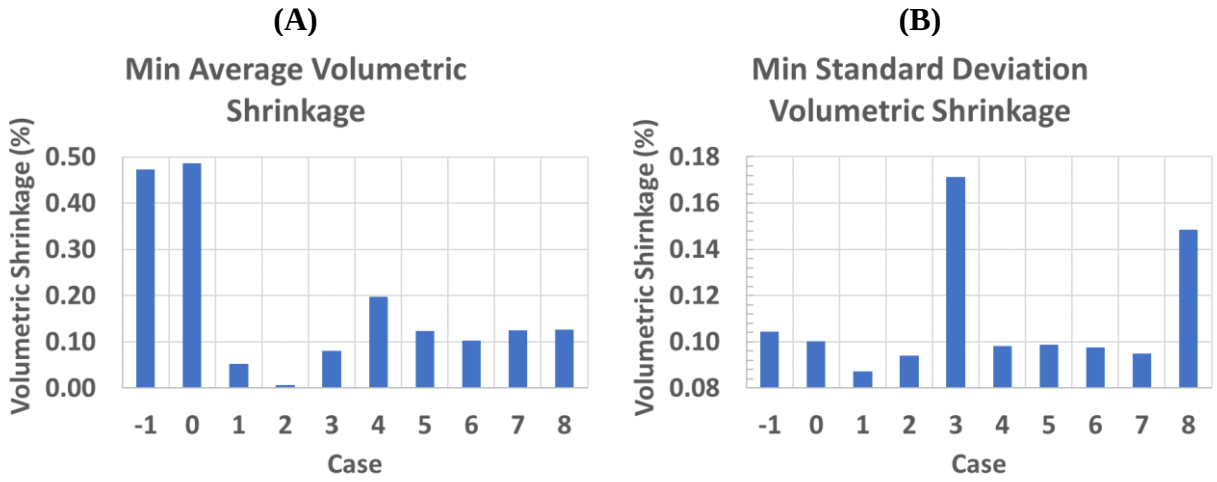

-1 No Stub No Reservoir
0 Stub No Reservoir
1 Intuitive Design 1mmT1mm
2 Intuitive Design 4mmT1mm
3 Intuitive Design 2mmT4mm
4 Momentum Balance 20mm/s
5 Momentum Balance 50mm/s
6 Momentum Balance 80 mm/s
7 Momentum Balance 20mm/s (Sept. 2021)
8 Continuity Balance

Figure 37: Minimum average and standard deviation volumetric shrinkage versus geometry case.

Table 27: Minimum, optimal, properties for each of the ten geometry cases and corresponding input parameters.

		Case -1		Case 0		Case 1		Case 2		Case 3		Case 4		Case 5		Case 6		Case 7		Case 8	
Average Flow Induced Retardation (nm)	**Flow Rate (mm/sec)**	43.4	99	51.4	99	41.7	99	40.8	99	53.2	60	42.4	99	42.9	99	45.2	99	40.2	99	69.9	60
	V/P Switch (%)		95		95		90		90		90		90		90		90		90		90
	Packing Pressure (%)		50		50		50		50		50		50		50		50		50		50
Average Thermally Induced Retardation (nm)	**Flow Rate (mm/sec)**	12.6	99	12.5	99	7.23	20	5.93	20	7.38	20	7.81	20	7.64	20	7.67	20	7.66	20	8.11	20
	V/P Switch (%)		90		90		90		90		90		90		90		90		90		90
	Packing Pressure (%)		50		50		50		50		50		50		50		50		50		50
Average Total Retardation (nm)	**Flow Rate (mm/sec)**	56.0	99	64.0	99	50.9	99	48.9	99	65.9	60	51.4	99	51.8	99	53.9	99	48.3	99	78.3	60
	V/P Switch (%)		95		95		90		90		90		90		90		90		90		90
	Packing Pressure (%)		50		50		50		50		50		50		50		50		50		50
Average Volumetric Shrinkage (%)	**Flow Rate (mm/sec)**	0.473	99	0.486	99	0.0527	99	0.00623	99	0.0813	99	0.197	99	0.124	99	0.103	99	0.124	99	0.127	99
	V/P Switch (%)		100		100		100		95/100		100		100		95		100		95		100
	Packing Pressure (%)		150		150		150		150		150		150		150		150		150		150
Standard Deviation Volumetric Shrinkage (%)	**Flow Rate (mm/sec)**	0.104	20	0.100	20	0.0873	20	0.0941	20	0.171	20	0.0982	20	0.0986	20	0.0975	20	0.0951	20	0.149	20
	V/P Switch (%)		90		90		90		90		90		90		90		90		90		90
	Packing Pressure (%)		50		50		50		50		50		50		50		50		50		50

Focusing on the minimum cases for the reservoir and no-reservoir simulations, the quality parameters are plotted versus the processing parameters for the 27 runs completed for each of the cases. Figure 38 shows the average flow induced retardation for Cases -1 and 7. The trends are similar, following the results of all the cases, and show that the flow induced retardation tend to be lower with the combination of higher flow rate, lower V/P switch, and lower packing pressure. This is likely due to the lower pressure experienced by the part with a lower V/P switch and lower packing pressure value since lower pressure reduces the amount of molded-in residual stress. The difference due to flow rate could be attributed to shear heating effects causing the melt to flow with lower viscosity, and therefore lower shear induced molecular orientation, with the higher flow rates. Figure 39 shows this trend of increased shear rate with increased flow rate, which is similar for all the geometry cases, for Case 2.

Figure 40 show the average thermally induced retardation for Cases 0 and 2. Between cases the trends match, and the trends also match those of the average flow induced retardation. As is expected, Figure 41 shows the same trends for the average total retardation for Cases-1 and 7 as was seen for the average flow induced retardation and average thermally induced retardation.

(A)

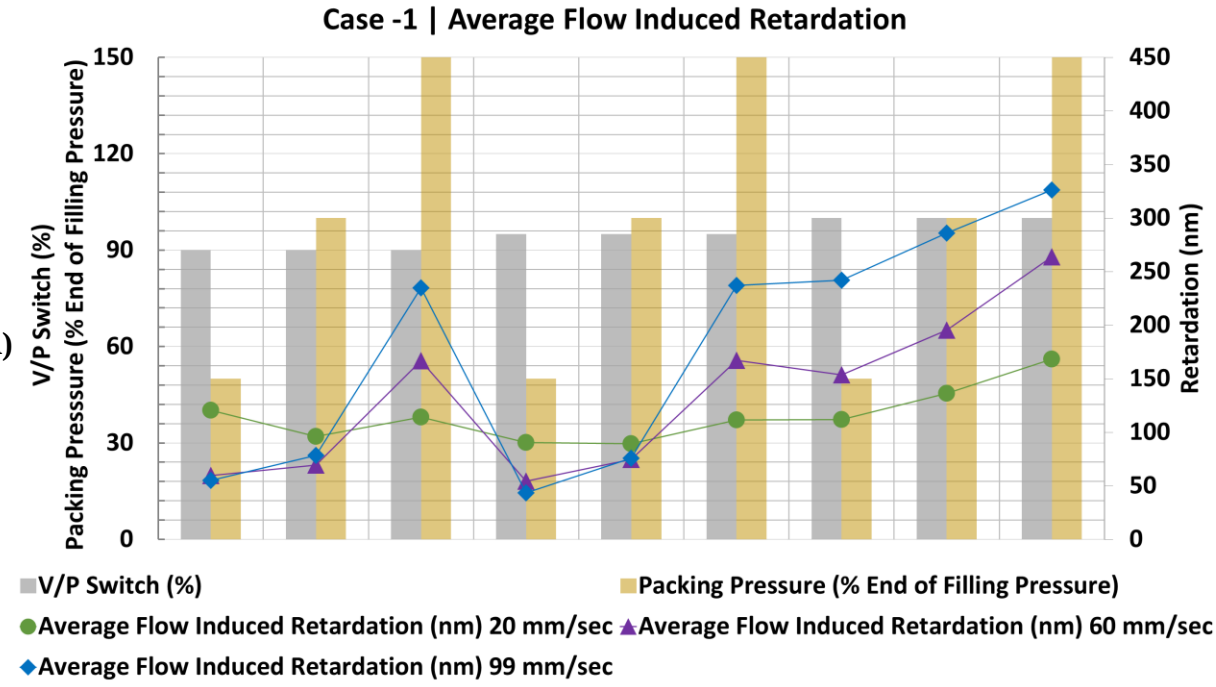

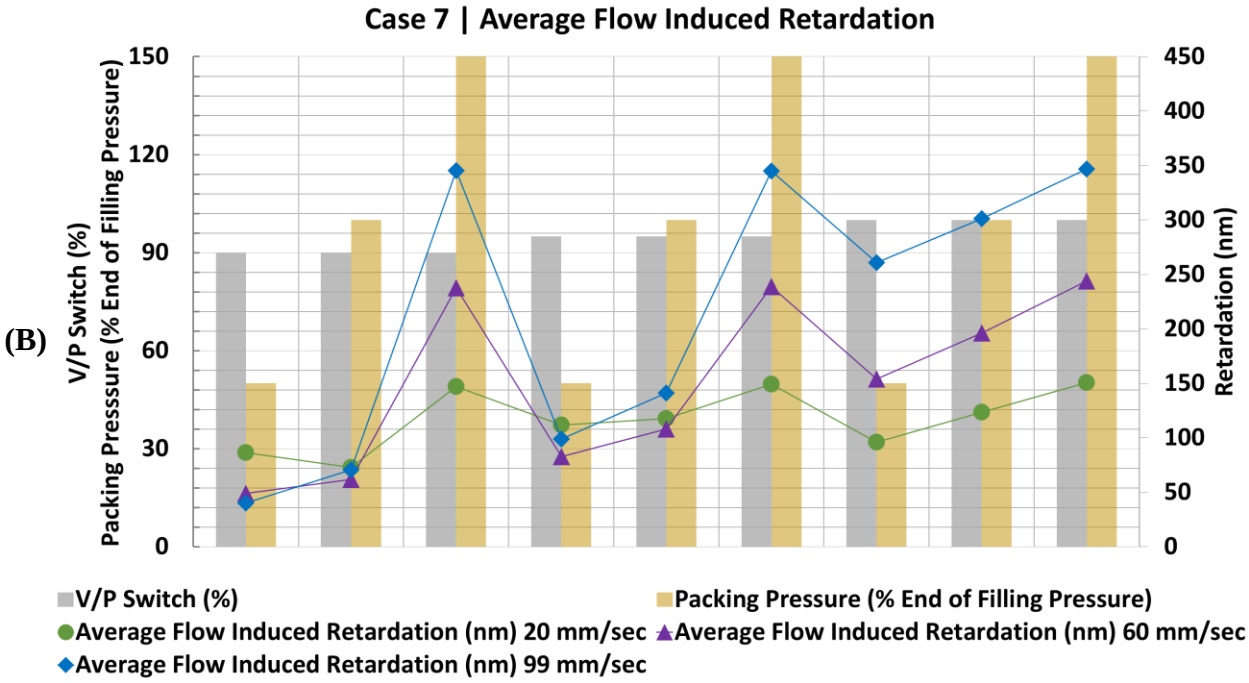

Figure 38: Average flow induced retardation versus processing parameters of V/P switch and packing pressure for the three flow rate levels.

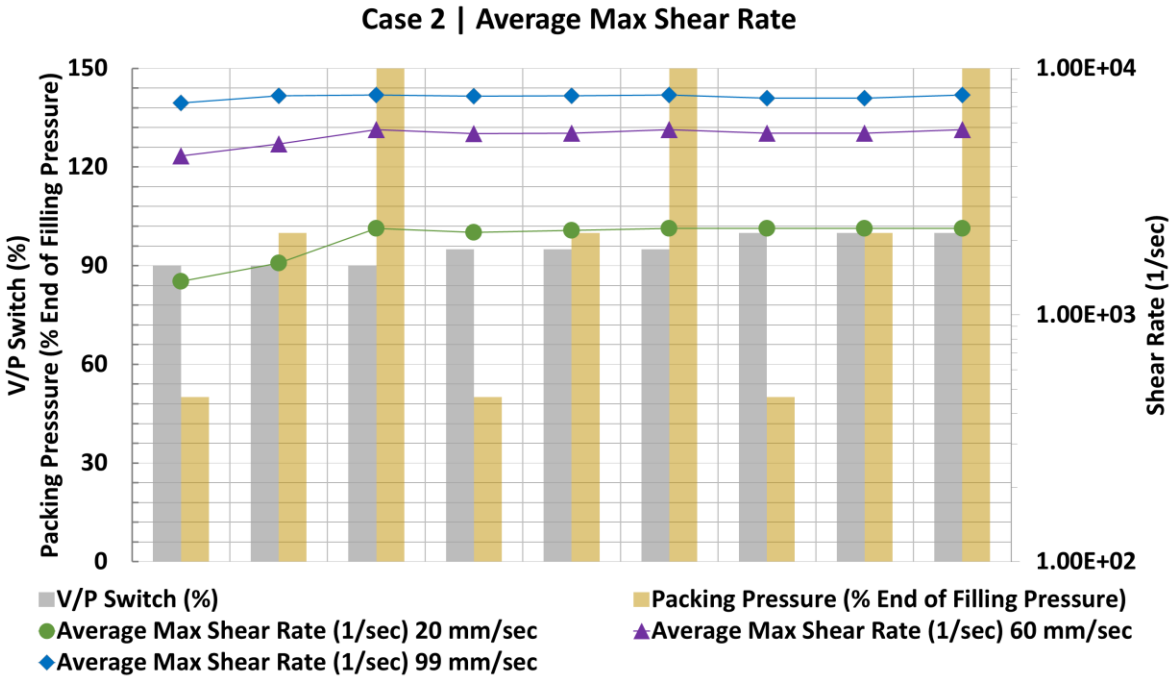

Figure 39: Shear rate versus processing parameters of V/P switch and packing pressure for the three flow rate levels.

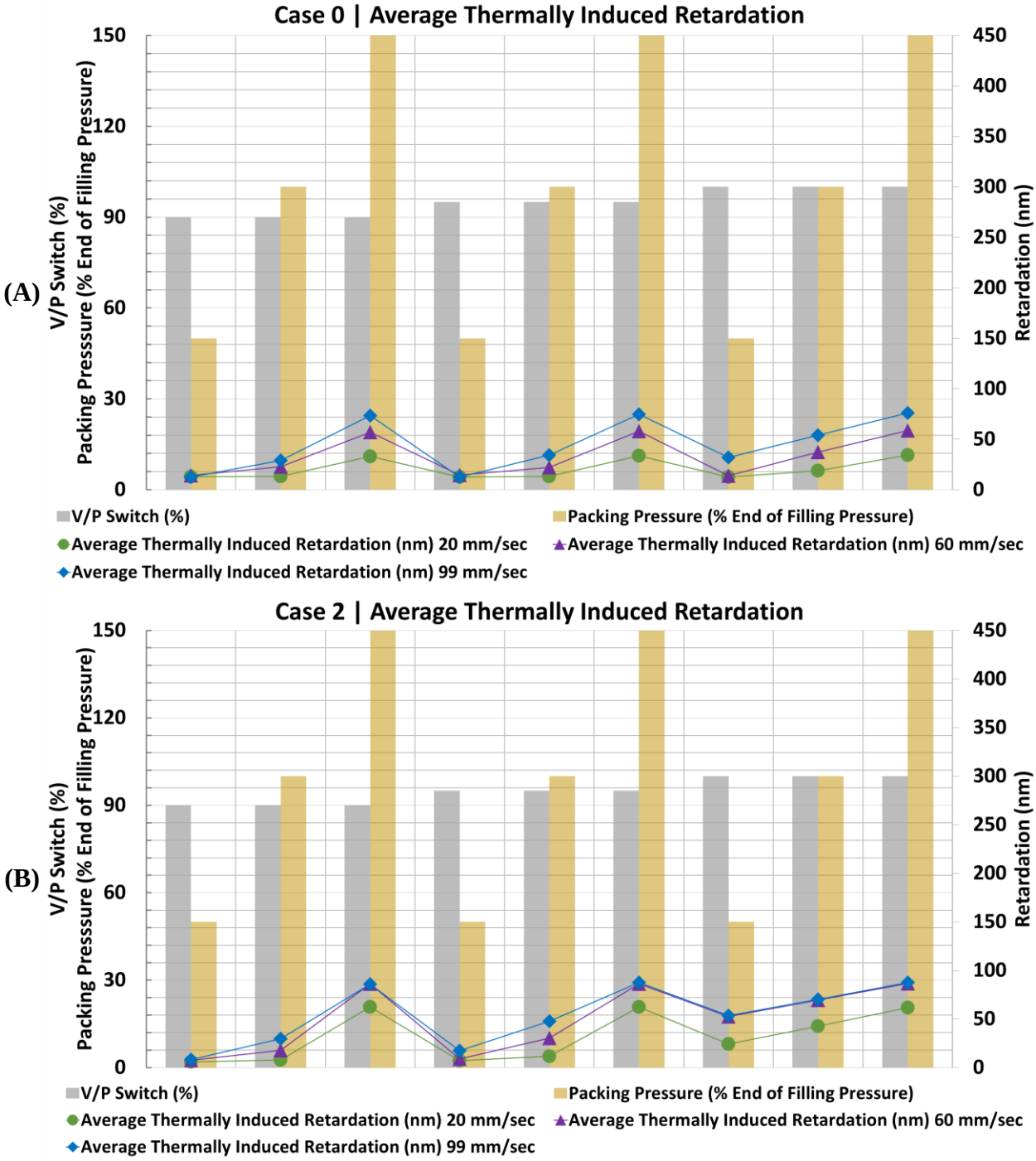

Figure 40: Average thermally induced retardation versus processing parameters of V/P switch and packing pressure for the three flow rate levels.

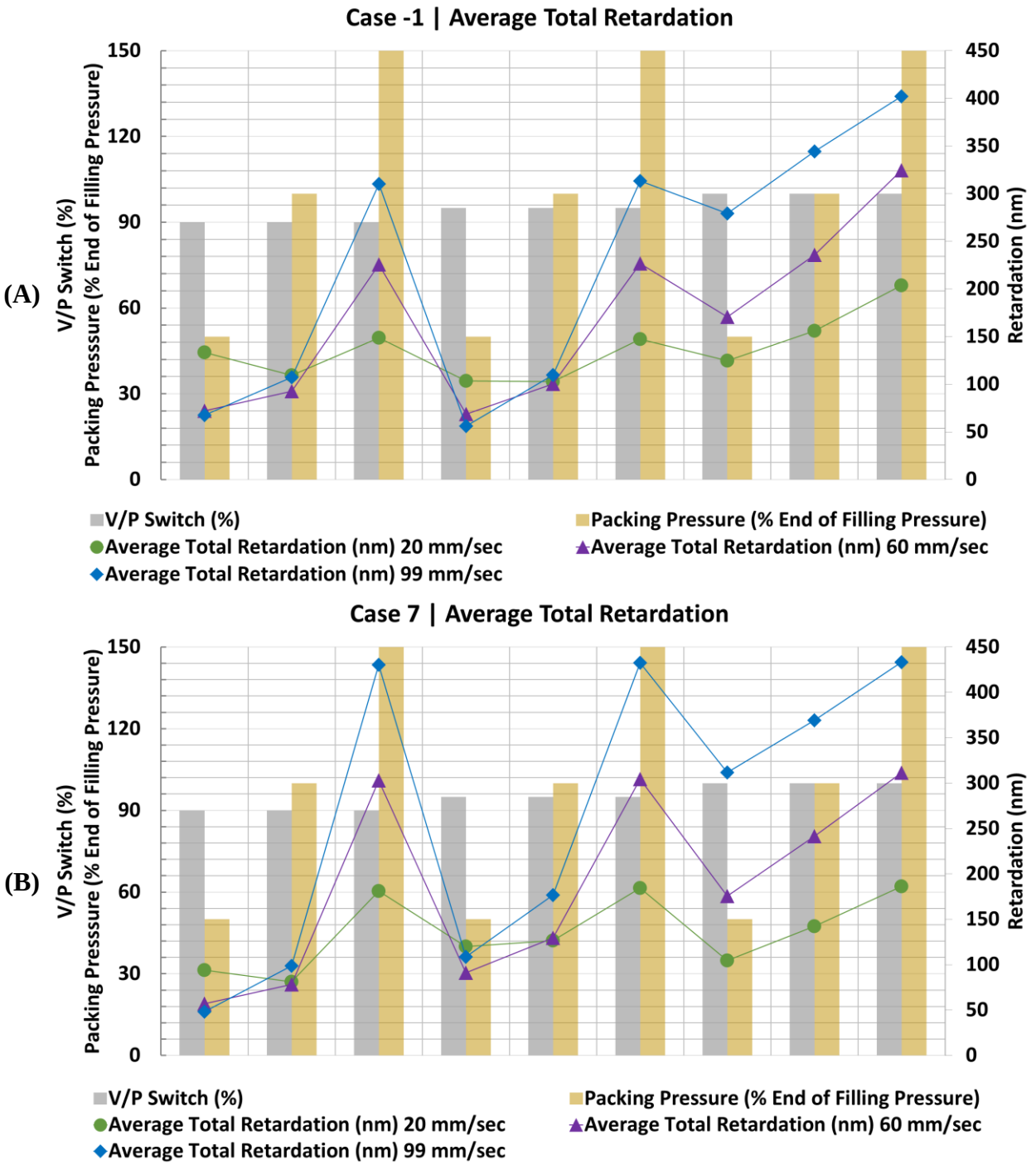

Figure 41: Average total retardation versus processing parameters of V/P switch and packing pressure for the three flow rate levels.

Figure 42 and Figure 43 show the average volumetric shrinkage and standard deviation volumetric shrinkage for the minimum cases with and without a reservoir. For the average volumetric shrinkage Cases -1 and 2 are shown in Figure 42. While the magnitudes are different

the trends match between all the cases and show that the minimum average volumetric shrinkage occurs when the highest packing pressure and highest flow rate is used. The later V/P switch (100%) also yields lower average volumetric shrinkage although the difference is less significant. These results are expected since the higher injection rate caused higher injection pressure and that and the higher packing pressure cause more force to be experienced by the melt and therefore increased density and reduced volumetric shrinkage. Cases 0 and 1 are shown in Figure 43 showing the trends of the standard deviation volumetric shrinkage for all 27 runs. There is more variation in the trends of the standard deviation, but the lowest results occur with the lowest flow rate, earlier V/P switch, and lowest packing pressure values.

These results show that the minimum retardation value and minimum volumetric shrinkage results occur at opposite ends of the processing parameters. Thus, there will have to be a tradeoff between these quality parameters. The standard deviation of volumetric shrinkage can be related to warpage due to the non-uniform volumetric shrinkage. The minimum standard deviation of volumetric shrinkage trend is more similar to the minimum retardation trends, which could lead to settings yielding high-quality parts that have low retardation and low warpage. In this way, these simulations indicate that reservoirs could be used to improve injection molding of plastic optical parts.

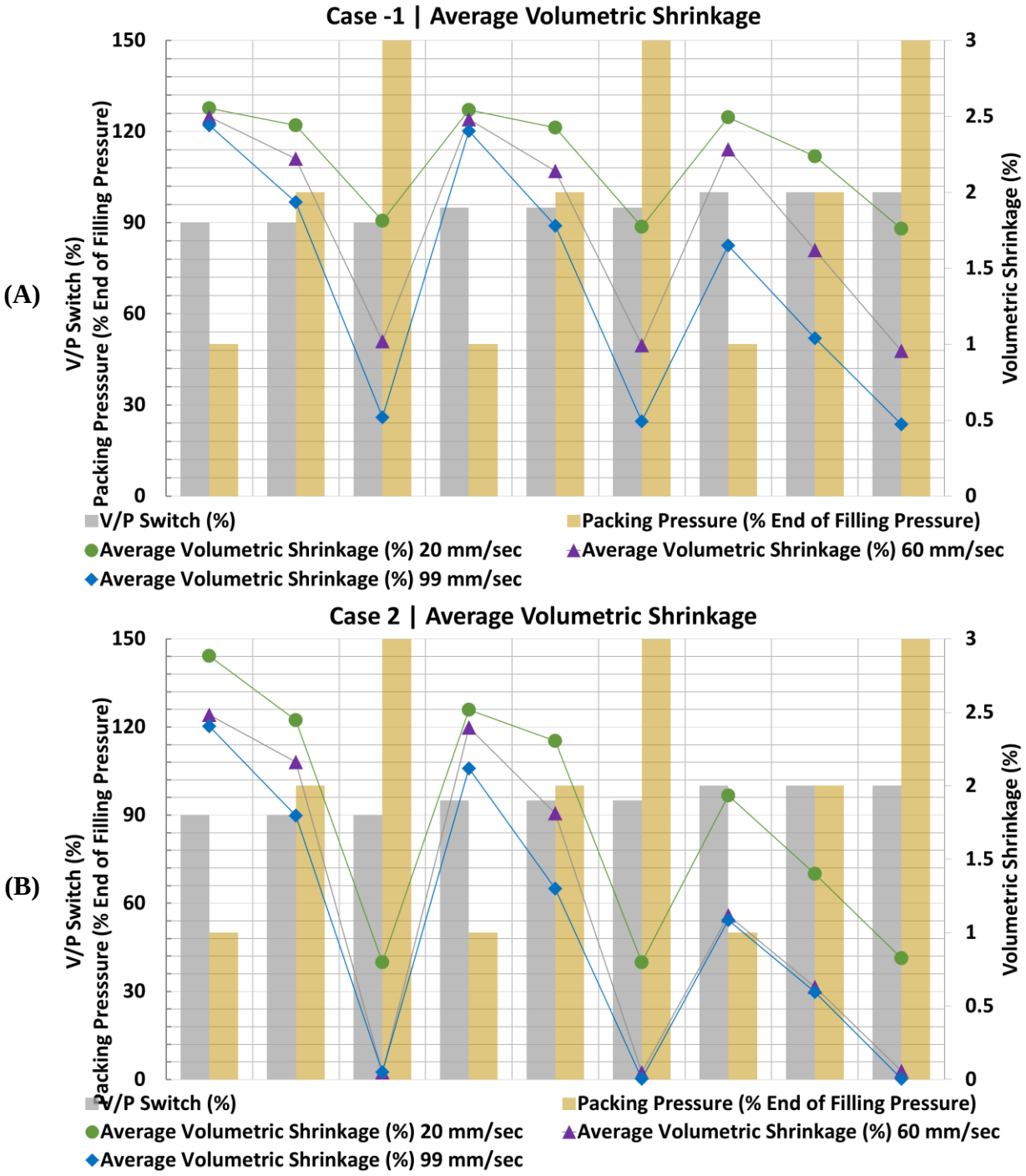

Figure 42: Average volumetric shrinkage versus processing parameters of V/P switch and packing pressure for the three flow rate levels.

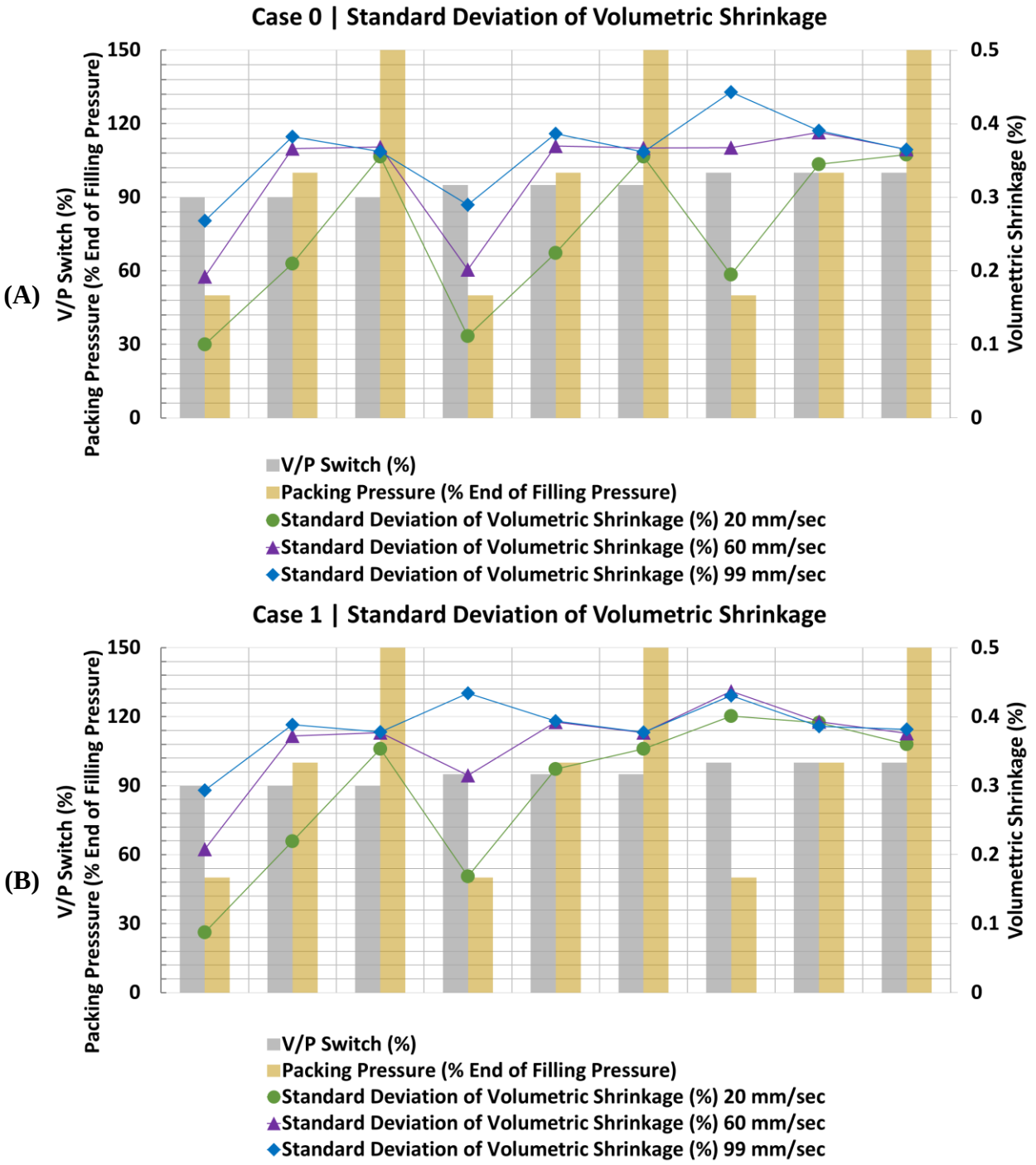

Figure 43: Standard deviation volumetric shrinkage versus processing parameters of V/P switch and packing pressure for the three flow rate levels.

4. Conclusion

The use of a sacrificial reservoir as part of an injection mold with optical polycarbonate (PC) materials was explored with simulations. Three different methods of reservoir designs were considered. The first method was using engineering intuition to determine the geometry, the second method used a combination of mass and momentum balance equations to determine the geometry, lastly, the third method used only the mass balance equation to determine the geometry. Using these three methods eight reservoirs were designed and simulated and compared to two no-reservoir cases. For each of the 10 geometry cases, 27 runs covering three levels of injection flow rate, V/P switch, and packing pressure were simulated.

The quality parameters of flow and thermally induced retardation and the average and standard deviation of volumetric shrinkage of lens parts were considered. For each of the quality parameters the minimum, best case occurred with one of the reservoirs. For each of the geometry cases the quality parameter versus the three processing parameters were compared. The trends for the quality parameters agreed between the cases. The lowest volumetric shrinkage occurred with high flow rate, late V/P switch, and high packing pressure, which was the inverse processing parameters for the lowest retardation and standard deviation volumetric shrinkage results. In this way a tradeoff must be made between these quality parameters. Since overall volumetric shrinkage can be compensated with proper cavity dimensions, the optical property of retardation and standard deviation of volumetric shrinkage, which can be directly related to warpage, are more significant to optical part quality. Thus, the reservoirs offer a method to improve both the retardation and warpage defects in injection molded optical parts.

Conclusion

Two methods of mold modification for injection molding specialty plastic parts were developed in three projects.

The use of a static mixer within the runner system in an injection mold with fiber-reinforced polypropylene material was explored with simulations and molding experiments in the first project. It was found that the mixers had the expected result of increasing machine injection pressure requirements during the injection stage due to the restriction of flow area in the runners. The mixers had a more complex effect on the temperature results due to the increased conductive cooling and shear heating from the flow restriction. For the general quality parameters of volumetric shrinkage and density at the end of packing the mixers appeared to cause increased shrinkage and decreased density but also yielded improved uniformity in the shrinkage results, thereby, indicating a potential reduction in part warpage when a mixer is used. The mixers successfully disrupted the fiber alignment in the runner, which was shown both in simulations and the molding experiments. There was also a slight decrease in the degree of fiber alignment for the disk mold as predicted in the simulations. However, the degree of fiber alignment was restored to near no-mixer values for the two-cavity impact + tensile bar mold by the time the melt reached the part cavity, yielding diminishing change in the orientation of the fibers within the part. In summary, the use of a static mixer shows potential in allowing for mixing after the plasticizing unit, but its impact in the fiber orientation in the final molded parts will depend on where it is positioned, the number of mixer elements, and the subsequent fiber re-orientation effect.

For the second project the use of a static mixer within the runner system in an injection mold with polystyrene (PS) materials was explored with simulations and molding experiments. It was found that the mixers had the expected result of increasing machine injection pressure requirements during the injection stage due to the restriction of flow area in the runners. The mixers also increased the shear rate. For the general quality variables of volumetric shrinkage and density at the end of packing, the mixers appeared to cause increased shrinkage and decreased density, but the change was small. The mixer had a slight effect on the optical property of retardation, which is shown both in simulations and the molding experiments. In the simulations the thicker, 1 mm helical and built-in mixer cases (Case 2 and 6) showed some improvements for the flow-induced optical properties. However, in the experiments the built-in

mixers showed improvements in the retardation and the helical mixers showed that they caused the retardation to increase slightly. All the cases yielded similar retardation values except the no-mixer no-packing case, suggesting the importance of the packing stage on the part retardation. In summary, the use of a static mixer shows potential in allowing for mixing after the plasticizing unit, but its impact in the optical properties in the final molded parts appears to be slight. Nonetheless, the mixers could still be used for post-plasticizing unit mixing to alleviate issues such as mold-flow imbalance without affecting the final part properties.

In the final project the use of a sacrificial reservoir as part of an injection mold with optical polycarbonate (PC) materials was explored with simulations. Three different methods of reservoir designs were considered. The first method was using engineering intuition to determine the geometry, the second method used a combination of mass and momentum balance equations to determine the geometry, lastly, the third method used only the mass balance equation to determine the geometry. Using these three methods eight reservoirs were designed and simulated and compared to two no-reservoir cases. 27 runs varying three levels of injection flow rate, V/P switch, and packing pressure were simulated for each of the 10 geometry cases.

The quality parameters of flow and thermally induced retardation and the average and standard deviation of volumetric shrinkage of lens parts were considered. For each of the quality parameters the minimum, best, case occurred with one of the reservoirs. For each of the geometry cases the quality parameter versus the three processing parameters were compared. The trends for the quality parameters agreed between the cases. The lowest volumetric shrinkage occurred with high flow rate, late V/P switch, and high packing pressure which was the inverse processing parameters for the lowest retardation and standard deviation volumetric shrinkage results. In this way a tradeoff must be made between these quality parameters. Since overall volumetric shrinkage can be compensated with oversized molds the optical property of retardation and standard deviation of volumetric shrinkage, which can be directly related to warpage, are more significant to optical part quality thus, the reservoirs offer a method to improve both the retardation and warpage defects in injection molded optical parts.

In sum these three projects show that there are opportunities to improve injection molding part qualities by introducing novel mold geometries into the process. Further, this work shows how simulation software can be used as a proof-of-concept and prototyping tool to explore new mold ideas without requiring excessive capital investment into specialty molds.

Future Work

Each of the three research projects described has several areas of future work that should be considered. They are described as follows:

Effect of Static Mixer on Fiber Orientation of Injection Molded Fiber-reinforced Composites

To further explore the benefits of using a static mixer to provide mixing post-plasticizing unit a study on the number of elements and mixer location within the runner system could be completed. The work done thus far indicates that these two variables change the effect of the mixer on fiber orientation in the final part. Further, repeating injection molding experiments with additional mixer geometries and different runner systems would be beneficial to continue to validate the simulations. Finally, additional studies on different polymers could be explored to determine if the polypropylene experiments already completed are indicative of the results for other common injection molding materials.

Effect of Static Mixer on Optical Properties of Plastic Injection Molded Parts

Future work on the effects of the static mixer on optical properties should include considerations on the number of mixer elements and further development of the built-in mixer geometries so more complex mixing could be generated with a machined-in mixer. Since polystyrene is not commonly used for high quality optical components testing a material such as polycarbonate could also be beneficial to determine if the same optical result trends are exhibited. Finally, experiments showing the benefits of mixers for thermal homogenization and preventing the common melt fill-imbalance problem should be explored.

Effect of Sacrificial Reservoir Runner Geometry on Optical Properties of Plastic Injection Molded Parts

Since the work considering the sacrificial reservoir geometry has been calculation and simulation based to this point experimental injection molding trials are the next step in the development of this idea. A reservoir mold insert with adjustable volume and cross-sectional geometry could successfully validate the simulations presented in this work.

References

[1] E. S. Zainudin, S. M. Sapuan, S. Sulaiman and M. M. H. M. Ahmad, "Fiber orientation of short fiber reinforced injection molded thermoplastic composites: a review," *Journal of Injection Molding Technology,* vol. 6, no. 1, pp. 1-10, 2002.

[2] C. A. Silva, J. C. Viana, F. W. J. v. Hattum and A. M. Cunha, "Fiber orientation in divergent/convergent flows in expansion and compression injection molding," *Polymer Composites,* vol. 27, no. 5, pp. 539-551, 2006.

[3] L. A. Goettler, "Mechanical property enhancement in short-fiber composites through the control of fiber orientation during fabrication," *Polymer Composites,* vol. 5, no. 1, 1984.

[4] P. H. Foss, H.-C. Tseng, J. Snawerdt, Y.-J. Chang, W.-H. Yang and C.-H. su, "Prediction of fiber orientation distribution in injection molded parts using Moldex3D simulation," *Polymer Composites,* vol. 35, no. 4, pp. 671-680, 2014.

[5] T. D. Papathanasiou, I. Kuehnert and N. D. Polychronopoulos, "5 - Flow-induced alignment in injection molding of fiber-reinforced polymer composites," in *Flow-induced alignment in composite materials*, T. D. Papathanasiou and A. Bénard, Eds., Woodhead Publishing, 2022, pp. 123-185.

[6] K. Yang, C. Xin, D. Yu, B. Yan and Y. He, "Experimental study and evaluation of mixing mechanism and performance in triple-screw extruder," *Adv Polym Technol,* pp. 2452-2461, 2018.

[7] T. Sakai, "Influence of melting zone and melt homogeneity on extrusion and injection molding process," *IPP,* pp. 229-237, 1990.

[8] T. A. Osswald, Understanding polymer processing: processes and governing equations, Cincinnati: Hanser Publications, 2017.

[9] S. A. Stewart, J. Dominguex-Robles, R. F. Donnelly and E. Larraneta, "Implantable polymeric drug delivery devices: classification, manufacture, materials , and clinical applications," *Polymers,* pp. 1-24, 2018.

[10] G. F. Wilson and Y. Eckstein, "Moldable low density thermoplastic composite with hollow glass spheres and the method for compounding". USA Patent US5017629A, 1989.

[11] V. B. Gupta, R. K. Mittal, P. K. Sharma, G. Mennig and J. Wolters, "Some studies on glass fiber-reinforced polypropylene. Part I: Reduction in fiber length during processing," *Polym. Compos.,* pp. 8-15, 1989.

[12] N. Gately and J. Kennedy, "Processing stability and the significance of variation in extrusion speeds and temperatures on SSB 55 pharma grade shellac for oral drug delivery," *JMMP*, pp. 1-14, 2017.

[13] A. Inoue, K. Morita, T. Tanaka, Y. Arao and Y. Sawada, "Effect of screw design on fiber breakage and dispersion in injection-molded long glass-fiber-reinforced polypropylene," *Journal of Composite Materials*, pp. 75-84, 2013.

[14] K. M. Grout and R. D. Devellian, "Mixing device". USA Patent US3664638A, 1970.

[15] National Oilwell Varco, "Kenics static mixer technology," [Online]. Available: https://www.chemineer.com/products/kenics/hev-mixers/item/download/498_92dbac57b6110550a0b2d40068bd441f.html.

[16] S. Soman, "Study of effects of design modification in static mixer geometry and its applications," University of Waterloo, Waterloo Ontario, 2016.

[17] D. Rauline, J.-M. Le Blevec, J. Bousquet and P. A. Tanguy, "A comparative assessment of the performance of the Kenics and SMX static mixers," *Chemical Engineering Research and Design*, pp. 389-396, 2000.

[18] D. M. Hobbs and F. J. Muzzio, "The Kenics static mixer: a three-dimensional chaotic flow," *Chemical Engineering Journal*, pp. 153-166, 1997.

[19] F. H. Ling and X. Zhang, "A numerical study on mixing in the Kenics static mixer," *Chemical Engineering Communications*, pp. 119-141, 2007.

[20] M. Regner, K. Ostergren and C. Tragardh, "Effects of geometry and flow rate on secondary flow and the mixing process in static mixers-a numerical study," *Chemical Engineering Science*, pp. 6133-6141, 2006.

[21] V. Kumar, V. Shirke and K. D. P. Nigam, "Performance of Kenics static mixer over a wide range of Reynolds number," *Chemical Engineering*, pp. 284-295, 2008.

[22] R. K. Rahmani, T. G. Keith and A. Ayasoufi, "Three dimensional numerical simulation and performance study of an industrial helical static mixer," *Journal of Fluids Engineering*, pp. 467-483, 2005.

[23] R. K. Rahmani, T. G. Keith and A. Ayasoufi, "Numerical simulation and mixing study of pseudoplastic fluids in an industrial helical static mixer," *Journal of Fluids Engineering*, pp. 467-480, 2006.

[24] J. Arimond and L. Erwin, "A simulation of a motionless mixer," *Chemical Engineering Communications*, pp. 105-126, 2007.

[25] R. M. Untrlander, M. Brelski, R. D. Schad, P. A. Lacza and D. D. Craig, "Static mixer for an injection molding system". Europe Patent EP1622705B1, 2004.

[26] C. W. Wallace and H. A. Koenic, "Method for injection molding articles wherein additives are added in selective portions". USA Patent US4255367A, 1978.

[27] C. D. Han, C. A. K. Y. W. Villamizar and S. J. Chen, "Morphology and mechanical properties of injection-molded specimens of two-phase polymer blends," *J. Appl. Polym. Sci.*, pp. 353-370, 1977.

[28] Stamixco, "Static mixing technology for extrusion and injection molding," [Online]. Available: https://www.stamixco.com/downloads/Stamixco_Technical_Presentation.pdf.

[29] Promix Solutions, "Static mixers and mixing nozzles for injection molding," [Online]. Available: https://www.promix-solutions.ch/mixing-nozzle-injection-molding.html.

[30] J. P. Beaumont, J. H. Young and M. J. Jaworski, "Mold filling imbalances in geometrically balanced runner systems," *Journal of Reinforced Plastics and Composites*, pp. 572-590, 1999.

[31] K.-M. Tsai, "Runner design to improve quality of plastic optical lens," *Int J Adv Manuf Technol*, pp. 523-536, 2013.

[32] D. Shotwell, S. Glas, E. Chen and L.-S. Turng, "Analysis of injection molding simulation of static mixer within the runner system to improve melt homogeneity, filler distribution, and part quality," in *ANTEC*, 2021.

[33] ImageJ, "Fiji," ImageJ, [Online]. Available: https://imagej.net/software/fiji/. [Accessed 2022].

[34] Moldex3D, "Moldex3D Help 2021," CoreTech System, 2021. [Online]. Available: http://support.moldex3d.com/2021/en/index.html. [Accessed 2022].

[35] T. A. Osswald, L.-S. Turng and P. Gramann, Injection Molding Handbook, Cincinanati: Hanser Gardner Publications, Inc., 2008.

[36] S. Baumer, Handbook of Plastic Optics, Weinheim: Wiley-VCH Verlag GmbH & Co. KGaA, 2010.

[37] U. Greis and G. Kirchhof, "Injection molding of plastic optics," in *Optical Surface Technology*, Garmisch-Partenkirchen, 1983.

[38] T. Matiacio, "Injection molding of optical components," in *Replication and Molding of Optical Components*, Los Angeles, 1988.

[39] S.-C. Chen and L.-S. Turng, Advanced Injection Molding Technology, Cincinnati: Hanser Publications, 2016.

[40] M. Roeder, P. Schilling, D. Hera, T. Guenther and A. Zimmerman, "Influences on the fabrication of diffractive optical elements by injection compression molding," *J. Manuf. Mater. Process.*, pp. 1-11, 2018.

[41] C.-Y. Chung, "Integrated optimum layout of conformal cooling channels and optimal injection molding process parameters for optical lenses," *Appl. Sci.*, pp. 1-17, 2019.

[42] C. Yang, L. Su, C. Huang, H.-X. Huang, J. M. Castro and A. Y. Yi, "Effect of packing pressure on refractive index variation in injection molding of precision plastic optical lens," *Advances in Polymer Techology*, pp. 51-61, 2011.

[43] M.-W. Wang, C.-H. Chen, F. Arifin and J.-J. Lin, "Modeling and analysis of multi-shot injection molding of Blu-ray objective lens," *Journal of Mechanical Science and Technology*, pp. 4839-4849, 2018.

[44] J. C. Lin and K. S. Lee, "Molding analysis of multi-cavity aspheric lens and mold designing," *Advanced Materials Research*, pp. 77-87, 2010.

[45] L. Li, T. W. Raasch and A. Y. Yi, "Simulation and measurement of optical aberrations of injection molded progressive addition lenses," *Applied Optics*, pp. 6022-6029, 2013.

[46] Y.-J. Chang, C.-K. Yu, H.-S. Chiu, W.-H. Yang, H.-E. Lai and P.-J. Wang, "Simulations and verifications of true 3D optical parts by injection molding process," in *ANTEC*, 2009.

[47] H. E. Lai and P. J. Wang, "Study of process parameters on optical qualities for injection-molded plastic lenses," *Applied Optics*, pp. 2017-2027, 2008.

[48] S.-W. Kim and L.-S. Turng, "Three-dimensional numerical simulation of injection molding filling of optical lens and multiscale geometry using finite element method," *Polymer Engineering and Science*, pp. 1263-1274, 2006.

[49] Y. D. Jeong and M. K. Jang, "A new runner system melt-buffer for filling balance in injection mold," *Transactions of Materials Processing*, pp. 122-127, 2009.

[50] K. Yang, C. Xin, D. Yu, B. Yan and Y. He, "Experimental study and evaluation of mixing mechanism and performance in triple-screw extruder," *Adv Polym Technol*, pp. 2452-2461, 2018.

[51] C. W. Wallace and H. A. Koenic, "Method for injection molding articles wherein additives are added in selective portions". USA Patent US4255367A, 1978.

[52] A. I. Isaev, K. D. Vachagin and A. M. Naberezhnov, "An engineering method for calculating the flow of polymers in channels of noncircular cross section," *Journal of engineering physics*, vol. 27, no. 2, pp. 998-1002, 1974.

[53] B. E. Sørensen, "A revised Michel-Lévy interference colour chart based on first-principles calculations," *European Journal of Mineralogy*, vol. 25, no. 1, pp. 5-10, 2013.

[54] V. W. Wang, K. K. Wang and C. A. Hieber, "An interactive computer program for runner-system design in injection molding," in *ANTEC*, Chicago, 1983.

[55] L. Yang, S. J. Chen, M. Charmchi and C. Douglas, "Runner design through flow balancing by proper dimensioning of runner system. Part I: Solidification of polymer flow in round tube," in *ANTEC*, Boston, 1986.

[56] S. C. Chen and C. Hsu, "A practical approach for flow branching and flow balancing," in *ANTEC*, Los Angeles, 1987.

[57] J. P. Goff and A. Whelan, "Optimizing the runner layout for a multi-cavity mould," in *ANTEC*, New York, 1989.

[58] W. R. Jong, S. C. Chen and K. K. Wang, "An integrated design system for 3-D runner balancing of injection-molding process," in *ANTEC*, San Francisco, 1994.

[59] R. B. Bird, W. E. Stewart and E. N. Lightfoot, Transport Phenomena, New York: John Wiley & Sons Inc., 1960.

[60] T. Osswald and J. P. Hernandez-Ortiz, Polymer Processing: Modeling and Simulation, Cincinnati: Hanser Gardner Publications, Inc., 2006.